APPLIED COMPUTATIONAL ELECTROMAGNETICS SOCIETY JOURNAL

February 2017
Vol. 32 No. 2
ISSN 1054-4887

The ACES Journal is abstracted in INSPEC, in Engineering Index, DTIC, Science Citation Index Expanded, the Research Alert, and to Current Contents/Engineering, Computing & Technology.

The illustrations on the front cover have been obtained from the research groups at the Department of Electrical Engineering, The University of Mississippi.

EMERITUS EDITORIAL ASSISTANTS

FEBRUARY 2017 REVIEWERS

THE APPLIED COMPUTATIONAL ELECTROMAGNETICS SOCIETY

JOURNAL

Vol. 32 No. 2 February 2017

TABLE OF CONTENTS

FDTD Potentials for Dispersion Analysis of Sinusoidally Modulated Media

Fatemeh M. Monavar [1], Gholamreza Moradi [2,3], and Pedram Mousavi [3]

[1] Department of Electrical and Computer Engineering
University of Alberta, Edmonton, T6G 1H9, Canada
mohamadi@ualberta.ca

[2] Department of Electrical Engineering
Amirkabir University of Technology (Tehran Polytechnic), Tehran, Iran
ghmoradi@aut.ac.ir, gmoradi@ualberta.ca

[3] Department of Mechanical Engineering
University of Alberta, Edmonton, T6G 1H9, Canada
pmousavi@ualberta.ca

Abstract ─ A numerical study based on the finite difference time domain (FDTD) method is presented for the oblique incidence of TE modes with an emphasis on dispersion properties. The proposed medium has sinusoidally modulated dielectric permittivity. In order to truly address this scattering problem, total field-scattered field (TFSF) approach is suggested, which yields accurate results for the electric field distribution inside the modulated medium. A comparison between analytical plots and the FDTD results reveals the ability of FDTD in rigorous analysis of band diagrams for any arbitrary value of modulation factor. In addition, a closed form formula for numerical dispersion relation is derived for the case of small modulation.

Index Terms ─ Dispersion analysis, FDTD, inhomogeneous media, Mathieu functions, oblique incidence, permittivity-modulated media, scattering, TFSF.

I. INTRODUCTION

Modulated structures have gained a great deal of attention in recent years. It is mainly due to their band-gap behavior which allows one to control the propagation and possible radiation of electromagnetic waves off these configurations. These platforms are extensively used to realize both radiating and non-radiating devices such as leaky-wave antennas, metamaterial lenses, filters, and etc. [1-3]. In antenna applications they are particularly useful for miniaturization, bandwidth enhancement, surface-coupling reduction, and generation of holographic surfaces.

In general, two common solutions are offered to exhibit band-gap properties in materials. First is by periodic arrangement of parasitic loads, which suggests modulation of the surface impedance. The second solution is periodic variation of electromagnetic properties of the material, i.e., modulation of effective permittivity. Drilling holes in dielectrics [4] or periodic variation of the width of microstrip line [5] are among solutions proposed to change effective dielectric permittivity in terms of fabrication and manufacturing.

Over the past years surface impedance modulation has received considerable studies (see [2] for instance), whereas modulation of effective dielectric permittivity has been investigated in an intermittent way throughout the years [5-6]. It is due to the complexity involved in Maxwell's equations, once the permittivity of the medium is altered as a function of space coordinate(s). This in fact changes the whole dynamic of the wave equation, which makes it impossible to find a simple analytic solution. In this case, one has to take into consideration that the medium is no longer homogeneous and it will treat electromagnetic waves differently as they try to propagate through. Since inhomogeneous media are finding very attractive applications in electromagnetic and antennas, it is absolutely necessary to find techniques to analyze such configurations [7,8].

A lot could be said about the characteristics of wave propagation by inspecting the dispersion curve corresponding to the structure along which the wave travels. Therefore the first step in designing unit cells is to obtain the related dispersion diagram. However this is not a straightforward process even for the case of homogeneous structures. Now for the non-homogeneous media, this could be quite a challenge since it requires exact knowledge of the effective permittivity of the medium at hand. Various numbers of numerical approaches have been adopted over the years for this

Submitted On: September 19, 2016
Accepted On: December 24, 2016

purpose. Despite the satisfactory results derived by these methods, they are still suffering from a deplorable lack of generality. Furthermore, the application of these methods is restricted by some factors like the configuration of the unit cell, the amount of loss associated with the excited modes, and etc. [2,5,9]. All these restrictions make it difficult to effectively employ the useful features of modulated structures. Hence, we were stimulated to revisit this problem in more depth. Therefore, the main motivation of this work is to develop a more general procedure capable of analyzing modulated structures in a fast and accurate way. Another aspect of this work is that it is focused on the study of an open structure, while mostly the investigations found in the literature have only considered closed structures.

Here we apply finite difference time domain FDTD method in an attempt to find both the dispersion and also field distributions for a medium whose effective permittivity has been sinusoidally modulated. The FDTD method has been selected since in addition to its generality it is robust and proved to produce reliable results for a wide number of applications [10]. However, we are aware of some negative impacts of FDTD like the numerical dispersion and try to choose the numerical parameters to avoid such effects.

The paper is structured as follows. In Section II, we begin by the wave equation inside the stratified structure. Then in Section III, we proceed to the more complicated task of finding dispersion plots. Three major methods of *graphical*, *analytical* and *numerical* are investigated and dispersion plots from each method are compared. It is proved that the proposed numerical method is capable of accurately predicting wave behavior and band gap limits inside the modulated medium and it has no restriction regarding the value of the modulation index as opposed to the analytical method. A demonstration of the electric field distribution inside modulated medium is also presented that agrees well with the theory which confirms the validity and reliability of the proposed method.

II. FORMULATION OF THE PROBLEM

A. TE wave equation

For a transverse electric, TE wave obliquely incident from free space to the semi-infinite medium of Fig. 1, under the assumption $\partial/\partial y = 0$, the wave equation is given by:

$$\frac{\partial^2 E}{\partial x^2} + \frac{\partial^2 E}{\partial z^2} = \mu_o \varepsilon_o \varepsilon_r (1 - M\cos 2\pi \frac{z}{d}) \frac{\partial^2 E}{\partial t^2}, \qquad (1)$$

where $\varepsilon(z) = \varepsilon_r(1 - M\cos 2\pi \frac{z}{d})$, being the relative dielectric permittivity of the modulated medium with ε_r, d, and M identifying the average permittivity, periodicity, and modulation constant respectively.

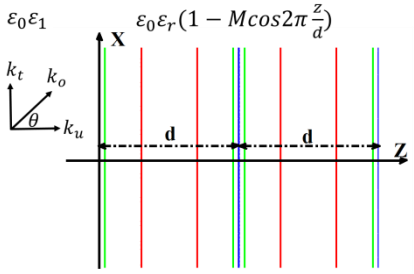

Fig. 1. Oblique incidence on a semi-infinite stratified medium. Shown to the left and right hand side of the *x*-axis, are the permittivity constants of the un-modulated and modulated media, respectively. The un-modulated medium is considered free space, hence its relative permittivity, ε_1 is equal to 1.

B. FDTD discretization

For FDTD computation we first set the following assignments:

$$E(x_i, z_m, t_n) = E(i\Delta x, m\Delta z, n\Delta t) = E^n_{i,m}, \qquad (2)$$

$$\varepsilon(z_m) = \varepsilon_r(1 - M\cos 2\pi \frac{m\Delta z}{d}) = \varepsilon_m. \qquad (3)$$

Now we use central-time central-space discretization scheme to form the discretized version of (1):

$$E^{n+1}_{i,m} = 2E^n_{i,m}(1 - \theta_x - \theta_z) + \theta_x\left(E^n_{i+1,m} + E^n_{i-1,m}\right) + \theta_z\left(E^n_{i,m+1} + E^n_{i,m-1}\right) - E^{n-1}_{i,m}, \qquad (4)$$

where $\theta_x = \frac{1}{\mu_o\varepsilon_o\varepsilon_m}\left(\frac{\Delta t}{\Delta x}\right)^2$, and $\theta_z = \frac{1}{\mu_o\varepsilon_o\varepsilon_m}\left(\frac{\Delta t}{\Delta z}\right)^2$ with Δx, and Δz, being grid spacing and Δt designating time increment. In the next sections, we employ this scheme to calculate the electric field intensity inside the modulated medium.

III. DISPERSION ANALYSIS

A. Graphical dispersion

For the medium presented in Fig. 1 as shown in [6], solutions of wave Equation (1) can be described in the form of Mathieu functions and there is no closed form formula for the dispersion relation. In fact, dispersion in such medium can be obtained by the help of "Mathieu stability diagrams" using the graphical approach. A comprehensive study of this kind can be found in [6]. In what follows we will present a brief illustration of the method. We restrict our discussion to the case of oblique incidence in Fig. 1 considering $k_o = \omega\sqrt{\mu_0\varepsilon_0}$ the free space wavenumber, with k_t and k_u being the wavenumbers along *x* and *z* directions respectively given by $k_t = k_o\sqrt{\varepsilon_1}sin\theta$ and $k_u^2 = k_o^2\varepsilon_r - k_t^2$, where ε_1 is the relative permittivity of un-modulated medium and θ is the angle of incidence. The last expression, i.e., $k_u^2 = k_o^2\varepsilon_r - k_t^2$, would be the dispersion relation if no modulation was present in the medium, namely $M = 0$.

However, when $M \neq 0$ the propagation constant along z, namely κ, has to be obtained by employing an iterative process to numerically solve a continued fraction expression. This leads to "stability diagrams" of Fig. 2.

It is customary to plot stability diagrams in a-q axes [5,6]. The vertical axis, q is basically an indication of modulation parameter, M which is multiplied by $\left(\sqrt{\varepsilon_r}k_o d/\sqrt{2}\pi\right)^2$ to factor in the effect of average dielectric constant and also frequency, since dispersion is the description of wavenumber variation with respect to frequency and also as modulation index, M varies, wave experiences different stratifications in the medium, and hence different dispersion effects, so modulation coefficient M has to be included in the definition of the axis as well. A more sophisticated physical meaning of parameter q is actually dependent on the specific problem at hand for which Mathieu equation arises. For example, in a problem where Mathieu equation describes vibrating modes of an elliptical membrane, q is associated with the eigenfrequencies of those vibrating modes [11]. The horizontal axis is $a = (k_u d/\pi)^2$ and it arises when the method of 'separation of variables' is used in the TE wave Equation of (1) to find solutions of Mathieu equation. (See [6] for more details).

From Fig. 2 one can distinguish two distinct regions, the shaded areas are "stable regions" where κ is real, whereas in the unshaded areas (unstable regions) κ becomes complex. Furthermore, we can draw a line through origin that will cut through all the regions of stability diagrams. Intersection points are shown with red stars in Fig. 2. The slope of this line can be written as:

$$\tan\varphi = \frac{0.5\varepsilon_r M}{\varepsilon_r - \varepsilon_1 sin^2\theta}. \qquad (5)$$

From (5), one realizes that at a specific angle θ and for constant values of , ε_1, and ε_r the slope of this line, $\tan\varphi$ is fixed and an intersection point with stability diagrams is the value of κ excited at a certain frequency. If $M = 0$, then the slope of the line is zero and it will fall on the horizontal axis which is described by k_u^2 and as stated earlier, k_u^2 is the wave number in the absence of modulation in the medium.

In a general case where $M \neq 0$, in order to construct dispersion diagram we have to find variation of κ versus frequency. Note that by changing frequency, parameters a, and q vary along the straight line yielding different intersection points each corresponding to a specific value of propagation constant at that frequency. Such diagram is shown in Fig. 3 where one can recognize a band-gap between $15.99\ GHz - 18.99\ GHz$. This is a result of the straight line of Fig. 2 passing through the first unstable region of stability diagrams and exciting waves with complex values of κ.

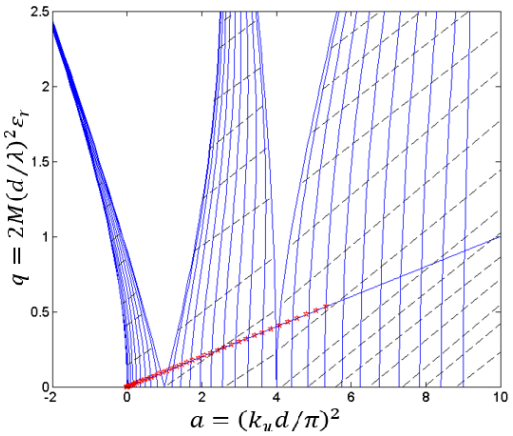

Fig. 2. Mathieu stability diagram (using the data in [12]). The intersecting points, shown with red stars on the straight line, determine the wavenumbers of modes excited in the modulated medium. Parameter λ used in the definition of q is the free space wavelength which is $1\ cm$ at the design frequency of $f = 30\ GHz$. Other parameters are as follows; $d = 1\ cm,\ M = 0.15,$ $\theta = 30^o,\ \varepsilon_r = \varepsilon_1 = 1$.

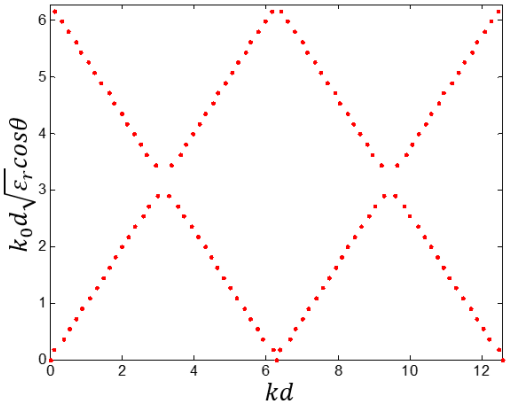

Fig. 3. Dispersion diagrams for the modulated medium shown in Fig. 1 using the graphical approach.

For the case represented in Fig. 2 based on the values given in the caption, the slope of the straight line given by (5) is equal to 0.1, and as can be seen it cuts through the stability diagrams where the appearance of the first band gap (first unshaded region) is noticeable, whereas it hardly cuts through the 2nd unstable region; hence the 2nd band gap is almost non-existent for such a small value of line slope. Therefore Fig. 3 is only focused on the first band gap. For higher values of incidence angle or modulation index the slope of the line increases and it will cut through both 1st and 2nd unshaded areas of Fig. 2 for which case both band gaps should be

considered.

B. Analytical dispersion

The above approach, though accurate but is frustrating since every time a single parameter in (5) varies, the whole process needs to be repeated. A more straightforward way is to use the following analytic expression suggested in [6] which is capable of predicting dispersion curves only when the value of q is taken very small and the solution is considered inside pass bands or the "stable' regions of the Mathieu stability diagram:

$$\frac{\kappa}{k_u} = 1 + \frac{1}{1-(k_u d/\pi)^2}\left(\frac{\pi}{k_u d}\frac{q}{2}\right)^2. \quad (6)$$

Under these circumstances, (7) is a good approximation for the solution of electric field inside the modulated medium:

$$E_y(x,z) = \left[1 - \frac{q}{2}.\frac{\cos\left(\frac{2\pi z}{d}\right) - j\frac{k_u d}{\pi}\sin\left(\frac{2\pi z}{d}\right)}{1-(k_u d/\pi)^2}\right] e^{jk_t x} e^{j\kappa z} e^{j\omega t}. \quad (7)$$

Designated with blue rhombus is the dispersion plot of (6) depicted in Figs.4 (a) and (b). One recognizes that (6) is quite accurate in pass-bands but when it comes to band-gaps its values cannot be trusted, which was expected as stated earlier.

C. Numerical dispersion

To find more satisfactory results we tried the FDTD technique. The discretized version of (7) is applied into (4) which reveals the numerical dispersion relation as in:

$$\sin^2\left(\frac{\omega\Delta t}{2}\right) = \theta_x \sin^2\left(\frac{k_t\Delta x}{2}\right) + \theta_z \sin^2\left(\frac{\kappa\Delta z}{2}\right). \quad (8)$$

Note that the actual expression is much more complicated and what is given in (8) is derived after taking into account certain approximations [13].

To examine the amount of numerical dispersion introduced by FDTD method into the solution one may try to find the κ-ω diagram of (8) but due to θ_x and θ_z being functions of space, as shown in Figs. 4 (a) and (b), plots will change for different nodes along the axis of modulation z.

This makes it hard to understand whether or not the numerical scheme is giving valid results in terms of band diagrams. However one interesting fact concluded from comparing Figs. 4 (a) and (b), is that such trend is periodic. As a matter of fact within one period, dispersion plots for nodes symmetrically located around $z = d/2$, (line of symmetry) are the same. Another interesting observation is that for the values selected here, neither of these plots suggests the existence of "numerical" band-gaps. The only effect is a small drift of dispersion plots along the nodes. This was expected since permittivity is a function of z, which means the guided wavelength varies along the modulation direction and so does the propagation constant.

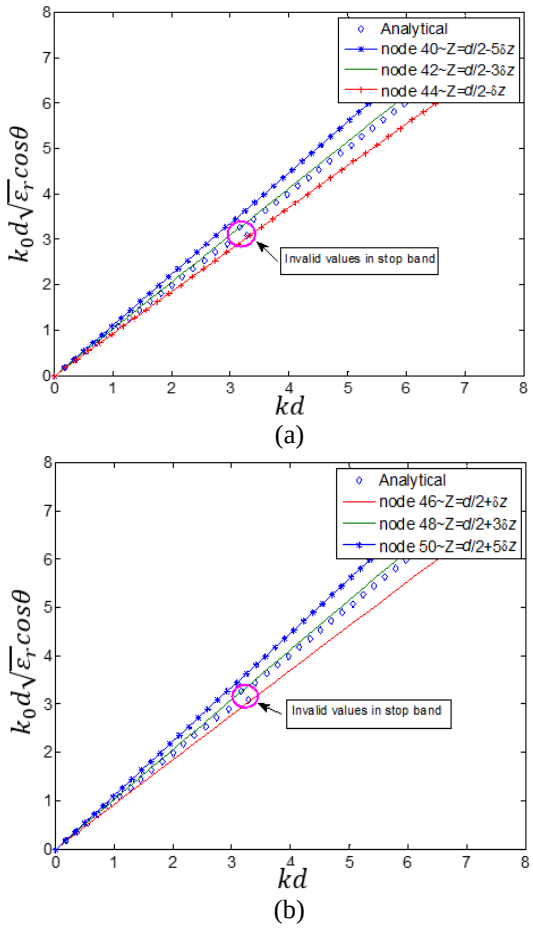

Fig. 4. Comparison of dispersion diagrams obtained by the approximate analytical solution in (6): blue rhombuses in both Figs. 4 (a) and (b), versus those obtained using (8) for: (a) sample nodes on the first half (left-hand) of the unit cell symmetry line, and (b) sample nodes on the second half (right-hand) of the unit cell line of symmetry.

These all mean that the approximations made to obtain (8) have worked out for the best since we could firstly avoid the numerical band-gaps arising from the periodic grid lattice used in the finite difference method and secondly, as suggested from Fig. 4(a) and (b), predict the dispersion plots quite accurately.

Back to our oblique incidence problem we need to find possible value(s) of κ that are excited in the modulated medium and also the band-gap frequencies. Based on the above analyses, the graphical method though accurate enough, is not necessarily the fastest way to approach the problem and (8) yields different dispersion plots for various nodes. It is also worth to emphasize that the approximations in (8) are only valid

within the pass bands not to mention the restrictions on the value of modulation constant. Having that in mind it seems like the most convenient way to obtain the dispersion curve is to calculate the electric field numerically at various sample frequencies and then to determine the wavenumber at each frequency. The results of such calculations are depicted in Fig. 5.

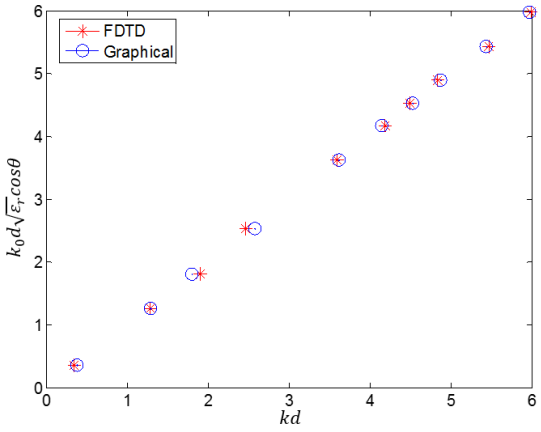

Fig. 5. Comparison between dispersion curves obtained by graphical approach and FDTD method.

A small discrepancy observed between the graphical and numerical plots is believed to be mostly due to a certain degree of approximation involved in the computation of the actual wavelength of the field. This can be explained using Fig. 6 where it can be seen that the electric field solution in the modulated medium has a slightly perturbed sinusoidal shape. One realizes this perturbation is responsible for a slight change of wavelength along the propagation direction. Hence, the results of Fig. 5 are obtained using the average value of the wavelength. There are other factors that affect the accuracy of plots in Fig. 5. First one needs to understand that the graphical approach, does not always give the exact values; to solve for the κ values we have to find the intersection points in Fig. 2 which requires the evaluation of non-integer Mathieu functions of any arbitrary order. Not enough tabulations of this kind can be found in literature. Furthermore, the intervals between two successive steps are often large not to mention the restricted range of parameters (namely q and a) for which these tables are available. Here we have used values in [12] which are obtained with an accuracy of 10^{-5}, however the intersection points, as presented in Fig. 2, do not exactly lie on the graphs available from [12] and therefore an interpolation process needs to be carried out to find the values in the intermediate steps. All these factors will introduce errors in the calculation of dispersion diagram, which then result in the small drift between the graphical and numerical plots of Fig. 5.

Lastly, we also computed the electric field solution inside the semi-infinite medium of Fig. 1, using a sinusoidal excitation at the incidence plane (at $z = 10\ cm$) chosen twenty wavelengths behind the air-dielectric interface (at $z = 30\ cm$).

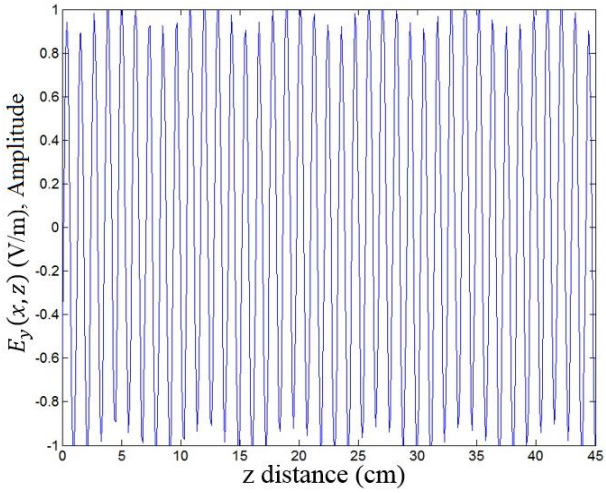

(a)

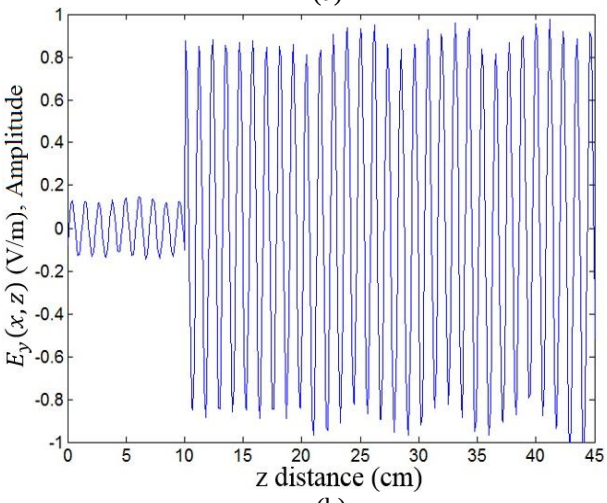

(b)

Fig. 6. Electric field distribution in modulated medium using: (a) closed form formula of (7) and (b) FDTD. As clear from the graph, $z = 30\ cm$ is the interface of air and the modulated medium whereas the incidence plane is set at $= 10\ cm$. To insure accuracy the modulated medium has extended over 15 wavelengths beyond the interface.

Using the total field-scattered field approach (TFSF), we account for multiple reflections that will happen due to continuous variation of the permittivity in the dielectric medium. It is clear from Figs. 6 (a) and (b) that the analytical and numerical results inside the modulated dielectric medium are in excellent agreement.

IV. CONCOLUSION

Realizing the challenge exist to address scattering problems involved oblique incidence, a numerical study based on FDTD has been presented to analyze wave propagation inside a modulated medium in terms of dispersion and field distribution. To avoid numerical dispersion a node-by-node band-diagram monitoring process has been carried out in order to adjust FDTD parameters to guarantee a distortion-free transmission. As an appropriate figure of merit for comparison of the numerical results, an approximate closed form formula was used. An inspection of band diagram and field distribution revealed great agreement between graphical and numerical results with the latter being less time consuming, more robust and accurate in predicting the band-limits.

ACKNOWLEDGMENT

The authors would like to thank TELUS, NSERC, TRTech and AITF for their support.

REFERENCES

[1] S. K. Podilchak, L. Metakovits, A. P. Freundorfer, Y. M. M. Antar, and M. Orefice, "Controlled leaky-wave radiation from a planar configuration of width-modulated microstrip lines," *IEEE Trans. Antennas Propag*., vol. 61, no. 10, pp. 4957-4972, Oct. 2013.

[2] A. M. Patel and A. Grbic, "A printed leaky-wave antenna based on a sinusoidally-modulated reactance surface," *IEEE Trans. Antennas Propag*., vol. 59, no. 6, pp. 2087-2096, June 2011.

[3] P. R. Villeneuve and M. Piché, "Photonic band gaps of transverse-electric modes in two-dimensionally periodic media," *J. Opt. Soc. Amer. A*, vol. 8, no. 8, pp. 1296-1304, Aug. 1991.

[4] G. P. Gauthier, A. Courtay, and G. M. Rebeiz, "Microstrip antennas on synthesized low dielectric-constant substrates," *IEEE Trans. Antennas Propag.*, vol. 45, no. 8, pp. 1310-1314, Aug. 1997.

[5] L. Matekovits, G. V. Colomé, and M. Orefice, "Controlling the band- limits of TE-surface wave propagation along a modulated microstrip- line-based high impedance surface," *IEEE Trans. Antennas Propag.*, vol. 56, no. 8, pt. 2, pp. 2555-2562, Aug. 2008.

[6] T. Tamir, H. C. Wang, and A. A. Oliner, "Wave propagation in sinusoidally stratified dielectric media," *IEEE Trans. Microw. Theory Techn*., vol. MTT-12, no. 3, pp. 323-335, May 1964.

[7] A. Farahbakhsh, D. Zarifi, and A. Abdolali, "Using MATLAB to model inhomogeneous media in commercial computational electromagnetics software," *ACES Journal*, vol. 30, no. 9, Sep. 2015.

[8] W. Rieger, M. Haas, C. Huber, G. Lehner, and W. M. Rucker, "Reconstruction of inhomogeneous lossy dielectric objects in one dimension," *ACES Journal*, vol. 12, no. 2, 1997.

[9] S. Tooni, T. F. Eibert, M. Tayarani, and L. Vietzorreck, "Dispersion analysis of open structures using reflection pole method," in Proc. *7th Eur. Conf. Antennas Propagation (EUCAP)*, pp. 2365-2368, Apr. 2013.

[10] A. Taflove and S. C. Hagness, *Computational Electrodynamics: The Finite Difference Time Domain Method*. 1st ed., Boston, Artech House, 1995.

[11] J. C. Gutierrez-Vega, R. M. Rodriguez-Dagnino, M. A. Meneses-Nava, and S. Chavez-Cerda, "Mathieu functions, a visual approach," *American Journal of Physics*, vol. 71, no. 3, Mar. 2003.

[12] T. Tamir, "Characteristic exponents of Mathieu functions," *Math. Comput*., vol. 16, pp. 100-106, Jan. 1962.

[13] F. M. Monavar and P. Mousavi, "Stability and dispersion analysis of FDTD technique in sinusoidally stratified media," in Proc. *IEEE Antennas Propag. Soc. Int. Symp*. *(APS-URSI)*, 2014.

Fatemeh M. Monavar received the B.Sc. degree in Biomedical Engineering (Bioelectric) from Amirkabir University of Technology (Tehran Polytechnic), Tehran, Iran, in 2006 and the M.Sc. degree in Electrical Engineering (Communications-Fields and Waves) from Iran University of Science and Technology, Tehran, Iran, in 2010. She is currently pursuing the Ph.D. degree in Electrical Engineering (Electromagnetics and Microwave) at University of Alberta, Edmonton, AB, Canada.

Her research interests include antenna analysis and design, computational electromagnetics, and periodic structures.

Monavar was the recipient of NSERC Industrial Postgraduate Scholarship, Myer Horowitz Graduate Students' Association Scholarship and Queen Elizabeth II Graduate Scholarship-Doctoral level.

Gholamreza Moradi received his B.Sc. degree in Electrical Engineering from University of Tehran, in 1989, his M.Sc. degree in Electrical Engineering from Iran University of Science and Technology, Tehran in 1992 and his Ph.D. degree in Electrical Engineering from Tehran Polytechnic University, Tehran, Iran in 2002.

His main research interests are numerical

Electromagnetics, antennas, active microwave circuits, mm-wave circuits and systems, bioelectromagnetic and microwave measurements.

Moradi has published several papers in the refereed journals and the local and international conferences. Also, he has co-authored some books on his major including Advanced Microwave Engineering, Advanced Engineering Mathematics, Communication Transmission Lines, and Active Transmission Lines (in Persian). The latter was selected as the book of the year of Iran in 2008. He is currently an Associate Professor with the Electrical Engineering Department at Amirkabir University of Technology (Tehran Polytechnic), Tehran, Iran. He is now a Visiting Professor at the University of Alberta.

Pedram Mousavi received the B.Sc. (Hons.) degree in Telecommunication Engineering from Iran University of Science and Technology, Tehran, in 1995 and the M.Sc. and Ph.D. degrees from the University of Manitoba, Winnipeg, Canada, in 1997 and 2001 respectively, all in Electrical Engineering.

He is an Associate Professor with Departments of Mechanical Engineering and NSERC-AITF Industrial Research Chair in Intelligent Integrated Sensors and Antennas at the University of Alberta. Mousavi has over twelve years of entrepreneurial academic experience with start-up companies from the University of Waterloo and the University of Alberta. He founded Intelwaves Technologies based on the research that he initiated during his postdoctoral fellowship at the University of Waterloo.

His current mission is to foster a strong collaboration between industry and academia and stimulate more industry relevant research in wireless technologies. The research conducted through this industrial chair program will allow ICT (information and communications technology) innovations to be applied to the areas of intelligent integrated sensors and antennas to improve the productivity of the oil-energy sector and to sustain its growth. Mousavi has more than 120 refereed journal and conference articles and several patents in this field. His research interests are in the areas of advanced intelligent antenna, microwave and millimetre-waves circuits and systems, UWB radar systems and 3-D printing electronics.

An Efficient and Analytical Solution to the Integral on Truncated-Wedge ILDCs for Polygonal Surfaces

Chao Liu, Xiao Zhou, Wen M. Yu, and Tie J. Cui

State Key Lab of Millimeter Waves
Southeast University, Nanjing, 210096, China
liu.chao@seu.edu.cn, xiaozhou@seu.edu.cn, wmyu@seu.edu.cn, tjcui@ seu.edu.cn

Abstract ─ A new method is proposed to analytically evaluate the line integral on truncated-wedge incremental length diffraction coefficients (TW-ILDCs). By utilizing the coherence of a geometry, the trailing edges can be divided into several linear segments, and the line integrals can be reduced as the two end-point contributions for each segment based on the mathematical model derived in this paper. Thus, the efficiency is greatly enhanced in comparison with the traditional numerical techniques. Numerical results for the bistatic radar cross sections show excellent performance of the proposed method both in accuracy and efficiency.

Index Terms ─ Closed form, linear division, TW-ILDCs.

I. INTRODUCTION

It is well known that the surface integral in the physical theory of diffraction (PTD) has the following form:

$$I(k)=\int_{v_1}^{v_2}\int_{u_1}^{u_2} f(u,v)e^{jk\varphi(u,v)}dudv\,, \qquad (1)$$

in which k is a large wavenumber, $f(u,v)$ represents the amplitude of the integrand, and $\varphi(u,v)$ is the phase function, both of them have two arguments u and v. The integral on u is seen as the inner integral with the lower and upper limits u_1 and u_2; while the integral on v is thought to be the outer integral with limits v_1 and v_2. As is known, this PTD surface integral was firstly introduced by Ufimtsev, who has also reduced it into point contributions. But his reduction procedure is a directly surface-to-point process, lacking the surface-to-line step, which may contribute to 'very complicated and immense equations' [1]. Thu, Ufimtsev's result is not very practical [3].

Therefore, there have been numerous contributions to better evaluate the inner integral in (1) in the past decades [2]-[10]. The theory of incremental length diffraction coefficients (ILDCs) [2] proposed by Mitzner has made significant improvement for such evaluation. In ILDCs, the two associated faces of a wedge are assumed to be two half-planes based on high frequency localization phenomenon. Hence, the inner integral limit is from zero to infinity. Meanwhile, a function v_B [11] is used to describe the fringe-wave surface current $f(u,v)$, the variable of which only contains u without v in this case, and the phase function $\varphi(u,v)$ can be expressed separately by $\varphi(u)$ and $\varphi(v)$ for the inner and outer integral. Thus, the inner integral in (1) is able to be reduced into closed form, and $I(k)$ can be evaluated analytically for straight wedges. For curved wedges, the stationary phase method [13] can be used to asymptotically reduce the outer integral into point contributions. Hence, ILDCs is an efficient algorithm, and has been successfully applied to design B-2 stealth aircraft [14].

However, some problems exist in ILDCs. Firstly, singularities emerge in some combinations of incidence and observation directions. The reason, as pointed out by Michaeli, is the inappropriate selection of the coordinate system [3]. Unlike ILDCs, who chooses the direction normal to the wedge edge as the inner integral direction, Ref. [3] has selected the grazing diffracted direction, which is a more natural way as pictured by the ray behavior in the geometrical theory of diffraction (GTD) [15]. As a result, most singularities were removed except the non-removable Ufimtsev singularity. Secondly, the half-plane assumption is in contrast to real conditions, which will influence the accuracy especially when the observation direction is close to the grazing diffracted ray [9]. This problem of ILDCs leads to the necessity to consider the second-order diffraction. In this circumstance, the upper limit of the inner integral is a finite value because the fringe wave surface current incremental strips will be truncated when hitting the second-order diffraction points. Work related to solve this kind of inner integral includes Refs. [6], [7] for the half-plane, and [8] for a right-angled wedge. Though the expression for a wedge with arbitrary angle was firstly

Submitted On: November 30, 2016
Accepted On: December 10, 2016

gained by Michaeli [9], the non-removable singularities still exist due to the improper mathematical derivation procedure. This difficulty was finally overcome by Johansen [10] with no non-removable singularities emerged in his result. Therefore, an analytical, more accurate and robust evaluation of the inner integral in (1) than ILDCs is achieved. Thus, the method in [10], named as truncated-wedge incremental length diffraction coefficients (TW-ILDCs), has been widely used and implemented in Xpatch [16] and GRASP [17].

However, compared with ILDCs, when considering the second-order diffraction, the outer integral in (1) cannot be analytically evaluated even for a straight wedge, because the length of each incremental strip is different and depends on the geometry of an object. To calculate such an integral, the numerical quadrature method has been used [16], [18], [19]. In Ref. [16], to implement TW-ILDCs in Xpatch, sample points on a wedge's leading edge are taken, and the incremental strips of the fringe wave surface currents, emanated from each sample point, will travel until hitting a point on another discontinuous edge. Obviously, the length of the incremental strip has to be calculated again for different sample points and incident angles. In Ref. [18] the distance between every two sample points is set to be $\lambda/10$, which is a frequency-related value and a similar value is taken in [19] as well. Thus, the final result of $I(k)$ is the summation of the diffraction coefficients calculated from all sample points. Consequently, to deal with such highly oscillatory integral, the computation time will increase largely as the frequency increases. To accelerate this numerical technique, a fixed truncated length TW-ILDCs method was proposed based on the idea of rectangular strip [7]. Similar to ILDCs, the amplitude of the integrand in the outer integral in (1) is thereby constant and this line integral can be reduced to closed form resultantly. Though the efficiency was improved by this approach, the accuracy cannot be guaranteed which has been illustrated by the examples in Ref. [18].

In this paper, we propose a new method that can rigorously reduce this line integral into a closed-form expression for planar structures. For the commonly used triangular patch mesh, it is found that the trailing edges can be divided into several linear segments, and on each of them, the outer integral in (1) can be evaluated analytically. The mathematical model required in this process is derived in details. Meanwhile, the efficiency can be greatly improved in comparison with the numerical technique.

This paper is organized as follows. In Section II, a mathematical model referring to the integral on the complementary error function is introduced. Then its application to PTD is described in Section III, including details in integral reduction. Numerical results are given in Section IV to illustrate the validation of the proposed method. Finally, Section V gives the concluding remarks.

II. MATHEMATICAL MODEL

Consider the integral form given below:

$$I(a_1,b_1,a_2,b_2)=\int F\left(\sqrt{a_1z+b_1}\right)e^{jk(a_2z+b_2)}dz, \qquad (2)$$

in which z is the integral variable, a_1,b_1,a_2,b_2 are the constant terms, and $F(x)$ is the modified Fresnel integral [9]. The aim here is to rigorously reduce the integral (2) into a closed form.

A. The general case

Note that the modified Fresnel integral has a relationship with the complementary error function [20] $F(z)=0.5erfc\left(\sqrt{j}z\right)e^{jz^2}$, then (2) can be rewritten as:

$$\begin{aligned} &I(a_1,b_1,a_2,b_2)\\ &=2\int erfc\left(\sqrt{j(a_1z+b_1)}\right)e^{j\left[(a_1+ka_2)z+(b_1+kb_2)\right]}dz. \end{aligned} \qquad (3)$$

By using the approach of integrating by parts, and noting that $erfc'(x)=-2e^{-x^2}/\sqrt{\pi}$, (3) can be transformed into:

$$\begin{aligned} &I(a_1,b_1,a_2,b_2)\\ &=\frac{2e^{j(b_1+kb_2)}}{j(a_1+ka_2)}\left[erfc\left(\sqrt{j(a_1z+b_1)}\right)e^{j(a_1+ka_2)z}\right.\\ &\left.+\sqrt{\frac{j}{\pi}}a_1e^{-jb_1}\int\frac{e^{jka_2z}}{\sqrt{(a_1z+b_1)}}dz\right]. \end{aligned} \qquad (4)$$

For the integral contained in (4), it has,

$$\begin{aligned} &\int\frac{e^{jka_2z}}{\sqrt{(a_1z+b_1)}}dz\\ &=-\frac{\sqrt{\pi}}{a_1}\sqrt{j\frac{a_1}{ka_2}}e^{-\frac{jka_2b_1}{a_1}}erfc\left(\sqrt{-\frac{jka_2}{a_1}(a_1z+b_1)}\right). \end{aligned} \qquad (5)$$

Therefore, based on the relationship between modified Fresnel integral and the error function, the final result of (2) can be obtained by taking (5) into (4) as:

$$\begin{aligned} &I(a_1,b_1,a_2,b_2)=\frac{4e^{jk(a_2z+b_2)}}{j(a_1+ka_2)}\\ &\cdot\left[F\left(\sqrt{a_1z+b_1}\right)-j\sqrt{\frac{a_1}{ka_2}}F\left(\sqrt{-\frac{ka_2}{a_1}(a_1z+b_1)}\right)\right]. \end{aligned} \qquad (6)$$

B. The singular case

In (3), when $a_1+ka_2=0$, the integral will be changed as the following form:

$$I(a_1,b_1,a_2,b_2)=2e^{j(b_1+kb_2)}\int erfc\left(\sqrt{j(a_1z+b_1)}\right)dz. \qquad (7)$$

Referring to Ref. [21], the result of integral

$\int z\cdot erfc(z)dz$ is listed in its table. Noting that $0.5\int erfc\left(\sqrt{z}\right)dz=\int z\cdot erfc(z)dz$, it is easy to get the value of (7) by variable substitution:

$$I\left(a_1,b_1,a_2,b_2\right)=2e^{j(b_1+kb_2)}\cdot\left[\frac{1}{a_1}\left(\left(a_1z+b_1\right)+\frac{j}{2}\right)\cdot erfc\left(\sqrt{j\left(a_1z+b_1\right)}\right)-\sqrt{\frac{j\left(a_1z+b_1\right)}{\pi}}e^{-j\left(a_1z+b_1\right)}\right]. \quad (8)$$

III. APPLICATION TO PTD

A. The line integral on TW-ILDCs

The geometry of a perfect conducting wedge with two finite sized polygonal planes is shown in Fig. 1. The points B and C are two points on the leading edge, from which the fringe wave incremental strips emanate, along the grazing diffracted direction $\hat{\sigma}$, hit an edge at point B' and C'. The dashed lines BB' and CC' are their propagation paths, whose lengths are l_B and l_C, respectively. And the equivalent edge currents are distributed on the polygon face AA'B'C'D. Therefore, edges A'B', B'C' and C'D are the so-called trailing edges.

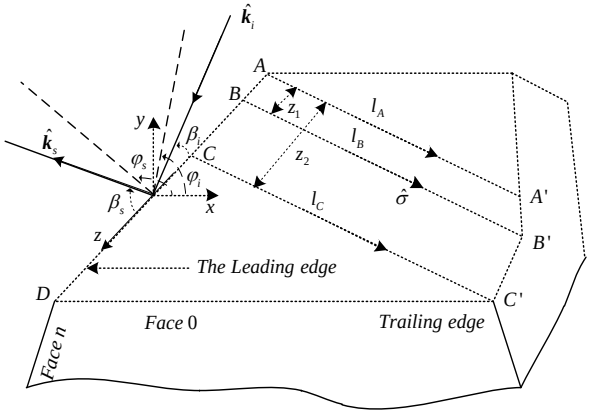

Fig. 1. The geometry of a perfectly conducting wedge. The dashed lines on the wedge represent the propagation paths of the fringe wave incremental strips. Segments AB and BC are the projections of line segments A'B' and B'C' on the leading edge AD. φ_i and φ_s are the angles from the *x* axis to the projections of $\hat{\boldsymbol{k}}_i$ and $\hat{\boldsymbol{k}}_s$ on the *xy* plane, β_i and β_s are the angles from the leading edge to $\hat{\boldsymbol{k}}_i$ and $\hat{\boldsymbol{k}}_s$, respectively.

The fringe-wave field is expressed by the radiation integral [12] as:

$$\boldsymbol{E}^{fw}=jk\int\left[ZI_T\hat{\boldsymbol{k}}_s\times\left(\hat{\boldsymbol{k}}_s\times\hat{\boldsymbol{t}}\right)+M_T\hat{\boldsymbol{k}}_s\times\hat{\boldsymbol{t}}\right]\frac{e^{-jkR}}{4\pi R}dz, \quad (9)$$

where Z_0 is the impedance, $\hat{\boldsymbol{t}}=\hat{\boldsymbol{z}}$, the direction of the leading edge, and M_T, I_T are the truncated equivalent magnetic and electric currents [10], having the expressions that $M_T=M_{ut}-M_{cor}$, $I_T=I_{ut}-I_{cor}$, in which M_{ut} and I_{ut} represent the untruncated equivalent magnetic and electric currents and their expressions can be obtained in Ref. [3], while M_{cor} and I_{cor} are the correction terms when considering partly the secondary diffraction, respectively.

Since M_{ut} and I_{ut} are constants for a wedge edge, the integrals on them can be expressed analytically. Hence, the main work here is to evaluate the integral on the correction terms M_{cor} and I_{cor}:

$$\boldsymbol{E}_{cor}^{fw}=jk\frac{e^{-jkR}}{4\pi R}\cdot\left[Z_0\hat{\boldsymbol{k}}_s\times\left(\hat{\boldsymbol{k}}_s\times\hat{\boldsymbol{t}}\right)\int_C I_{cor}\exp\left(jk(-\hat{\boldsymbol{k}}_i+\hat{\boldsymbol{k}}_s)\cdot\boldsymbol{z}\right)dz+\hat{\boldsymbol{k}}_s\times\hat{\boldsymbol{t}}\int_C M_{cor}\exp\left(jk(-\hat{\boldsymbol{k}}_i+\hat{\boldsymbol{k}}_s)\cdot\boldsymbol{z}\right)dz\right]. \quad (10)$$

The expressions of M_{cor} and I_{cor} are obtained from Ref. [10] and listed as:

$$M_{cor}=\frac{2Z_0\sin\varphi_s\hat{\boldsymbol{z}}\cdot\boldsymbol{H}^i\exp[jL(\mu-1)]}{jk\sin\beta_s\sin\beta_i}\cdot\left[\frac{-sign[cos(\varphi_i/2)]}{\mu+\cos\varphi_i}F\left(\sqrt{2L}\left|\cos(\varphi_i/2)\right|\right)+\left(\frac{\sqrt{1-\mu}}{\sqrt{2}\left(\mu+\cos\varphi_i\right)\cos(\varphi_i/2)}-\frac{\sqrt{2}\sin(\pi/n)}{n\sqrt{1-\mu}\left(\cos(\pi/n)-\cos(\varphi_i/n)\right)}\right)\cdot F\left(\sqrt{L(1-\mu)}\right)\right], \quad (11)$$

$$I_{cor}=\frac{2sign[cos(\varphi_i/2)]\exp[jL(\mu-1)]}{jk\sin\beta_i\left(\mu+\cos\varphi_i\right)}\cdot\left[\frac{\sin\varphi_i\hat{\boldsymbol{z}}\cdot\boldsymbol{E}^i}{Z_0\sin\beta_i}-\left(\cot\beta_i\cos\varphi_i+\cot\beta_s\cos\varphi_s\right)\hat{\boldsymbol{z}}\cdot\boldsymbol{H}^i\right]\cdot F\left(\sqrt{2L}\left|\cos(\varphi_i/2)\right|\right)+\sqrt{2(1-\mu)}\cdot\left[-\frac{\sin(\varphi_i/2)\hat{z}\cdot\boldsymbol{E}^i}{Z_0\sin\beta_i}+\frac{\hat{z}\cdot\boldsymbol{H}^i}{2\cos(\varphi_i/2)}\cdot\left(\cot\beta_i\cos\varphi_i+\cot\beta_s\cos\varphi_s\right)+\frac{\sin(\pi/n)\left(\mu+\cos\varphi_i\right)\left(\cot\beta_i-\cot\beta_s\cos\varphi_s\right)\hat{z}\cdot\boldsymbol{H}^i}{n\left(\cos(\pi/n)-\cos(\varphi_i/n)\right)(1-\mu)}\right]\cdot F\left(\sqrt{L(1-\mu)}\right)\right]. \quad (12)$$

The argument L in the modified Fresnel integral has the expression:

$$L = kl\sin^2\beta_i, \tag{13}$$

in which l is the truncated length for each incremental strip, and the angle-related terms for both excitation and observation, such as β_i, φ_i, β_s, φ_s and μ, are the same as these defined in Ref. [10].

Taking (11), (12) into (10), it can be found the key point when dealing with the integrals in (10) is to calculate the two integrals below:

$$T_1 = \int_C F\left(\sqrt{2L}\left|\cos(\varphi_i/2)\right|\right) \cdot \exp\left[jL(\mu-1)+jk(-\hat{\boldsymbol{k}}_i+\hat{\boldsymbol{k}}_s)\cdot\boldsymbol{z}\right]dz, \tag{14}$$

$$T_2 = \int_C F\left(\sqrt{L(1-\mu)}\right) \cdot \exp\left[jL(\mu-1)+jk(-\hat{\boldsymbol{k}}_i+\hat{\boldsymbol{k}}_s)\cdot\boldsymbol{z}\right]dz. \tag{15}$$

B. Linear division and representation

When the mesh of an object is based on triangular patches, each edge of the meshed model is a linear segment. Therefore, within each linear segment, the truncated length of any point on the corresponding leading edge segment can be expressed as a linear function of the point's position on the leading edge. As illustrated by Fig. 1, take edge BC as an example. For face 0, the distance between points A and B is z_1, between points A and C is z_2, the distance between point A and any point on edge AD is assumed to be z, and the position vector is z. For face n, it has $\hat{z} \to -\hat{z}$; hence, the starting point of the wedge edge should also be changed. The truncated length of each point on edge BC is:

$$l = \frac{l_C - l_B}{z_2 - z_1}(z - z_1) + l_B. \tag{16}$$

Thus, the slope for this trailing edge is given as $k_l = (l_C - l_B)/(z_2 - z_1)$, then l is further written as $l = k_l z + c_l$, where c_l can be derived from (16).

As a result, the variable L in (18) and (19) can be represented as:

$$L = k_L z + c_L, \tag{17}$$

in which $k_L = kk_l\sin^2\beta_i$, $c_L = kc_l\sin^2\beta_i$.

C. Integral reduction

Taking (17) into (14) and (15), T_1 and T_2 are rewritten as:

$$T_1 = \int F\left(\sqrt{k_L(1+\cos\varphi_i)z + c_L(1+\cos\varphi_i)}\right) \cdot e^{jk\left\{\left[\frac{k_L(\mu-1)}{k}+\cos\beta_s-\cos\beta_i\right]z+\frac{c_L(\mu-1)}{k}\right\}}dz, \tag{18}$$

$$T_2 = \int F\left(\sqrt{k_L(1-\mu)z + c_L(1-\mu)}\right) \cdot e^{jk\left\{\left[\frac{k_L(\mu-1)}{k}+\cos\beta_s-\cos\beta_i\right]z+\frac{c_L(\mu-1)}{k}\right\}}dz. \tag{19}$$

Obviously, the integrals (18) and (19) have the same form as (2), so the results of them have the same form as (6) and the values of a_1, b_1, a_2, and b_2 can be determined for T_1 and T_2 in this condition. For T_1,

$$a_1 = k_L(1+\cos\varphi_i), b_1 = c_L(1+\cos\varphi_i)$$
$$a_2 = \frac{k_L}{k}(\mu-1) - \cos\beta_i + \cos\beta_s, b_2 = \frac{(\mu-1)}{k}c_L; \tag{20}$$

and for T_2,

$$a_1 = k_L(1-\mu), b_1 = c_L(1-\mu)$$
$$a_2 = \frac{k_L}{k}(\mu-1) - \cos\beta_i + \cos\beta_s, b_2 = \frac{(\mu-1)}{k}c_L. \tag{21}$$

Consequently, for each face of a wedge, the line integral on TW-ILDCs is successfully reduced into a closed-form expression in terms of the modified Fresnel integral.

IV. NUMERICAL RESULTS

In this section, the good performance of the proposed method will be demonstrated via calculating the bistatic radar cross sections on a trapezoid body. The results of numerical TW-ILDCs method are also exhibited as comparisons.

The geometry of the object is illustrated in Fig. 2. The incident angle is given by $\theta_i = 60^\circ$ and $\varphi_i = 30^\circ$, and the observation angles are determined by $\theta_s = 90^\circ$ and $\varphi_s = 0 \sim 360^\circ$ using an angular resolution of 0.25°. The working frequency is set to be 3 GHz. Numerical TW-ILDCs are performed using the method presented in [18], in which the $\lambda/10$ mesh on wedge edge is taken to give enough accuracy.

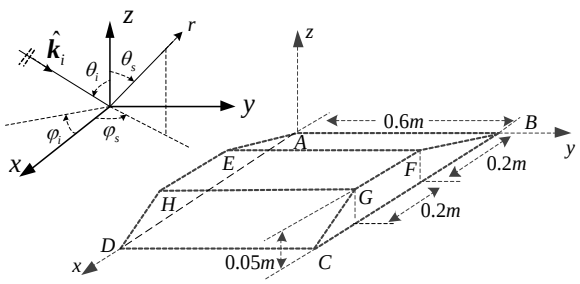

Fig. 2. Perfectly conducting object. The bottom face is ABCD, a 0.6m × 0.6m square. The upper face is EFGH, the front and back side faces are CDHG and ABFE. θ_i, θ_s are from the z axis to the incident and scattering directions, φ_i and φ_s are from the x axis to the projections of the incident and scattering directions on xy plane, respectively.

Considering the linear division process for all discontinuous edges, the trailing edges of edges AE, BF, EH and FG can only be divided into one linear segment for their two faces, thus these four wedge edges do not need to be divided. For the upper face of edge AB, the trailing edges are divided into four linear segments: EA, HE, DH, part of CD. Thus, the outer integral in (1) can be written as the summation of four sub-integrals on these four linear segments. For the bottom face of AB, the trailing edges are: AD and part of CD. Hence AB should be divided into two parts, and the outer integral in (1) is the summation of two sub-integrals on these two linear segments. The division of BC, CD, CG, EF, GH and DH are similar to AB.

As can be seen from Figs. 3-4, the results of the proposed method are almost the same as the numerical TW-ILDCs except some small discrepancies which are possibly due to the slight numerical errors in the calculation process. Moreover, the results of multi-level fast multipole method (MLFMM) minus PO are also given as a reference, in which the results of MLFMM are obtained by software FEKO and the reason for the difference between the proposed method and MLFMM minus PO is that the higher-order and vertex diffraction contributions are not considered by both numerical TW-ILDCs and the proposed method.

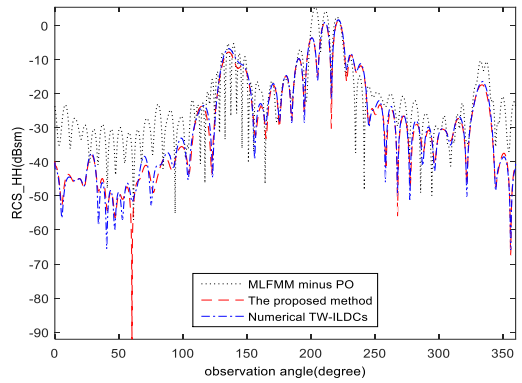

Fig. 3. HH polarization bistatic radar cross section results.

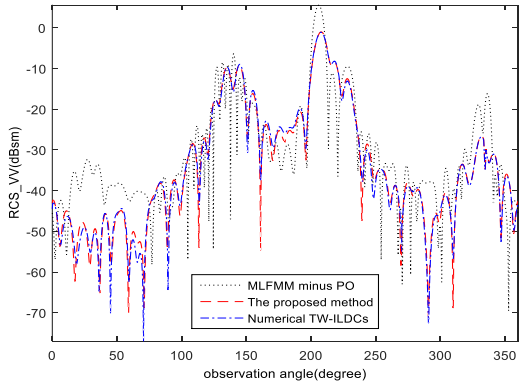

Fig. 4. VV polarization bistatic radar cross section results.

Meanwhile, to illustrate the efficiency of the proposed method and numerical TW-ILDCs, the computation time is listed in Table 1.

Table 1: Computation time consumed by diffraction

Frequency (GHz)	Computation Time (s)	
	The Proposed Method	Numerical TW-ILDCs
3.0	0.827	3.276
10.0	0.905	10.701
30.0	0.905	31.121

It can be seen that the time needed by numerical TW-ILDCs is increased as the frequency increases; while the computation time of the proposed method is relatively stable and takes very small part of that of numerical TW-ILDCs.

V. CONCLUSION

In this paper, a new method is proposed to analytically treat the line integral on TW-ILDCs. Based on the triangular patch mesh, the trailing edges corresponding to a leading edge can be divided into several linear segments, and the line integral can then be reduced to an analytical form in terms of the modified Fresnel integral among the linear segments. Thus, the efficiency has been improved significantly compared with the traditional numerical quadrature method. The future work will focus on the higher-order diffraction contributions to develop a more accurate algorithm.

REFERENCES

[1] P. Y. Ufimtsev, "Method of edge waves in the physical theory of diffraction," *U.S. Air Force*, Foreign Technology Div., Wright-Patterson AFB, OH, Sept. 7, 1971 (transl. from Russian).

[2] K. M. Mitzner, *Incremental length diffraction coefficients*, Report AFAL-TR-73-296, Northrop Corporation, 1974.

[3] A. Michaeli, "Elimination of infinities in equivalent edge currents, part I: Fringe current components," *IEEE Trans. Antennas and Propagat.*, vol. 34, no. 7, pp. 912-918, July 1986.

[4] R. A. Shore and A. D. Yaghjian, "Incremental diffraction coefficients for planar surfaces," *IEEE Trans. Antennas and Propagat.*, vol. 37, no. 1, pp. 55-70, Jan. 1988.

[5] R. A. Shore and A. D. Yaghjian, "Correction to Incremental diffraction coefficients for planar surfaces," *IEEE Trans. Antennas and Propagat.*, vol. 37, pp. 1342, Jan. 1989.

[6] O. Breinbjerg, "Higher-order equivalent edge currents for fringe wave radar scattering by perfectly conducting polygonal plates," *IEEE Trans. Antennas and Propagat.*, vol. 40, pp. 1543-1544, Dec. 1992.

[7] R. A. Shore and A. D. Yaghjian, "Incremental diffraction coefficients for plane conformal strips with application to bistatic scattering from the disk," *J. Electromagn. Waves Applicat.*, vol. 6, no. 3, pp. 359-396, Mar. 1992.

[8] M. G. Cote, M. B. Woodworth, and A. D. Yaghjian, "Scattering from the perfectly conducting cube," *IEEE Trans. Antennas and Propagat.*, vol. 36, pp. 1321-1329, Sept. 1988.

[9] A. Michaeli, "Equivalent currents for second-order diffraction by the edges of perfectly conducting polygonal surfaces," *IEEE Trans. Antennas and Propagat.*, vol. 35, no. 2, pp. 183-190, Feb. 1987.

[10] P. M. Johansen, "Uniform physical theory of diffraction equivalent edge currents for truncated wedge strips," *IEEE Trans. Antennas and Propagat.*, vol. 44, no. 7, pp. 989-995, July 1996.

[11] W. Pauli, "On asymptotic series for functions in the theory of diffraction of light," *Phys. Rev.*, vol. 54, pp. 924-931, Dec. 1938.

[12] A. Michaeli, "Equivalent edge currents for arbitrary aspects of observation," *IEEE Trans. Antennas and Propagat.*, vol. 32, pp. 252-258, Mar. 1984.

[13] V. A. Borovikov, "Uniform stationary phase method," *IEEE Electromagn. Waves*, 1994.

[14] P. Ya. Ufimtsev, "The 50-year anniversary of the PTD: Comments on the PTD's origin and development," *IEEE Antennas and Propagat. Magazine*, vol. 55, no. 3, June 2013.

[15] G. L. James, *Geometrical Theory of Diffraction for Electromagentic Waves*. Hertfordshire, England: Peter Peregrinus, 1976.

[16] J. T. Moore, A. D. Yaghjian, and R. A. Shore, "Shadow boundary and truncated wedge ILDCs in Xpatch," *in Proc. IEEE Antennas and Propag. Society Int. Symp.*, 2005, vol. 1, pp. 10-13, July 1986.

[17] R. A. Shore and A. D. Yaghjian, "A comparison of high-frequency scattering determined from PO fields enhanced with alternative ILDCs," *IEEE Trans. Antennas and Propagat.*, vol. 52, no. 1, pp. 336-341, Jan. 2004.

[18] B. Robert and F. E. Thomas, "Investigation of equivalent edge currents for improved radar cross section predictions," *Proc. 8th Eur Conf. Antennas Propag. (EuCAP)*, pp. 2321-2325, 2014.

[19] P. C. Gao, Y. B. Tao, Z. H. Bai, and H. Lin, "Mapping the SBR and TW-ILDCs to heterogeneous CPU-GPU architecture for fast computation of electromagnetic scattering," *Progress Electromagn. Res. (PIER)*, vol. 122, pp. 137-154, 2012.

[20] M. Abramowitz and I. A. Stegun, *Handbook of Mathematical Functions*. Norwood, MA, USA: Dover, 1972.

[21] E. W. Ng and M. Geller, "A table of integrals of the error functions," *Joural of Research of the National Bureau of Standards - B. Mathematical Sciences*, vol. 73B, no. 1, Jan.-Mar. 1969.

Chao Liu was born in Jiangsu, China, in July 1992. He received the B.E. degree in Electronics and Information Engineering from Xidian University, Xi'an, China, in 2014. Currently, he is pursuing the M.Sc. degree in Electric Engineering at Southeast University, Nanjing, China. His research interests include high-frequency method and hybrid method for electromagnetic scattering and radiations.

Xiao Zhou was born in Anhui, China, in June 1990. He received the B.E. degree in Electrics and Information Engineering from Anhui University, Hefei, China, in 2009, and the Ph.D. degree in Electric Engineering at Southeast University, Nanjing, China, in 2016. He is currently working in Huawei Cooperation. His research interests include high-frequency method and hybrid method for electromagnetic scattering and radiations.

Wen Ming Yu was born in Zhuji, Zhejiang, China, in 1980. He received the B.S. and Ph.D. degrees in Electrical Engineering from Nanjing University of Science and Technology, Nanjing, China, in 2002 and 2007, respectively. Currently, he is an Associate Professor with Southeast University, Nanjing, China.

Tie Jun Cui (M'98–SM'00–F'15) received the B.Sc., M.Sc., and Ph.D. degrees in Electrical Engineering from Xidian University, Xi'an, China, in 1987, 1990, and 1993, respectively.

In March 1993, he joined the Department of Electromagnetic Engineering, Xidian University, and was promoted as an Associate Professor in November 1993. From 1995 to 1997, he was a Research Fellow with the Institut fur Hochstfrequenztechnik und Elektronik (IHE), University of Karlsruhe, Karlsruhe, Germany. In July 1997, he joined the Center for Computational Electromagnetics, Department of Electrical and Computer Engineering, University of Illinois at Urbana-

Champaign, Champaign, IL, USA, first as a Postdoctoral Research Associate and then as a Research Scientist. In September 2001, he became a Cheung-Kong Professor with the Department of Radio Engineering, Southeast University, Nanjing, China. Currently, he is an Associate Dean with the School of Information Science and Engineering and an Associate Director of the State Key Laboratory of Millimeter Waves. He has authored over 250 peer-review journal papers in Science, PNAS, Nature Communications, Physical Review Letters, IEEE TRANSACTIONS, etc. He is the Co-Editor of Metamaterials Theory, Design, and Applications (Springer, 2009), and the author of six book chapters. His research interests include metamaterials, computational electromagnetic, wireless power transfer, and millimeter-wave technologies.

Cui is an Active Reviewer for Science, Nature Materials, Nature Physics, Nature Communications, Physical Review Letters, and a series of IEEE Transactions. He was an Associate Editor in the IEEE Transactions on Geoscience and Remote Sensing. He served as an Editorial Staff in the IEEE Antennas and Propagation Magazine, and is in the Editorial Boards of Progress in Electromagnetic Research (PIER) and Journal of Electromagnetic Waves and Applications. He served as a General Co-Chair of the International Workshops on Metamaterials (META2008, META2012), TPC Co-Chair of Asian Pacific Microwave Conference (APMC2005) and Progress in Electromagnetic Research Symposium (PIERS2004). He was awarded a Research Fellowship from the Alexander von Humboldt Foundation, Bonn, Germany, in 1995. He received the Young Scientist Award from the International Union of Radio Science (URSI) in 1999 and was awarded a Cheung Kong Professor under the Cheung Kong Scholar Program by the Ministry of Education, China, in 2001. He received the National Science Foundation of China for Distinguished Young Scholars in 2002, the Special Government Allowance awarded by the Department of State, China, in 2008, and the Award of Science and Technology Progress from Shanxi Province Government in 2009. He was awarded a May 1st Labour Medal by Jiangsu Province Government in 2010. He received the First Prize of Natural Science from Ministry of Education, China, in 2011, and the Second Prize of National Natural Science, China, in 2014. His researches have been selected as one of the 10 Breakthroughs of China Science in 2010, Best of 2010 in New Journal of Physics, Research Highlights in Europhysics News, Journal of Physics D: Applied Physics, Applied Physics Letters, and Nature China. His work has been reported by Nature News, Science, MIT Technology Review, Scientific American, New Scientists, etc.

A Regularized Source Current Reconstruction Method for Reactive Near Field to Far Field Transformation

M. Bod, R. Sarraf-Shirazi, GH. Moradi, and A. Jafargholi

Department of Electrical Engineering
Amirkabir University of Technology, Tehran, Iran
(mbod, sarraf, ghmoradi, amirajafargholi)@aut.ac.ir

Abstract ─ The source current reconstruction method (SRM) is based on reconstructing equivalent current from the known electric field and can be used as a method of near field to far field transformation. In this paper for the first time the reactive near field (RNF) to far field (FF) transformation based on SRM is carefully studied. It is shown that in the RNF region, the singular values of the SRM transformation matrix can magnify the evanescent modes of RNF region and unstable the SRM iterative solvers. Therefore, in this paper for RNF/FF transformation a regularized SRM is proposed and the equivalent magnetic current of an antenna under test is reconstructed from the Tikhonov SRM equation. The regularization parameter of the Tikhonov equation is determined by the L-curve method. The effect of near field distance and noise on the accuracy of far field transformation of the proposed algorithm are studied in two different antenna simulations. It is shown that in all cases in the RNF region a regularized SRM have more stable behavior and more accurate results.

Index Terms ─ Reactive near field, regularization, source current reconstruction, Tikhonov inverse problem.

I. INTRODUCTION

One of the important parameters to characterize the antenna performance is its far field radiation pattern which is measured in an anechoic chamber. In practice, due to size limitation, it is not always possible to measure the far field radiation pattern of the antenna under test (AUT). Therefore, the near field radiation pattern of the AUT is measured and the far field radiation pattern is reconstructed by means of Near Field (NF) to Far Field (FF) transformation [1].

In recent years, many different techniques for NF/FF transformation are developed [1]-[10]. The earliest works are based on the wave mode expansion, in which the measured near field data are used to determine the wave mode coefficients of the AUT [1], [2]. By finding theses wave mode coefficients, it is possible to determine the antenna radiation pattern at any desired distance. However, in these techniques, the spatial sampling rate should satisfy Nyquist criterion and reducing the number of sampling points from that criterion can deteriorate the transformation procedure. Furthermore, the modal techniques are limited to canonical acquisition surfaces (planar, cylindrical or spherical measurements) [3].

Recently, another NF/FF transformation technique, called the sources reconstruction method (SRM), has been proposed [3]-[12]. In this technique by using an equivalence principle, the equivalent currents at the antenna aperture can be reconstructed from the known NF data. By reconstructing the equivalent current at the antenna aperture it is possible to determine the radiation pattern of the AUT at any desired distance.

SRM is, in fact, an inverse radiation problem which is based on an electric field integral equation and is solved by the inverse method of moment techniques [8]. In comparison to the modal methods, SRM is more accurate, more stable and more robust but have a high computational cost associated to the solving of complex integral equations [3]. Furthermore, SRM is based on the full wave equations which are valid in all of the space around the AUT, while modal expansion based NF/FF transformation can be applied outside the minimum sphere enclosing AUT [3].

Until recently, the NF/FF transformation are mostly done with data that measured in the radiative near field region [13]. In fact, unavoidable coupling, reflection, and interferences between the AUT and typical electromagnetic field probes enforce the measurement to be done at distance more than one wavelength from the AUT aperture [13]. With the development of optic sensors and equipment, the reactive near field (RNF) measurement is also possible [13]-[15]. With such progressions in the measurement systems, a method for RNF/FF transformation can drastically reduce the dimensions of test facilities and test costs and increase measurement speeds. However, up to the authors' knowledge, the RNF/FF transformation are not studied well until know.

A brief report about the very near field to far field transformation with the modal techniques can be found in [14]. An accurate RNF/FF transformation is obtained

Submitted On: July 6, 2016
Accepted On: December 24, 2016

in this paper by the field sampling strategy that the authors have proposed. In fact, in this paper, the field sampling positions have been optimized for each antenna in a way that creates a transformation matrix with the most convenient singular value. This will reduce the effects of evanescent modes of RNF region as shown in this paper.

A RNF/FF transformation based on SRM technique is reported in [12]. In this paper, it has been shown that the field transformation error of the conventional SRM is increased drastically in the RNF region. Therefore, a dual equation formulation for SRM technique has been proposed. One can be shown that the proposed formulation of SRM technique can noticeably improve the condition number of field transformation matrix and therefore reduce the effects of evanescent modes but this formulation has very high computational cost.

In this paper, the effect of RNF data on the SRM field transformation is completely studied. It is shown that if the singular values of the SRM field transformation matrix are not treated well, the evanescent modes of the RNF region will create instability in the FF transformation. Therefore, in order to reconstruct the FF radiation from the RNF data, a regularized SRM is proposed in the paper. The necessity of regularization for RNF/FF applications are demonstrated both analytically and experimentally. The effect of near field distance and noise on the accuracy of the proposed regularized SRM are studied in two different antenna simulations. It is shown that in all cases, in the RNF region the regularized SRM have more stable and more accurate results.

II. DESCRIPTION OF THE METHOD

A. Source current reconstruction method

The SRM is based on the electromagnetic equivalence principle which allows one to establish an equivalent problem of an AUT radiation by using equivalent electric and magnetic currents [8]. According to this principle, the radiated fields outside the domain containing the equivalent currents are the same in both the original and the equivalent problem. This basic idea is used in the SRM to develop a set of integral equations in which the known electric field is related to the radiation of equivalent current at the AUT aperture.

SRM integral equation can be used to reconstruct both equivalent electric and magnetic currents [8]. However, in the field transformation applications for the simplification of equations, one can assume that a half space perfect electric conductor is placed at the AUT aperture in the xy-plane and reconstruct only an equivalent magnetic current by the following integral equation [4]:

$$\bar{E}(\bar{r}) = -\frac{1}{4\pi}\int_{S'} \bar{M}_{eq}(\bar{r}') \times \nabla' G_M(\bar{r},\bar{r}')\ ds', \qquad (1)$$

in which $E(r)$ is the known electric field at the observation point r, M_{eq} is the equivalent magnetic current at the antenna aperture and G_M is the appropriate dyadic Green function relating the magnetic current and fields in free space.

This integral equation should be discretized and solved via standard method of moments (MOM). For this purpose, the antenna aperture should be meshed with triangular facets as shown in Fig. 1, and the equivalent magnetic current M_{eq} is approximated by a finite sum of Rao-Wilton-Gilson (RWG) subdomain basis functions as follows [9]:

$$\vec{M}_{eq}(\vec{r}') = \sum_{n=1}^{N} I_{M_n} \cdot \vec{f}_n(\vec{r}'), \qquad (2)$$

in which I_M is the unknown coefficient that should be determined by the method of moment and $\vec{f_n}(\vec{r'})$ are the well-known RWG basis functions defined at each triangular facets as shown in Fig. 2 [9].

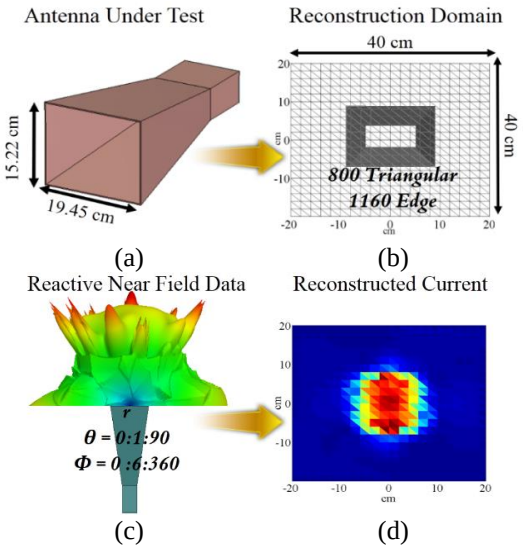

Fig. 1. Source current reconstruction method elements. (a) A horn antenna is selected as an AUT, (b) the RWG facets at the horn antenna aperture, (c) the hemisphere acquisition of reactive near field with λ/2 radius from the antenna aperture, and (d) the reconstructed equivalent magnetic current at the antenna aperture.

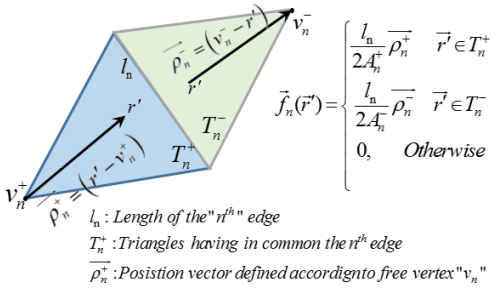

Fig. 2. RWG basis function definition on the triangular facets.

By adding a set of known electric fields at different positions in Equation (1) and using Equation (2), a matrix equation can be constructed as follows:

$$\begin{bmatrix} H_{\theta,\mathrm{I}_{M_n}} \\ H_{\phi,\mathrm{I}_{M_n}} \end{bmatrix}_{2m\times n} \times \left[\mathrm{I}_{M_n}\right]_{n\times 1} = \begin{bmatrix} E_\theta \\ E_\phi \end{bmatrix}_{2m\times 1}, \quad (3)$$

where m is the number of measured electric field points, n is the number of unknown coefficients (total edges in RWG basis function) and H is the discretized impedance matrix which has $2\times m$ column and n rows.

The system of Equations (3) is overdetermined because the number of known field is greater than unknown coefficients. Therefore, Equation (3) should be solved by a least square solver which minimize the following equation:

$$I_M = \arg\min_{\mathrm{I}_M} \left\{ \left\| E - H \times I_M \right\|_2^2 \right\}. \quad (4)$$

This least square equation can be solved by the singular value decomposition (SVD) method [5]. In this method, the impedance matrix H is expanded as $H \approx \hat{U}\Sigma\hat{V}^*$ in which matrix $\hat{U}$ contains the left singular vector $\hat{u}_i$, the matrix $\hat{V}$ contains the right singular vector $\hat{v}_i$ and the diagonal matrix Σ contains the singular values σ_i of the impedance matrix H. With this decomposition, the solution of (4) can be considered as follows [16]:

$$I_M = H^\dagger \times E.$$
$$I_M = \left(\sum_{i=1}^{n} \frac{\hat{u}_i^* E}{\sigma_i} \hat{v}_i \right), \quad (5)$$

where $H^\dagger$ is called the pseudo inverse of matrix H. It should be mentioned that in the applications where a large amount of data is involved in the system of Equations (4), iterative solvers like conjugate gradient (CG), least square QR (LSQR) and etc. is preferred [8].

Once the equivalent magnetic currents are obtained, the final step is to use these currents in the forward radiation problem and find the radiation fields at any desired distance.

B. The regularized SRM

As is shown in the previous section, SRM is an inverse source problem in which the equivalent currents are determined from the known electric field data. Like all other inverse problems, SRM is inherently an ill-posed problem, which means that a solution is very sensitive to small errors and noise.

In order to minimize the effect of measurement errors and noise, a regularized SRM can be applied in which the currents are reconstructed by the Tikhonov Regularization Technique (TRT). It is already shown that the TRT results are more stable in the presence of any type of noise signals [6]. In the TRT, the minimization Equation (4) is replaced by the following equation [6]:

$$I_{reg} = \arg\min_{\mathrm{I}_M} \left\{ \left\| E_{noisy} - H \times I_M \right\|_2^2 + \Gamma^2 \left\| I_M \right\|_2^2 \right\}, \quad (6)$$

in which E_{noisy} is the measured electric field in the presence of noise and Γ is a regularization parameter. Similar to (5), the solution of Equation (6) can be written as follows [16]:

$$I_{reg} = H^\# \times E_{noisy}.$$
$$I_{reg} = \sum_{i=1}^{n} \left(\frac{\sigma_i \hat{u}_i^* E_{noisy}}{\sigma_i^2 + \Gamma^2} \right) \hat{v}_i, \quad (7)$$

where $H^\#$ is the pseudo inverse of the regularized Equation (6).

From Equation (7), it is obvious that by adding a regularization parameter to the singular values of H, the effect of perturbation error and noise is reduced. Therefore, the regularized solutions are more stable in the presence of noise. It is also can be understood that if the measurement is noiseless no regularization is needed $(H^\dagger = H^\#)$.

As described before, in this paper we want to investigate the effectiveness of noiseless SRM in the RNF/FF transformation. To evaluate the SRM accuracy, a RNF/FF error can be defined as follows [11]:

$$\varepsilon_{FF} = \frac{\left\| E_{FF} - E_{SRM-FF} \right\|_2^2}{\left\| E_{FF} \right\|_2^2}, \quad (8)$$

in which E_{FF} is the reference FF data of the AUT and E_{SRM-FF} is the obtained FF radiation by the SRM equations. The numerator of this equation can be expanded based on the known reactive near field data E_{RN} as follows:

$$Num(\varepsilon_{FF}) = \left\| E_{FF} - H' \times M_{eq} \right\|_2^2 = \left\| E_{FF} - H' \times (H^\dagger \times E_{RNF}) \right\|_2^2, \quad (9)$$

in which H' is the impedance matrix of the forward problem which transform the equivalent currents to the FF radiation fields.

As is known in the RNF region, the electric field E_{RN} is composed of evanescent and non-evanescent modes and can be written as follows:

$$E_{RNF} = E_{Non-Ev.} + E_{Ev.}. \quad (10)$$

If this equation is used in the FF transformation error of Equation (9) and the $H^\dagger$ matrix is replaced by its SVD, the following equation is obtained:

$$Num(\varepsilon_{FF}) = \left\| E_{FF} - H' \times \sum_{i=1}^{n} \left(\frac{u_i^* E_{\mathrm{Ev.}}}{\sigma_i} \right) v_i - H' \times \sum_{i=1}^{n} \left(\frac{u_i^* E_{\mathrm{Non\text{-}Ev.}}}{\sigma_i} \right) v_i \right\|_2^2. \quad (11)$$

In this equation the forward radiation matrix H' is ideally try to filter all of the evanescent terms of electric field and amplify the non-evanescent terms in order to create the stable far field radiation. However if the singular values of $H^\dagger(\sigma_i)$ are not treated well, mathematically they can magnify the non-desirable evanescent modes in Equation (11) and makes the far field radiation unstable. This important point is neglected

in the SRM papers until now [3]-[12]. This instability in the far field transformation error in Equation (11) can be resolved by replacing $H^{\dagger}$ with $H^{\#}$ as follows:

$$Num(\varepsilon_{FF}) = \left\| E_{FF} - H' \times H^{\#} \times E_{Ev.} - H' \times H^{\#} \times E_{Non-Ev.} \right\|_2^2,$$

$$= \left\| E_{FF} - H' \times \sum_{i=1}^{n} \left(\frac{\sigma_i u_i^* E_{\mathrm{Ev.}}}{\sigma_i^2 + \Gamma^2} \right) v_i - H' \times \sum_{i=1}^{n} \left(\frac{\sigma_i u_i^* E_{Non-\mathrm{Ev.}}}{\sigma_i^2 + \Gamma^2} \right) v_i \right\|_2^2 . \quad (12)$$

It should be emphasized that in the above equations it is assumed that all the measurements are noiseless, however, because of a large amount of evanescent modes, only a regularized SRM have a stable behavior in the RNF/FF transformation. In (12) the term $H' \times H^{\#} \times E_{Ev.}$ can be defined as a regularized perturbation error in the noiseless RNF/FF transformation.

C. Determination of the regularization parameter

Once the necessity of regularization in the RNF/FF transformation is shown, the next step is to introduce a method for determining the regularization parameter, Γ, in the Equation (6). In the open literature, there are different methods for computing a good regularization parameter, such as the discrepancy principle, the L-curve, and generalized cross validation (GCV) [17].

In this paper, the L-curve method is used for finding a regularization parameter because this method is more visual and can be understood more physically. In the L-curve method for different regularization parameters, the norm of $\|I_{reg}\|_2$ versus the residual norm of $\|E - H \times I_{reg}\|_2$ is plotted in a log-log scale as shown in Fig. 3. This plot has always a characteristic of L-shaped appearance and the regularization parameter is determined at the L-curve corner which is corresponds to the minimum of both quantities [17].

III. RESULTS AND DISCUSSION

A. Horn antenna effect of near field distance

In order to evaluate the accuracy of the proposed regularized SRM, first, a horn antenna as shown in Fig. 1, is simulated in a well-known FEM solver HFSS. This horn antenna that is simulated at 2.4 GHz, has a largest dimension of *D=24cm*. Therefore, the RNF region of this antenna extends up to *1.6λ* from the antenna aperture. The RNF data of this antenna is obtained in a hemisphere with $0° < \theta < 90°$, $0° < \varphi < 360°$ and angular resolution of $\Delta\theta = 1°$ and $\Delta\varphi = 6°$. The magnetic currents are reconstructed in a rectangular aperture of *40 cm×40 cm* with 800 triangular facets and 1160 edges. Therefore, the SRM matrix equation should be solved with 11102 known near field data and 1160 unknown magnetic current coefficients.

For the initial investigation, reactive near field data on a hemisphere with *λ/2* radius from the antenna aperture is used as the input of the proposed regularized SRM. The L-curve plot of this data is shown in Fig. 3. As it can be seen from this figure, the value of the regularization parameter should be chosen as *Γ=0.57*.

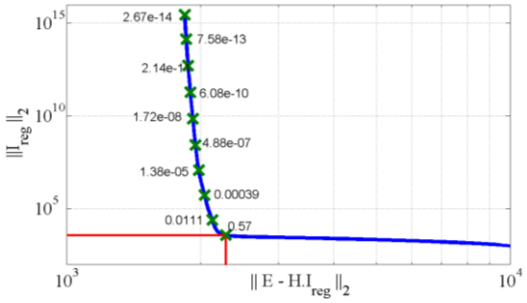

Fig. 3. The L-curve plot of a regularized SRM for λ/2 reactive near field data of the Horn antenna. The L-curve corner is at Γ= 0.57.

In order to solve the Tikhonov Equation (6) with this regularization parameter, LSMR solver is used. LSMR is an iterative solver for the least square problem that recently proposed in [18]. In comparison to other iterative solvers like LSQR and CG, the LSMR has better numerical properties and may be able to terminate sooner [18]. The magnetic current that reconstructed by these settings is shown in Fig. 1 (d).

The reconstructed FF pattern of the regularized solver (LSMR with *Γ=0.57*) and non-regularized solver (LSMR with *Γ=0*) from *λ/2* RNF data are compared with the full wave HFSS simulation in Fig. 4. From this figure, it can be seen that in both E-and H-plane, the regularized algorithm can reconstruct the FF pattern drastically better than the non-regularized solver.

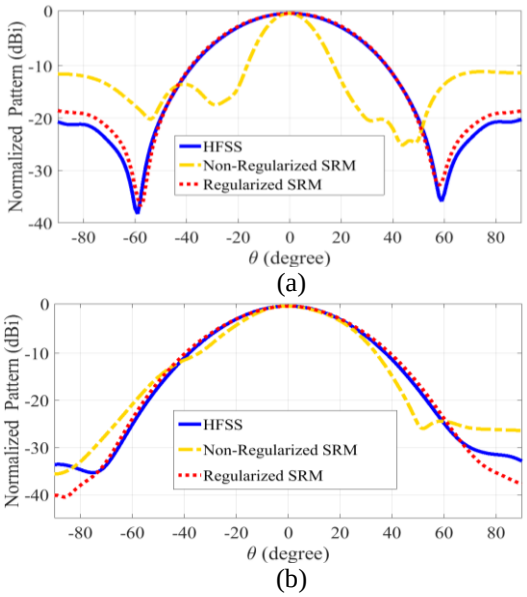

Fig. 4. Comparison of FF pattern of the studied horn antenna in HFSS with the obtained FF pattern of SRM solvers: (a) E-plane and (b) H-plane.

In order to study the necessity of regularization, the FF transformation error (9) of three different near field hemispheres with *λ/2*, *λ*, *3λ/2* radius is evaluated and plotted in Figs. 5 (a), (b) and (c) respectively. The errors are plotted in these figures at each iteration of four different iterative solvers of regularized LSQR, non-regularized LSQR, regularized LSMR and non-regularized LSMR.

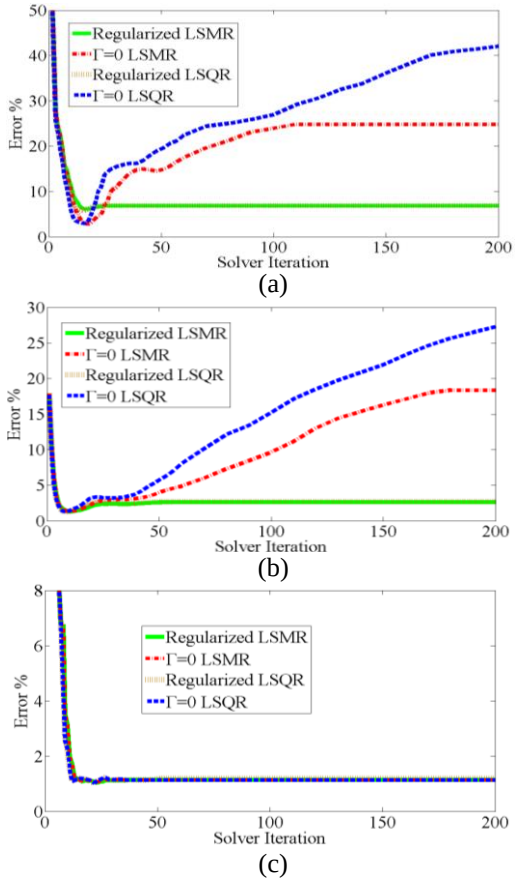

Fig. 5. Comparison of the far field transformation error of regularized and non-regularized solvers in different solver iterations. Input data is a hemisphere with: (a) λ/2, (b) λ, and (c) 3λ/2, radius.

As it can be seen in these figures, while the regularized solvers have a stable response in all three sub figures, the non-regularized solvers show semi-convergence and instability in Figs. 5 (a) and (b). It should be mentioned that the semi-convergence behavior of the iterative solvers in the presence of noise is already discussed in many publications of regularization [19]. The reason for this behavior is that the early iterations of non-regularized solvers reconstruct correct information about the solution while the later iteration amplifies the noise [19].

In our problem, although noiseless simulation data are used in all three figures, but the evanescent modes in the reactive near field region of *λ/2* and *λ*, create such instability in the error plots. As it can be seen in Fig. 5 (c), when these modes are reduced in the *3λ/2* radiative near field region, this instability is also disappeared.

In Fig. 6, the FF transformation error of regularized and non-regularized solvers for near field data of different radii is plotted. As it can be seen in this figure, while in the radiative near field region all methods have almost identical results, in the reactive near field region the non-regularized solvers are oscillating strongly.

Figure 7 shows the value of regularization parameter Γ for the near field data of different radii that calculated by L-curve method. As expected, the value of Γ becomes greater and greater when we approach the antenna aperture, while this value is almost zero in the radiative near field region. In other words, when the evanescent modes are become greater the minimum norm condition ($\|I_{reg}\|_2$) should be stronger in the least square Equation of (6).

From the above results it can be concluded that while the evanescent modes are part of the input data in the RNF region, they can unstable the SRM field transformation just like a noise signal and a regularization is necessary for the RNF/FF transformation applications.

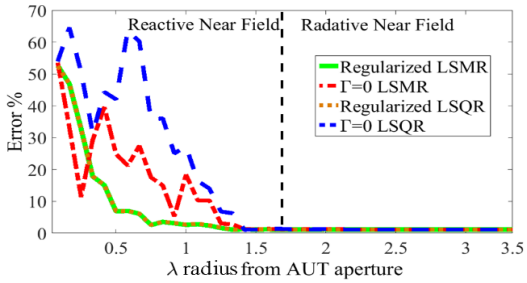

Fig. 6. The far field transformation error of regularized and non-regularized solvers for near field data of different radii.

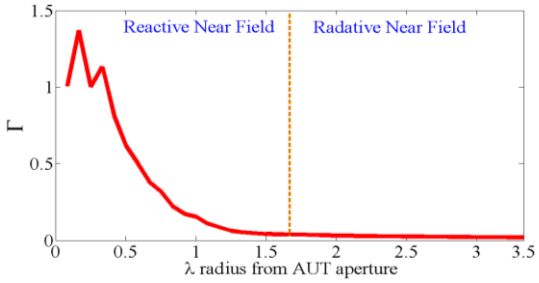

Fig. 7. The value of regularization parameter Γ for the near field data of different radii that calculated by L-curve method.

B. Array antenna effect of SNR

For the second example, consider an array of three

broadband clover leaf dipole antenna as shown in Fig. 8. Clover leaf antennas are originally a broadband cross dipole antennas and are frequently used in base transceiver station (BTS) structures [20]. This antenna is simulated in 1.7 GHz frequency in a well-known FDTD solver CST.

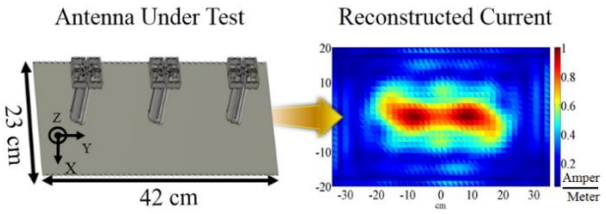

Fig. 8. The configuration of four leaf array antenna and the equivalent magnetic current that reconstructed by the regularized SRM from RNF data of 1.3λ.

The largest dimension of this antenna is equal to 48 cm, therefore, the RNF region of this antenna extends up to 2.8λ from the antenna aperture. The near field data of this antenna is obtained in a hemisphere with $0° < \theta < 90°$, $0° < \varphi < 360°$ and angular resolution of $\Delta\theta = 4°$ and $\Delta\varphi = 3°$. The magnetic currents are reconstructed by SRM in a rectangular aperture of *70 cm ×40 cm* and this aperture is meshed with 2000 triangular facets and 2935 edges. Therefore, the SRM matrix equation should be solved with 5566 known near field data and 2935 unknown magnetic current coefficients.

The reconstructed magnetic current of the regularized LSMR solver from the RNF data of a hemisphere with 1.3λ radius is shown in Fig. 8. The FF pattern that reconstructed by the regularized and non-regularized LSMR are compared with the full wave CST simulation results in Fig. 9. As it can be seen in the both E- and H-planes, the regularized SRM are again reconstructed the FF pattern more accurate than the non-regularized ones. It should be mentioned that a little deviation that can be seen in the calculated pattern of regularized SRM over the horizon angles are mainly due to the truncation error in the reconstructed equivalent current domain as described in [7]. Theoretically, it is assumed that magnetic currents are reconstructed in an infinite surface; however, in the practical computation this surface is truncated at a specified distance. The other important reason is considering only the currents of antenna aperture in SRM calculation while in the full wave simulation scattering from the antenna body is also considered. Therefore calculated pattern with SRM is valid at angles above the horizon [7].

For this example, we try to show the effectiveness of the regularized SRM in the presence of noise. Therefore, a Gaussian noise with different SNR is added to the reactive near field data of CST software. The far field transformation error of non-regularized and regularized LSMR for near field data of different radii in different SNRs is plotted in Figs. 10 (a) and (b), respectively. As it can be seen in this figure, the regularized SRM have more accurate results in all cases especially in the RNF region (less than 2.8λ). It also can be seen that in the radiative near field region the regularization reduce the effect of Gaussian noise when the SNR is not so high.

From these results, it can be understood that in the RNF region due to the presence of a large amount of evanescent modes a regularized SRM should be used instead of the conventional SRM. It is shown that the regularized SRM in RNF/FF application can create more stable and accurate transformation whether RNF data are noiseless or noisy.

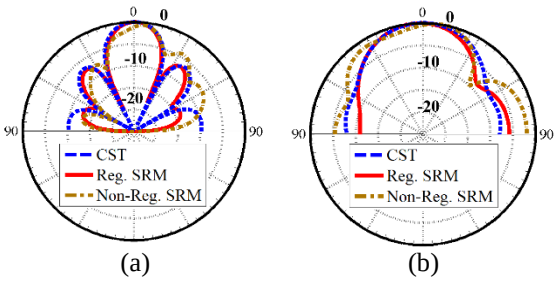

Fig. 9. Comparison of FF pattern of the four leaf antenna in CST with the obtained far field pattern of a regularized and non-regularized SRM from RNF data of 1.3λ: (a) E-plane and (b) H-plane.

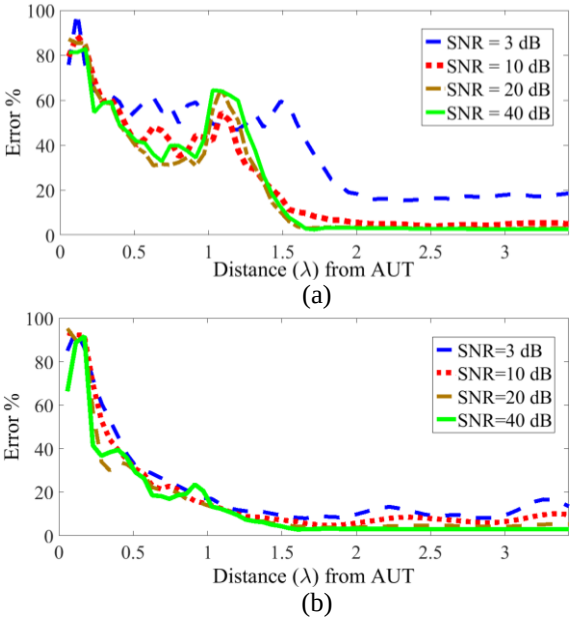

Fig. 10. The far field transformation error of LSMR solver for near field data of different radii in different SNRs: (a) non-regularized LSMR solver, and (b) regularized LSMR solver.

VI. CONCLUSION

In this paper, the RNF/FF transformation based on the SRM technique has been studied carefully. It has been shown that in the RNF region whether the input data is noisy or noiseless, the evanescent modes can unstable the SRM iterative solvers. It has been shown analytically that the RNF instability can be resolved by using a Tikhonov SRM equation. The regularization parameter of the Tikhonov equation has been determined by the well-known L-curve method. In order to evaluate the accuracy of the proposed regularized SRM two different antenna with different conditions has been simulated. Far field transformation error of theses antennas has been evaluated by both regularized and non-regularized solvers. It has been shown that in the RNF region the non-regularized SRM is unstable and failed to reconstruct the correct pattern, while the regularized SRM is maintained stable and can create better transformation both in the presence and non-presence of Gaussian noise. According to the results of this paper, a regularized SRM should be used instead of conventional SRM for the RNF/FF applications.

REFERENCES

[1] A. Yaghjian, "An overview of near-field antenna measurements," *IEEE Trans. Antennas Propag.*, vol. 34, pp. 30-45, Jan. 1986.

[2] L. Zhiping, Z. Wang, and W. Jianhua, "Computer reconstructed holographic technique for phase-less near-field measurement," *ACES Journal*, vol. 28, no. 12, pp. 1199-1204, Dec. 2013.

[3] Y. Alvarez, F. Las-Heras, and M. R. Pino, "On the comparison between the spherical wave expansion and the sources reconstruction method," *IEEE Trans. Antennas Propag.*, vol. 56, no. 10, pp. 3337-3341, Oct. 2008.

[4] A. Taaghol and T. K. Sarkar, "Near-field to near/ far-field transformation for arbitrary near-field geometry, utilizing an equivalent magnetic current," *IEEE Trans. on Elec. Comp.*, vol. 38, no. 3, pp. 536-542, Aug. 1996.

[5] T. K. Sarkar and A. Taaghol, "Near-field to near/ far-field transformation for arbitrary near-field geometry utilizing an equivalent electric current and MoM," *IEEE Trans. Antennas Propag.*, vol. 47, no. 3, pp. 566-573, Mar. 1999.

[6] J. Colinas, Y. Goussard, and J. J. Laurin, "Application of the Tikhonov regularization technique to the equivalent magnetic currents near-field technique," *IEEE Trans. Antennas Propag*., vol. 52, no. 11, pp. 3122-3132, Nov. 2004.

[7] F. Las-Heras, M. R. Pino, S. Loredo, Y. Alvarez, and T. K. Sarkar, "Evaluating near-field radiation patterns of commercial antennas," *IEEE Trans. Antennas Propag.*, vol. 54, no. 8, pp. 2198-2207, Aug. 2006.

[8] Y. Alvarez, F. Las-Heras, and M. R. Pino, "Reconstruction of equivalent currents distribution over arbitrary three-dimensional surfaces based on integral equation algorithms," *IEEE Trans. Antennas Propag.*, vol. 55, no. 12, pp. 3460-3468, Dec. 2007.

[9] Y. Alvarez Lopez, F. Las-Heras Andres, M. R. Pino, and T. K. Sarkar, "An improved super-resolution source reconstruction method," *IEEE Trans. Instrum Meas.*, vol. 58, no. 11, pp. 3855-3866, Nov. 2009.

[10] C. H. Schmidt and T. F. Eibert, "Integral equation methods for near-field far-field transformation," *ACES Journal*, vol. 25, no. 1, pp. 15-22, Jan. 2010.

[11] J. L. Araque Quijano and G. Vecchi, "Improved-accuracy source reconstruction on arbitrary 3-D surfaces," *IEEE Antennas Wireless Propag. Lett.*, vol. 8, pp. 1046-1049, 2009.

[12] J. L. Araque Quijano and G. Vecchi, "Near- and very near-field accuracy in 3-D source reconstruction," in *IEEE Antennas Wireless Propag. Lett*, vol. 9, pp. 634-637, 2010.

[13] P. Vinetti, *A Non-Invasive, Near-Field and Very Near-Field Phaseless Antenna Characterization System*, Ph.D. dissertation, Universita di Napoli Federico II, Nov. 2008. (Available at http://www.fedoatd.unina.it/1343/2/Tesi_Dottorato_PV_v2.pdf)

[14] A. Capozzoli, et al., "Dielectric field probes for very-near-field and compact-near-field antenna characterization [measurements corner]," *IEEE Antennas Propag. Mag.*, vol. 51, no. 5, pp. 118-125, Oct. 2009.

[15] D. J. Lee, J. Y. Kwon, N. W. Kang, J. G. Lee, and J. F. Whitaker, "Vector-stabilized reactive-near-field imaging system," *IEEE Trans. Instrum. Meas.*, vol. 60, no. 7, pp. 2702-2708, July 2011.

[16] M. E. Kilmer and D. P. O'Leary, "Choosing regularization parameters in iterative methods for ill-posed problems," *SIAM J. Matrix Anal. Applicat*., vol. 22, no. 4, pp. 1204-1221, 2001.

[17] P. C. Hansen, "Rank-deficient and discrete ill-posed problems: Numerical aspects of linear inversion," *SIAM*, vol. 4, 1998.

[18] D. C.-L. Fong and M. A. Saunders, "LSMR: An iterative algorithm for sparse least-squares problems," *SIAM J. Sci. Comput.*, vol. 33, no. 5, pp. 2950-2971, Oct. 2011.

[19] J. Chung, J. G. Nagy, and D. P. O'Leary, "A weighted GCV method for Lanczos hybrid regularization," *Electron. Trans. Numerical Anal*., vol. 28, pp. 149-167, Jan. 2008.

[20] G. M. Lytle, J. L. Schadler, and D. Kokotoff, "*Broadband Clover Leaf Dipole Panel Antenna*," U.S. Patent 8 558 747, Oct. 15, 2013.

Electromagnetic Radiation Source Identification Based on Spatial Characteristics by Using Support Vector Machines

Dan Shi and Yougang Gao

Department of Electronic Engineering
Beijing University of Posts and Telecommunications, Beijing, 100000, China
shidan@buptemc.com

Abstract ─ In the radio monitoring, electromagnetic interference diagnostics and radar detection, the electromagnetic radiation source identification (ERSI) is a key technology. A new method for ERSI was proposed. The support vector machines (SVMs) have been applied to facilitate the ERSI on the basis of the spatial characteristics of the electromagnetic radiation sources. The radiation sources were located by the triangulation method, and then their spatial characteristics were collected by a band receiver array, and converted from 3D data to 1D vector with subscripts as the inputs for the SVMs. We trained the model with these 1D vectors to enable it to identify the radiation source types with both high speed and accuracy. The identification time needs only a few seconds, which is much faster than the artificial neural networks (ANNs). The influence of parameters (e.g., noise from the ambient environment, the data collection method, the scaling method for the input data, and the penalty parameter) were discussed. The proposed method has good performance even in the noisy environments. The results were verified by a designed measurement. The proposed approach is very useful for the ERSI of unknown radiation sources in practice.

Index Terms ─ Band receiver array, electromagnetic radiation source identification, spatial characteristics, support vector machines.

I. INTRODUCTION

Electromagnetic radiation source identification has been a topic of intense researches due to its applications in the radio monitoring and electromagnetic interference diagnostics as well as radar sensor [1-10]. Nowadays, the EMC diagnosis is mainly confronting with a challenge, that is, the identification and localization of different interference sources. The traditional EMC diagnosis widely relies on the experience of engineers and the exact knowledge of the electronic system, and there is no unitized methodology can be referred to. [1] proposed an electromagnetic radiation source identification method based on the independent component analysis (ICA) theory. By using a kurtosis-based ICA algorithm, the radiated emission feature of different sources is extracted from some spectrum data measured at different positions. This method requires that the sources are independent signals, whose features are different frequencies. If the frequencies overlap, the method may be unavailable. Moreover, the accuracy is affected by the noise in the environment significantly. [2-8] investigated the possibility of detecting and identifying the electronic devices based on their electromagnetic emissions. Short-term FFT combined with a cross correlation technique was applied to identify different devices [2]. The signal was separated from the noise on the basis of different frequency, and then the envelope of the signal was recovered. The devices were identified by their envelopes with a cross correlation or a neural network. Thus, the different frequencies and envelopes are necessary for this method. [3] presented a method for detecting and identifying the vehicles based on their RF emissions. The parameters like the average magnitude or the standard deviation of the magnitude within a frequency band were extracted from the measured emission data. These parameters were used as the inputs to the artificial neural networks (ANNs) that were trained to identify the vehicle that produced the emissions. When a spark event was not captured, however, the neural network was unable to successfully identify the responsible vehicle. Thus, a high signal to noise ratio is needed. In the radar detection, many published literatures are focus on the emitter identification (EID). The conventional identification approaches, which separate the received pulses into individual emitter groups, are usually based on the basic pulse parameters, such as the direction of arrival (DOA), radio frequency, time-of-arrival, pulse width and pulse repetition interval; these approaches are not applicable when the EM source frequencies overlap and are sensitive to noise [9-18]. In the radio monitoring, the distinction between the radiation sources mainly depends on the frequency separation by using a spectrum analyzer [19-20].

Our group has been working on the radiation source identification when the frequencies of sources overlap in

Submitted On: September 2, 2016
Accepted On: December 24, 2016

the noisy environment [21-22]. Firstly, we proposed to identify the radiation sources based on their spatial characteristics by using the artificial neural networks [21]. The method is very accurate without any additive noise. However, the accuracy is affected by the noise significantly. Thus, an improved method was brought forward [22]. The radiation source type was recognized by the support vector machines (SVMs), which can withstand some strong noise. Nevertheless, the above two methods have same limitation for they use the same receiver array, which is located in a 3D cube. This requires that the test data must be collected in the same way as the training data collected. It means all data are collected in the enlarged or shrunken cubes in the main lobe of the radiation sources, and only small bias is allowed.

In this paper, to make the method more applicable, the receiver array is improved by using a band shape instead of a 3D cube. The band receiver array is more consistent with the pattern recognition theory. It relaxes the requirement that the test data should be exactly collected in the same way as the training data collected, where all the data are collected in a narrow cone around the main lobe of the radiation sources. In our model, the ERSI problem is considered as a nonlinear mapping problem, the mapping from the space of the feature vectors of the radiation source to the space of the source type. The effectiveness of the method is demonstrated as a multi-ERSI problem with and without the additive noise. With this method, taking the spatial characteristics as the feature vectors is enough to obtain the high accuracy for the identification, which is much simpler than the multi-features for the identification in [9].

II. SVMs FOR CLASSFICATION

The data used for the SVM classification is often a pair comprising an input object (typically a vector, called attribute or feature) and a desired output value (called label). A supervised learning algorithm analyzes the training data and produces inferred functions, which are called "classifiers". The inferred function should predict the correct output value for any valid input object. This approach requires the learning algorithm to generalize unseen situations in a "reasonable" way.

In classification, however, it often happens that the data sets to discriminate are not linearly separable in a finite dimensional space. For this reason, it is proposed that the original finite-dimensional space is mapped into a much higher-dimensional space, presumably making the separation easier in that space. In our model, the data sets composed by the electric field strengths at 27 points are difficult separated in the finite dimensional space, so they should be mapped into a higher-dimensional space by using a kernel function $K(\boldsymbol{x}_i, \boldsymbol{x}_j)$ [23-24]. The radial basis function (RBF), a kind of the kernel functions, is suitable for the case that the class labels and attributes is nonlinear. In our model, the attributes are the electric field strengths at 27 points, and the labels are the types of the radiation sources, so the RBF is chosen for this nonlinear issue;

$$K(\boldsymbol{x}_i, \boldsymbol{x}_j) = \exp(-\gamma \| \boldsymbol{x}_i - \boldsymbol{x}_j \|^2), \ \gamma > 0 . \quad (1)$$

After the data are mapped to a higher-dimensional space with the RBF, the soft margin method will choose a hyper-plane that splits the examples as cleanly as possible, while still maximizing the distance to the nearest cleanly split examples [25]. The method introduces the non-negative slack variables ξ_i to mark a degree of the classification error of sample xi. Given a training set of attribute-label pairs $(\boldsymbol{x}_i, \boldsymbol{y}_i)$, $i = 1, \cdots, m$, where $\boldsymbol{x}_i \in \mathrm{R}n$ and $\boldsymbol{y}_i \in \{-1,1\}^m$, the SVMs require the solution of the following optimization problem:

$$\min_{\boldsymbol{w},b,\xi} \left\{ \frac{1}{2} \boldsymbol{w}^T \boldsymbol{w} + C \sum_{i=1}^{m} \xi_i \right\}$$

$$\text{subject to } \begin{matrix} \boldsymbol{y}_i (\boldsymbol{w}^T \phi(\boldsymbol{x}_i) + b) \geqslant 1 - \xi_i \\ \xi_i \geqslant 0 \end{matrix} . \quad (2)$$

Here, the training vectors $\boldsymbol{x}_i$ are nonlinearly mapped into a higher dimensional space by the function ϕ. The RBF has the relationship with function ϕ, that is, $K(\boldsymbol{x}_i, \boldsymbol{x}_j) = \phi(\boldsymbol{x}_i)^T \phi(\boldsymbol{x}_j)$. $\boldsymbol{w}$ is the normal vector to the hyper-planes. We should minimize $\|\boldsymbol{w}\|$ to find the maximum distance between these hyper-planes. C>0 is the penalty parameter of the error term, and the compromise between the maximal margin and the classification error can be achieved by adjusting C. Eq. (2) tries to increase the margin and decrease the error introduced by ξ_i.

The steps using the SVMs for the classification in this paper are listed below:

1) Collect data sets comprising attributes (electric field strengths at 27 points) and labels (types of the radiation sources), and randomly divide them into the training sets and test sets.
2) Scale the attributes.
   The scaling of attributes is to avoid the attributes in greater numeric ranges to dominate those in smaller numeric ranges, and can accelerate the convergence of the SVMs. Since the kernel values usually depend on the inner products of the feature vectors, large attribute values may also lead to numerical problems. As a result, each attribute is scaled to the range [0, 1] in our model. An arc tangent, logarithm scaling and linear scaling are applied, and the results are compared in Section IV.
3) Choose the RBF kernel function.
   The RBF usually works well in the situation that the

number of feature is small, but the size of the training set is intermediate. For the model introduced in the paper, which contains 27 feature points and 9,000 rows in the training set, the RBF kernel can help provide enough variance to fit the training data within the constraints.

4) Perform cross-validation to find the best parameters C and γ. The influence on identification accuracy from different C and γ is investigated in Section IV. The optimized C and γ are found by the genetic algorithm (GA), which are 2 and 1 respectively in our model.
5) Utilize the best parameters C and γ to train the data sets and then find an appropriate inferred function.
6) Test and predict the accuracy with the test data sets, and then check the validity of the method.

III. MODEL AND CALCULATION

For the intentional electromagnetic radiation, it is often generated from the radiator, namely antenna. For instance, the radiation from a mobile phone usually comes from the phone antenna, such as the planar inverse-F antenna (PIFA), the radiation from a base station is often generated by a planar antenna, and the radars transmit the electromagnetic wave through the phased array antennas, etc. On the other hand, for the unintentional radiation, it is often caused by the equivalent antennas. For example, a bare wire in an electronic device often causes the electromagnetic interference (EMI), which is usually modeled with a dipole antenna. The radiation caused by a printed circuit board trace is often modeled with a loop antenna. In a word, the devices causing the radiation interference can be modeled with their primary radiated antennas. Obviously, the spatial characteristics of different antennas are different, which are unique features used for identification of the antennas, thereby achieving the ERSI.

In [21] and [22], the spatial characteristics of the radiation sources are collected by a 3D cube. The dimensions of this cube are 50 mm x 50 mm x 50 mm. The 27 receivers distributed in a cube are located at the center of edges, faces and volume. Two neighboring receivers are set 25 mm away from each other. The cube moves with a 20 mm steps in the x, y and z directions in a cone around the main lobe to collect the data sets. In those models, the way collecting the data sets for the recognition should be similar with the way collecting data sets for the training. That is, the 27 receivers collect the data sets in the enlarged or shrunken cubes in a narrow cone around the main lobe of the radiation sources. In other words, the high identification accuracy is achieved under these conditions:

(1) The test data sets are collected at the same plane as the training data sets, shown in Fig. 1.
(2) For an alternative method, if the test data sets are collected at different plane from the training data sets, the distance between the neighboring receivers should vary with the distance from the radiation source to the receiver cube, and the formula is presented in [21];

$$L = H/50\sqrt{6}\,, \tag{3}$$

where L is the distance between the neighboring receivers, H is the distance from the radiation source to the receiver cube.

We have tested the ability of the method proposed in [21] to withstand the deviation between the test data sets and the training data sets. It is found that the identification accuracy decreases significantly with the deviation, as shown in Table 1.

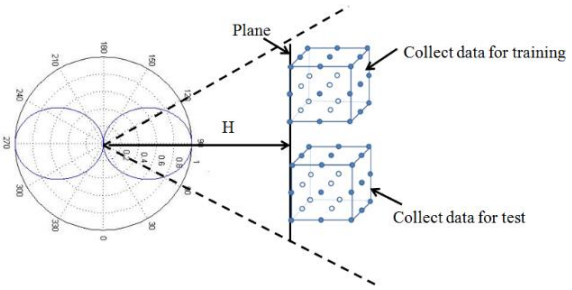

Fig. 1. Data collection for a dipole antenna.

Table 1: Identification accuracy vs. deviation

Training Data Location / Test Data Location	5 m	10 m
1.5 m	13.59%	19.03%
3 m	50.46%	29.37%
5 m	89.86%	46.2%
6 m	78.6%	55.12%
10 m	63.7%	91.49%
15 m	54.94%	71.25%
20 m	51.93%	60.08%

Table 1 shows that the location deviation between the training data sets and the test data sets gives rise to an accuracy degeneration.

To solve the problem, hence, this paper brings up a new receiver array. In practice, before the data are collected by the receiver array, the position of the radiation source should be located. The triangulation method is often used. As Fig. 2 shows, a directional antenna with a narrow range is located at TP1. The DOA (direction of arrival) of the radiation source is determined [26], which is in the line of r1. Similarly, another directional antenna is located at TP2, which determines that the radiation source is in the line of r2. Therefore, the intersection point between r1 and r2 is the location of the radiation source [27].

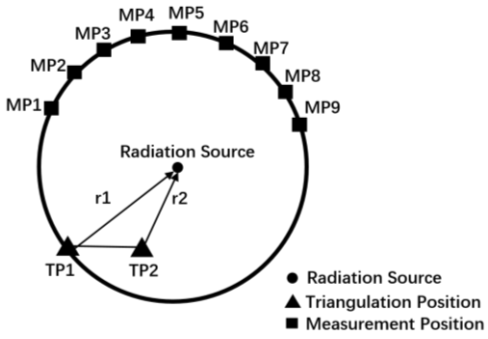

Fig. 2. Triangulation for determining the position of a radiation source.

After the location of the radiation source is determined, the receiver array is moved around the equator of the radiation source to collect the electric field distribution of the source, and then the data are sent to the SVMs for the training and recognition. The steps of the ERSI are shown in Fig. 3.

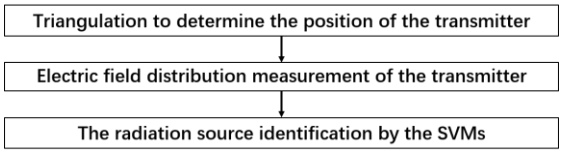

Fig. 3. Steps of ERSI.

The receiver array is composed by 27 elements, which are utilized to collect the spatial characteristics of the radiation source simultaneously. The receivers are located at a band, which is 30° in latitude and 120° in longitude. All the receivers are arranged at 3 rows and 9 columns. The receivers at 9 columns are shown as MP1 to MP9 in Fig. 2. The neighboring receivers are 15° intervals in latitude and 15° intervals in longitude. Then the receiver band moves along the equator of the radiation sources with a 0.1° step. When the band moves 360° along the equator, 3600 data sets are collected, and every data set includes 27 values, which can be expressed as a 1D vector with 27 elements:

$$\boldsymbol{E}_{\mathrm{p}}^{\mathrm{k}} = [\boldsymbol{E}_{11}^{\mathrm{kp}}, \boldsymbol{E}_{12}^{\mathrm{kp}}, \boldsymbol{E}_{13}^{\mathrm{kp}}, \boldsymbol{E}_{14}^{\mathrm{kp}}, \boldsymbol{E}_{\mathrm{mn}}^{\mathrm{kp}} \cdots, \boldsymbol{E}_{39}^{\mathrm{kp}}], \qquad (4)$$

where k is the label of the radiation source type, p is the position label of the band receiver array, m is the row label of the receiver in the band, and n is the column label of the receiver in the band.

Three EM radiation sources, namely, the bare wires, mobile phones, and RFID systems, are modelled with their primary radiators, that is, a dipole antenna, a planar inverse-F antenna (PIFA), and a microstrip antenna, respectively. These three antennas are all working at 3 GHz to ensure that the SVMs identify the radiation sources on the basis of the spatial characteristics other than the frequency. The electric field distributions around these sources, called "spatial characteristics", are collected by the simulation with the HFSS software, a commercial software based on the finite element method [28]. The band receiver arrays vs. the antenna patterns are displayed from Fig. 4 to Fig. 6.

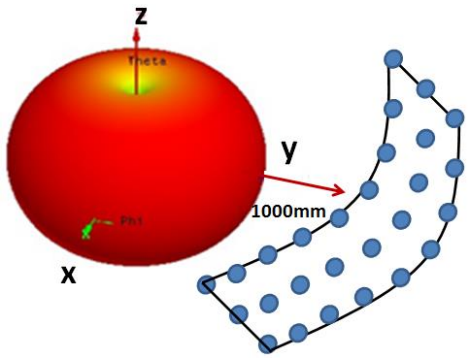

Fig. 4. Receivers vs. pattern of a dipole antenna.

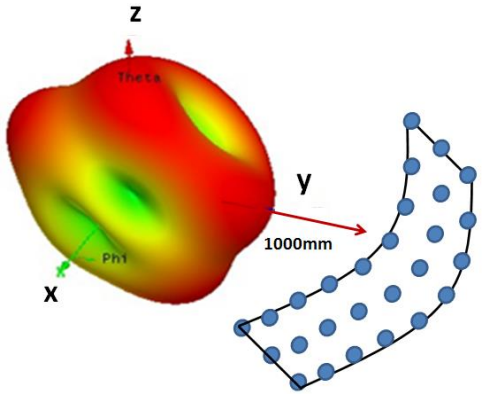

Fig. 5. Receivers vs. pattern of a PIFA antenna.

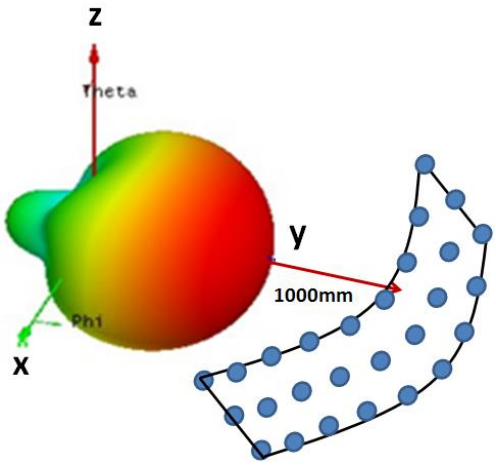

Fig. 6. Receivers vs. pattern of a microstrip antenna.

Obviously, the spatial characteristics of these three antennas are different as shown in Figs. 4-6. They are

collected by a band receiver array, which is a circular and part of a big ring around the radiation source, and are used as the unique features for the SVMs to identify. The spatial information is converted from 3D array to 1D vector with subscripts as inputs to simplify the model. Since there are 3600 data sets, that is, 3600 1D vectors for each antenna, 10800 data sets for these three antennas are obtained. These data sets are expressed as a combined vector set $\boldsymbol{E}_{total} = [\boldsymbol{E}_1^1, \boldsymbol{E}_2^1, \cdots, \boldsymbol{E}_{3600}^3]'$, where the superscript in the vector set represents the type of the radiation source, and the subscript in the vector set represents the position of the band receiver array. The vector set $\boldsymbol{E}_{total}$ is scaled to the range [0, 1] with a linear scaling and marked with the source type. For instance, the data sets belonging to the dipole antenna are marked with "1" at the end of the data sets, the data sets belonging to the PIFA antenna are marked with "2", and the third one is marked with "3". The vector set $\boldsymbol{E}_{total}$ includes 10800 vectors, which are randomly divided into two categories for the training and the test. In the training process, the RBF kernel function is utilized to extract the relationship between the spatial characteristics and the source types, and constructs a hyper-plane classifying the sources based on the vectors. Since the distinction among the spatial characteristics of the radiation sources is apparent, the hyper-plane is easy to construct. The RBF kernel function has two important parameters, called "kernel parameter γ and penalty parameter C". The GA is applied to find the best parameters C and γ by an iteration searching, which are 2 and 1 in this model respectively. After trained with 9000 data sets within a few minutes, the SVMs can identify these EM source types by their spatial characteristics rapidly and accurately. The 1800 data sets left are applied for the test. When the vectors are input into the SVMs, the SVMs can identify the source types these vectors belong to, and the identification accuracy is up to 100%. The $F1$ measure is used for checking the validity of our model. $F1$ combines the recall (r) and the precision (p) with an equal weight in the following form:

$$F1 = \frac{2rp}{r+p}, \tag{5}$$

where p is the number of the correct results divided by the number of all returned results, and r is the number of the correct results divided by the number of results that should have been returned. The $F1$ in this model is 1, which reflects the validity of our method.

IV. DISCUSSION

A. The influence from the noise

In this section, the influence from ambient noise is investigated. The Gaussian noise is added in our model. The parameter of signal-to-noise ratio (SNR) is applied, which is expressed as follows:

$$\text{SNR (dB)} = 10 \times \log_{10} \frac{P_{\text{avg}}}{P_{\text{noise}}}, \tag{6}$$

where P_{avg} is the average power of the input data, and P_{noise} is the power of the Gaussian noise.

The identification accuracy versus SNR is listed in the Table 2. It also gives the comparison between the SVMs and the ANNs. The ANNs are classic back-propagation (BP) neural networks which include one input layer, one hidden layers, and one output layer. There are 30 neurons in the hidden layer. The levenberg-marquardt algorithm is applied in the training. When the mean square error (MSE) falls below 0.01 or the epochs exceed 30000, the training stops. The data for the training and the test are same with those for the SVMs, and a linear scaling is used. From Table 2 it is found that if no noise is added, the identification accuracy with the SVMs and the ANNs is both very high. However, the SVMs are not closely related to the noise. When the SNR decreases from 20 dB to 15 dB, the accuracy varies from 99.94% to 97.12%. Even in a strong noise environment, where the SNR is only 10 dB, the accuracy with the SVMs is still 76.57%. Thus, the method using the SVMs to identify the radiation sources can be applied in the noisy environments. Whereas the accuracy with the ANNs significantly decreases as the noise increases. When the SNR is 15 dB, the accuracy rate with the ANNs degrades to 64.1%, and it cannot work when the SNR is 10 dB.

Table 2: Identification accuracy vs. SNR

SNR/dB	No Noise	25	20	15	10
Accuracy of SVMs/%	100	100	99.94	97.12	76.57
Accuracy of ANN/%	99.98	98.43	82.3	64.1	38.87

B. The influence from the data collection

The spatial characteristics are represented by the data sets. Thus, the method of the data collection is important to the identification accuracy. In [22], we proposed to collect the data sets by using a 3D cube with 27 receivers. The 3D cube moves along a cone, whose angle is 60°. So the data sets mainly represent the spatial characteristics of the main lobe of the antennas. As an improved method, the data sets are collected with a band receiver array, and the band moves around the equator of antennas. According to the pattern recognition theory, it is preferable to identify the radiation sources with the global information other than the local information, which has been proven by the result comparison between this method and that proposed in [22].

Some other test results also support this point. Firstly, we use a band receiver array with 9 receivers to collect the data sets. The neighboring receivers are 1° intervals in longitude. The identification accuracy is not good, and the best accuracy is only 71.2%. So we

suppose that the receiver number is not enough to collect the spatial characteristics. Then the receiver number is increased to 30, and the neighboring receivers are also 1° intervals in longitude. Unfortunately, the identification accuracy is still not satisfactory. Thus, we increase the intervals between the neighboring receivers to 15° in longitudes and 27 receivers are applied, and good results are obtained finally. The reason lies in the fact that the pattern recognition has better performance when the object is recognized as a whole. The results using a receiver array with different intervals are compared in Fig. 7.

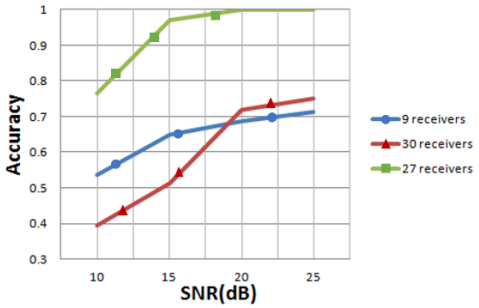

Fig. 7. Accuracy of three data collection methods.

From Fig.7 it can be found that the method using 27 receivers with 15° intervals is the most accurate one among these three methods.

C. The influence from the scaling method

Different scaling methods give different identification accuracy. In this section, three typical scaling methods, namely the tangent scaling, logarithm scaling and linear scaling, are utilized to investigate the influence from the scaling method on the accuracy.

As mentioned in Section III, a total of 10800 input vectors are expressed as a combined vector set $\boldsymbol{E}_{total} = [\boldsymbol{E}_1^1, \boldsymbol{E}_2^1, \cdots, \boldsymbol{E}_{3600}^3]'$. The elements in $\boldsymbol{E}_{total}$ are scaled by three different methods.

The following formula is applied for the arc tangent scaling:

$$\boldsymbol{E}_s = a\tan(\boldsymbol{E}_{total}) \times 2/\pi , \tag{7}$$

where $\boldsymbol{E}_s$ is the input vector sets after the scaling.

Eq. (8) is used for the logarithm scaling:

$$\boldsymbol{E}_s = \log_{10}(\boldsymbol{E}_{total}) . \tag{8}$$

Eq. (9) is applied for the linear scaling:

$$\boldsymbol{y}_i = \frac{\boldsymbol{x}_i - x_{\min}}{x_{\max} - x_{\min}} , \tag{9}$$

where $\boldsymbol{x}_i$ is the element of $\boldsymbol{E}_{total}$; $\boldsymbol{y}_i$ is the element of $\boldsymbol{E}_s$ after the scaling; $x_{\max}$ and $x_{\min}$ are the maximum and minimum elements of $\boldsymbol{E}_{total}$, respectively.

The accuracy versus different scaling methods is shown in Table 3.

Table 3: Accuracy vs. scaling method

SNR/dB	25	20	15	10
Accuracy with arc tangent scaling/%	95.09	93.66	84.16	67.21
Accuracy with logarithm scaling/%	100	99.47	92.4	68.67
Accuracy with linear scaling/%	100	99.94	97.12	76.57

Obviously, the linear scaling method has the best performance among these three scaling methods. The reason lies in the fact that the linear scaling works better when the data value exceeds 3 while the arc tangent scaling is more suitable for the data value in range (0-3), and most of the data used in our model are above 4.

D. The influence from the parameters of the SVMs

For the support vector machines, there are two key parameters, namely the penalty parameter C and γ of the kernel function. The penalty parameter C reflects the impact from the outlier case, and adjusting it can achieve the compromise between the maximal margin and the classification error. According to Eq. (2), the loss of the object function increases with C when $\sum_{i=1}^{m} \xi_i$ is fixed. When C is infinite, the problem would be insoluble once the outlier case exists. Therefore, smaller C is preferable when the same identification rate is achieved since it can improve the generalization ability of the SVMs. However, if C is too small, the penalty to the outlier case is small and the error is large, leading to an identification accuracy degradation. For γ of the kernel function, it represents the correlation between those support vectors. If γ is too small, there is no significant correlation between the support vectors, and the learning process is complex. On the other hand, if γ is too large, the mutual influence between the support vectors is obvious and the precision of the model will be affected. Table 4 presents the identification accuracy versus C and γ . The optimized C and γ are found by the GA, which are 2 and 1 respectively. Obviously, the most accurate result is obtained with these optimized parameters. The accuracy decreases as the values of C and γ deviate from the optimized values. If the C and γ are too small or too large, the accuracy is poor.

Table 4: Accuracy vs. parameters

Parameters	C=0.1, γ=0.1	C=0.2, γ=0.2	C=2, γ=1	C=20, γ=20	C=100, γ=100
Accuracy/%	79.61	94.66	100	89.58	35.62

V. VERIFICATION BY MEASUREMENTS

Some measurements are made to validate the proposed method. The spatial characteristics of the three cell phones with above antennas are collected by a receiving antenna and a spectrum analyzer in an anechoic chamber. The electric field of the points distributed within the sphere that surrounds the source can be obtained by setting the rotation angle of the receiving antenna. A 1° interval is applied for the antenna rotation in the equatorial plane, and 15° intervals are used in the meridian plane. Consequently, the data within the band from −15° to 15° longitude and 1° to 360° latitude around the cell phones are extracted. Then, the electric fields at 27 points are divided into groups using the same method described in Section III. A total of 90 data sets are selected randomly from the three cell phones (i.e., 30 for each cell phone), combined, and scaled. Finally, the scaled data are sent to the proposed model to check the validity of the presented method. The model can correctly identify the data set belonging to which type of the sources. The identification accuracy is 96%, which proves the validity of the proposed method.

VI. CONCLUSION

A new method for the ERSI by using the SVMs is proposed in this paper. The data collection method has been improved. After the position of the radiation source is determined by the triangulation method, a band receiver array is applied for the data collection. The band receiver array moves along the equator of the radiation sources and focuses on collecting the data with global information, which more coincides with the pattern recognition. The results demonstrate that the method proposed in this paper has a better identification accuracy compared with the ANNs and the 3D cube receiver array. It can be applied in a strong noise environment, and the deviation between the training data sets and the test data sets is allowed.

In practice, the method proposed in this paper is also useful for the radiation predication of the sources. The same SVMs model can be applied. After trained by the electric field strengths at several points, the SVMs can predict all the radiations from the sources accurately, which can save a lot of computation time and cost, and this will be investigated in the next step.

ACKNOWLEDGMENT

This work has been supported by National Natural Science Foundation of China, No. 61201024.

REFERENCES

[1] Z. F. Song and D. L. Su, "A novel electromagnetic radiated emission source identification methodology," *Proceeding of 2010 Asia-Pacific International Symposium on* Elec*tromagnetic Compatibility*, pp. 645-648, 2010.

[2] H. Weng, X. Dong, X. Hu, D. G. Beetner, T. Hubing, and D. Wunsch, "Neural network detection and identification of electronic devices based on their unintended emissions," *International Symposium on EMC*, vol. 1, pp. 245-249, 2005.

[3] X. Dong, H. Weng, and D. G. Beetner, "Detection and identification of vehicles based on their unintended electromagnetic emissions," *IEEE Transaction on Electromagnetic Compatibility*, vol. 48, no. 4, pp. 752-759, 2006.

[4] T. Hubing, D. Beetner, X. Dong, H. Weng, M. Noll, B. Moss, and D. Wunsch, "Electromagnetic detection and identification of automobiles," *Proceeding of EuroEM*, Magdeburg Germany, July 2004.

[5] H. Weng, X. Dong, X. Hu, D. Beetner, T. Hubing, and D. Wunsch, "Neural network detection and identification of electronic devices based on their unintended emissions," *in Proc. IEEE Int. Symp. Electromagn. Compat.*, 2005, vol. 1, pp. 245-249, 2005.

[6] C. J. Kaufman, J. Dudczyk, J. Matuszewski, and M. Wnuk, "Applying the radiated emission to the specific emitter identification," *in Proc. 15th Int. Conf. Microwave, Radio Wireless Commun.*, Warsaw, Poland, vol. 2, pp. 431-434, May 17-19, 2004.

[7] M. D'Amore, A. Morriello, and M. S. Sarto, "A neural network approach for identification of EM field sources: Analysis of PCB configurations," *in Proc. IEEE Int. Symp. Electromagn. Compat.*, Denver, CO, vol. 2, pp. 664-669, Aug. 24-28, 1998.

[8] K. Aunchaleevarapan, K. Paithoonwatanakij, Y. Prempreaneerach, W. Khanngern, and S. Nitta, "Classification of PCB configurations from radiated EMI by using neural network," *in Proc. CEEM*, Shanghai, China, pp. 105-110, May 3-7, 2000.

[9] C.-S. Shieh and C.-T. Lin, "A vector neural network for emitter identification," *IEEE Trans. Antennas Propag.*, vol. 50, no. 8, pp. 1120-1127, Aug. 2002.

[10] H. Liu, Z. Liu, and W. Jiang, "Approach based on combination of vector neural networks for emitter identification ," *IET Signal Processing*, vol. 4, no.2, pp. 137-148, 2010.

[11] H. Liu, Z. Liu, and W. Jiang, "Incremental learning approach based on vector neural network for emitter identification," *IET Signal Pro*cessing, vol. 4, no.1, pp. 45-54, 2010.

[12] L. Li, H. B. Ji, and L. Jiang, "Quadratic time-frequency analysis and sequential recognition for specific emitter identification," *IET Signal Processing*, vol. 5, no. 6, pp. 568-574, 2011.

[13] M. Wnuk, A. Kawalec, and J. Dudczyk, "The

method of regression analysis approach to the specific emitter identification," *Proceeding of 16th International Conference on Microwaves, Radar and Wireless Communications*, Krakow, Poland, pp. 491-494, May 22-24, 2006.

[14] X. Chen and W. D. Hu, "Approach based on interval type-2 fuzzy logic system for emitter identification," *Electronics Letters*, vol. 48, no. 18, 2012.

[15] M. Liu and J. F. Doherty, "Nonlinearity estimation for specific emitter identification in multipath channels," *IEEE Transactions on Information Forensics and Security*, vol. 6, no. 3, pp. 1076-1085, 2011.

[16] H. Ye, Z Liu, and W. Jiang, "Comparison of unintentional frequency and phase modulation features for specific emitter identification," *Electronics Letters*, vol. 48, iss. 14, pp. 875-877, 2012.

[17] L. Anjaneyulu, N. S. Murthy, and N. Sarma, "Radar emitter classification using self-organising neural network models," *Proceedings of International Conference on Recent Advances in Microwave Theory and Applications*, Jaipur, Rajasthan, India, pp. 431-433, Nov. 21-24, 2008.

[18] Y. Zhang, H. P. Zhao, and Q. Wan, "Single snapshot 2D-DOA estimation in impulsive noise environment using linear arrays," *ACES Journal*, vol. 27, no. 12, pp. 991-998, 2012.

[19] F. Mavromatis, A. Boursianis, T. Samaras, C. Koukourlis1, and J. N. Sahalos, "A broadband monitoring system for electromagnetic-radiation assessment," *IEEE Antennas and Propagation Magazine*, vol. 51, iss. 1, pp. 71-79, 2009.

[20] C. Camilo Rodríguez, C. Andrés Forero, and H. Ortega Boada, "Electromagnetic field measurement method to generate radiation map," *IEEE Colombian Communications Conference*, pp. 1-7, 2012.

[21] D. Shi and Y. G. Gao, "A new method for identifying electromagnetic radiation sources using backpropagation neural network," *IEEE Transactions on Electromagnetic Compatibility*, vol. 55, iss. 5, pp. 842-848, 2013.

[22] D. Shi and Y. G. Gao, "A method of identifying electromagnetic radiation sources by using support vector machines," *China Communications*, vol. 10, iss. 7, pp. 36-43, 2013.

[23] C. Nello and S.-T. John, *An Introduction To Support Vector Machines And Other Kernel-based Learning Methods*. Cambridge University Press, 2000.

[24] B. Schölkopf, C. J. C. Burges, and A. J. Smola, *Advances In Kernel Methods: Support Vector Learning*. MIT Press, Cambridge, MA, 1999.

[25] C. Cortes and V. Vapnik, "Support-vector networks," *Machine Learning*, vol. 20, no. 3, pp. 273-297, 1995.

[26] Q. Yuan, Q. Chen, and K. Sawaya, "Accurate DOA estimation using array antenna with arbitrary geometry," *IEEE Transactions on Antennas and Propagation*, vol. 53, no. 4, pp. 1352-1357, 2005.

[27] A Practical Approach to Identifying and Tracking Unauthorized 802.11 Cards and Access Points. http://www.interlinknetworks.com/graphics/news/wireless_detection_and_tracking.pdf

[28] ANSYS[EB/OL]. http://www.ansys.com/Products/Simulation+Technology/Electromagnetics/High-Performance+Electronic+Design/ANSYS+HFSS

Dan Shi received Ph.D. degree in Electronic Engineering from Beijing University of Posts & Telecommunications, Beijing, China in 2008.

She has been working in Beijing University of Posts & Telecommunications. Her interests include electromagnetic compatibility, electromagnetic environment and electromagnetic computation.

Shi has published more than 100 papers. She is Chair of IEEE EMC Beijing Chapter, Vice Chair of URSI E-Commission in China, General Secretary of EMC Section of China Institute of Electronics.

Yougang Gao received his B.S degree in Electrical Engineering from National Wuhan University, China in 1950. He was a Visiting Scholar in Moscow Technical University of Communication and Information in Russia from 1957 to 1959. He is now a Professor and Ph.D. Supervisor in Beijing University of Posts and Telecommunications, China. He has been an Academician of International Informatization Academy of UN since 1994. He was once the Chairman of IEEE Beijing EMC Chapter and Chairman of China National E-Commission for URSI. He has published several books: Introduction of EMC, Inductive Coupling and Resistive Coupling, as well as Shielding and Grounding (all these books were published by People's Posts and Telecommunications Press). He became an EMP Fellow of US Summa Foundation since 2010.

A Null Broadening Beamforming Approach Based on Covariance Matrix Expansion

Wenxing Li [1], Yu Zhao [1], Qiubo Ye [2], and Si Li [1]

[1] College of Information and Communications Engineering
Harbin Engineering University, Harbin, 150001, China
liwenxing@hrbeu.edu.cn, zhaoyu0816@hrbeu.edu.cn, lisi@hrbeu.edu.cn

[2] Department of Electronics
Carleton University, Ottawa, Canada
qiubo.ye.1997@ieee.org

Abstract ─ In order to improve the performance of antenna array beamforming in the case of jammer motion, a null broadening beamforming approach based on covariance matrix expansion is proposed in this paper. The covariance matrix of the array is expanded through the Kronecker product of an eye matrix and the sample covariance matrix. The steering vector of the array is also expanded. When the expanded covariance matrix is used for beamforming, more linear constraints can be constructed compared with the original sample covariance matrix, so wider and deeper nulls can be obtained with equal number of array elements, or similar performance can be obtained with fewer number of array elements. Necessary numerical procedures are provided and computation complexity is analyzed. The validity of the proposed approach is verified by theoretical analysis and simulation results.

Index Terms ─ Beamforming, covariance matrix expansion, null broadening.

I. INTRODUCTION

Adaptive antenna beamforming has been widely used in radar, sonar, mobile communications and other fields. It helps adaptive arrays improve the reception of the desired signal and suppress interferences by forming nulls at the directions of interferences [1-4]. The performance of the adaptive arrays is severely degraded if the weights of the arrays are not able to adapt sufficiently fast to the changing (nonstationary) jamming situation or to the antenna platform motion. This issue can be handled, however, if a broad null is formed toward the direction of the interference [5-7].

Broad nulls can be formed by the approach of covariance matrix taper (CMT) [8-11], the concept of which is introduced in [10]. The CMT approach does not need prior knowledge of the directions of interferences. Broad nulls will be formed at all the directions of interferences adaptively, and the width of the nulls can be controlled. However, as a price, the depth of the nulls will be reduced.

Quadratic constraint sector suppressed (QCSS) is another approach of null broadening [12, 13]. The QCSS approach needs prior knowledge of the approximate directions of interferences. Broad nulls can be formed around the directions specified, that is to say, the directions of broad nulls can be controlled. In addition, both the width and depth of the nulls can be controlled by the QCSS approach, and the depth of the nulls can be increased. However, the solving process of the QCSS approach is complicated, which is a nonlinear problem. The approach of linear constraint sector suppressed (LCSS) [14] is proposed based on the QCSS approach. The quadratic constraint is transformed into a set of linear constraints, by which the nonlinear problem is transformed into a linear problem and the solving process is simplified. The LCSS approach is an advanced null broadening beamforming method that forms broad nulls through linear constraints, while it can be further improved. In order to obtain wider or deeper nulls, more linear constraints should be constructed by the LCSS approach, which requires more degrees of freedom (DOFs) of an antenna array, so the DOFs of the antenna array is a restrictive factor to the LCSS approach.

Virtual antenna array is an advanced technique that focuses on the methods of forming virtual array elements and transforms the real array into virtual array, which mainly includes the methods of virtual array transformation [15-17] and high order cumulant [18-20]. By using the idea of the virtual antenna array that forms virtual array elements, a null broadening beamforming approach based on covariance matrix expansion (CME) is proposed in this paper. In this proposed approach, the covariance matrix of an array is expanded through the Kronecker product of an eye

Submitted On: May 31, 2016
Accepted On: December 6, 2016

matrix and the sample covariance matrix. The steering vector of the array is expanded as well. Moreover, the LCSS approach is combined. Eventually, the broad nulls are realized. Compared with the LCSS approach, more linear constraints can be constructed by the proposed approach. Therefore, when the numbers of the array elements of the two approaches are equal, wider and deeper nulls can be obtained by the proposed approach and the output signal-to-interference-plus-noise ratio (SINR) can be improved. Besides, similar performance can be obtained by the proposed approach with fewer number of array elements compared with the LCSS approach. The validity of the proposed approach is verified by theoretical analysis and simulation results.

II. SIGNAL MODEL AND THE QCSS APPROACH

Assuming that noncoherent narrowband excitation sources are far away from the antenna array, we consider a uniform linear array (ULA) with N elements and the element space is equal to one-half wavelength. The structure of the ULA antenna is shown in Fig. 1.

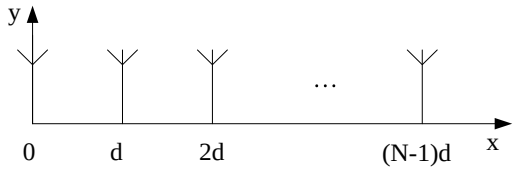

Fig. 1. The structure of the ULA antenna.

The received data $\mathbf{X}(t)$ can be expressed as follows:

$$\mathbf{X}(t) = \mathbf{A}\mathbf{S}(t) + \mathbf{N}(t), \quad (1)$$

where $\mathbf{X}(t)$ is an $N \times 1$ snap data vector, $\mathbf{A}$ is the matrix of steering vectors, $\mathbf{S}(t)$ is the complex signal envelope, and $\mathbf{N}(t)$ is the noise of the antenna array.

If $\mathbf{W} = [\mathbf{w}_1, \cdots, \mathbf{w}_N]^T$ is the weight vector of the antenna array, the output power of the array can be expressed as follows:

$$P_{out} = E\left\{\left|\mathbf{W}^H \mathbf{X}(t)\right|^2\right\} = \mathbf{W}^H \mathbf{R}_{i+n} \mathbf{W}, \quad (2)$$

where $E\{\cdot\}$ denotes expectation, $(\cdot)^H$ denotes conjugate transpose, and $\mathbf{R}_{i+n}$ is the covariance matrix of interference-plus-noise. In practice, this matrix is commonly replaced by the sample covariance matrix with K snapshots as $\hat{\mathbf{R}} = 1/K \sum_{k=1}^{K} \mathbf{X}(k)\mathbf{X}^H(k)$.

Assume that the direction of the source of interest, denoted by θ_d, is constant during the observation time $0 \le t \le T$. When the interference direction changes around θ_i and the total variation is $\Delta\theta_i$, the optimal weight vector $\mathbf{W}_{opt}$ of the QCSS approach will minimize the output power P_{out}. In addition, the desired signal level should be kept and the average output power within the sector $\Delta\theta_i$ should be lower than a pre-set value η in order to obtain a broad null with certain depth. These can be expressed as follows:

$$\min_{\mathbf{W}} \mathbf{W}^H \hat{\mathbf{R}} \mathbf{W} \quad \text{s.t.} \quad \mathbf{W}^H \mathbf{a}(\theta_d) = 1, \ \mathbf{W}^H \mathbf{Q} \mathbf{W} \le \eta, \quad (3)$$

where $\mathbf{a}(\theta_d)$ denotes the steering vector of the desired signal, and $\mathbf{Q}$ is a matrix of $N \times N$ and can be expressed as:

$$\mathbf{Q} = \frac{1}{\Delta\theta_i} \int_{\theta_i - \Delta\theta_i/2}^{\theta_i + \Delta\theta_i/2} \mathbf{a}(\theta)\mathbf{a}^H(\theta) d\theta. \quad (4)$$

The solving process of the optimal weight vector of the array in formula (3) is complicated, which is a nonlinear problem involving the quadratic constraint. To reduce the complexity of the QCSS approach, the LCSS approach was proposed in [14], which replaced the quadratic constraint by a set of linear constraints.

III. THE LCSS APPROACH

Ideally, the goal of null broadening is to obtain a zero power response at the sector $\Delta\theta_i$, that is, $\mathbf{W}^H \mathbf{Q} \mathbf{W} = 0$. Since $\mathbf{Q}$ is a Hermitian matrix, it can be factorized as $\mathbf{Q} = \mathbf{U}\mathbf{\Sigma}\mathbf{U}^H$, where $\mathbf{U}$ is an $N \times N$ matrix containing the orthonormal eigenvectors of $\mathbf{Q}$, and $\mathbf{\Sigma}$ is an $N \times N$ diagonal matrix containing the eigenvalues of $\mathbf{Q}$ in a decreasing order. Assume that $\mathbf{Q}$ has a rank equal to r, and $\mathbf{U}_r = [\mathbf{u}_1, \cdots, \mathbf{u}_r]$ is the matrix of eigenvectors that correspond to the larger eigenvalues. Then, the quadratic constraint $\mathbf{W}^H \mathbf{Q} \mathbf{W} = 0$ is satisfied if $\mathbf{W}^H \mathbf{U}_r = \mathbf{0}$. Therefore, the quadratic constraint can be transformed into a set of linear constraints, and the optimal weight vector of the array can be obtained as follows [14]:

$$\min_{\mathbf{W}} \mathbf{W}^H \mathbf{R} \mathbf{W} \ \text{ s.t. } \mathbf{W}^H \mathbf{C} = \mathbf{e}_1^T, \quad (5)$$

where $\mathbf{C} = [\mathbf{a}(\theta_d), \mathbf{U}_r]$, and $\mathbf{e}_1 = [1, \mathbf{0}^T]^T$. The solution to (5) is:

$$\mathbf{W}_{LCSS}(r) = \mathbf{R}^{-1}\mathbf{C}(\mathbf{C}^H \mathbf{R}^{-1} \mathbf{C})^{-1} \mathbf{e}_1, \quad (6)$$

where the rank r is the number of linear constraints that minimize the average output power of the sector $\Delta\theta_i$. Similar to the QCSS approach, in practice, $\mathbf{R}$ is first replaced with the sample covariance matrix $\hat{\mathbf{R}}$, and then the sample matrix inversion method can be applied where we calculate $\hat{\mathbf{R}}^{-1}$ selectively with or without diagonal loading (DL).

The minimal number r'_{opt} of linear constraints, which needs to be determined to ensure that the average

output power of the sector $\Delta\theta_i$ is lower than the pre-set value η, can be expressed as [14]:

$$r'_{opt} = \arg\min_{r'=[1,2,\cdots,N]} q(r') \le \eta \,, \tag{7}$$

where $q(r') = \mathbf{W}_{LCSS}^H(r')\mathbf{Q}\mathbf{W}_{LCSS}(r')$.

When the DOFs of a real array are more than the optimal rank r'_{opt}, the broad nulls can be achieved by the LCSS approach and the interferences can be suppressed. However, if the DOFs of the real array are less than the optimal rank r'_{opt}, the width or depth of nulls will not be able to reach the requirements. Hence, the performance of the LCSS approach can be improved by increasing the DOFs of the array to construct more linear constraints.

IV. THE CME-LCSS APPROACH

A. The proposed approach

The LCSS approach is an advanced null broadening beamforming method. However, more DOFs of the array will be needed when the performance of the LCSS approach is improved. To solve the problem, the covariance-matrix-expansion-based LCSS (CME-LCSS) approach is proposed in this paper. Compared with the LCSS approach, more linear constraints can be constructed by the CME-LCSS approach and the width and depth of nulls can be improved.

An eye matrix is used to expand the sample covariance matrix $\hat{\mathbf{R}}$. The expanded matrix $\tilde{\mathbf{R}}$ can be expressed as follows:

$$\tilde{\mathbf{R}} = \mathbf{I} \otimes \hat{\mathbf{R}} \,, \tag{8}$$

where $\mathbf{I}$ is an eye matrix of $N \times N$ order and $\otimes$ denotes the Kronecker product. The steering vector of the antenna array is expanded as:

$$\mathbf{b}(\theta) = \mathbf{a}(\theta) \otimes \mathbf{a}(\theta) \,. \tag{9}$$

It can be observed from formula (8) that the sample covariance matrix, $\hat{\mathbf{R}}$ (of $N \times N$ order), is expanded to matrix $\tilde{\mathbf{R}}$ (of $N^2 \times N^2$ order). From formula (9), the steering vector, $\mathbf{a}(\theta)$ (of $N \times 1$ order), of the real antenna array is expanded to the steering vector, $\mathbf{b}(\theta)$ (of $N^2 \times 1$ order), of the virtual antenna array. Therefore, virtual antenna array elements are formed and more linear constraints can be constructed.

Ideally, the goal of null broadening is to obtain a zero power response at the sector $\Delta\theta_i$, that is, $\mathbf{W}^H\bar{\mathbf{Q}}\mathbf{W} = 0$. It can be obtained according to the steering vector of virtual antenna array as follows:

$$\bar{\mathbf{Q}} = \frac{1}{\Delta\theta_i}\int_{\theta_i - \Delta\theta_i/2}^{\theta_i + \Delta\theta_i/2} \mathbf{b}(\theta)\mathbf{b}^H(\theta)d\theta \,, \tag{10}$$

where $\bar{\mathbf{Q}}$ is a matrix of $N^2 \times N^2$ order.

We can factorize it as $\bar{\mathbf{Q}} = \bar{\mathbf{U}}\bar{\mathbf{\Sigma}}\bar{\mathbf{U}}^H$, where $\bar{\mathbf{U}}$ is an $N^2 \times N^2$ matrix containing the orthonormal eigenvectors of $\bar{\mathbf{Q}}$, and $\bar{\mathbf{\Sigma}}$ is an $N^2 \times N^2$ diagonal matrix containing the eigenvalues of $\bar{\mathbf{Q}}$ in a decreasing order. Assume that $\bar{\mathbf{Q}}$ has a rank equal to $\bar{r}$, then $\bar{\mathbf{U}}_{\bar{r}} = [\bar{\mathbf{u}}_1, \cdots, \bar{\mathbf{u}}_{\bar{r}}]$ is the matrix of eigenvectors that corresponding to larger eigenvalues. The quadratic constraint $\mathbf{W}^H\bar{\mathbf{Q}}\mathbf{W} = 0$ is satisfied if $\mathbf{W}^H\bar{\mathbf{U}}_{\bar{r}} = \mathbf{0}$. Therefore, the quadratic constraint can be transformed into a set of linear constraints, and the optimal weight vector of the array can be obtained as follows:

$$\min_{\mathbf{W}} \mathbf{W}^H\tilde{\mathbf{R}}\mathbf{W} \text{ s.t. } \mathbf{W}^H\bar{\mathbf{C}} = \bar{\mathbf{e}}_1^T \,, \tag{11}$$

where $\bar{\mathbf{C}} = [\mathbf{b}(\theta_d), \bar{\mathbf{U}}_{\bar{r}}]$ and $\bar{\mathbf{e}}_1 = [1, \mathbf{0}^T]^T$.

According to the Lagrange multipliers, we define:

$$L(\mathbf{W}) = 1/2\,\mathbf{W}^H\tilde{\mathbf{R}}\mathbf{W} + \mu^H(\bar{\mathbf{e}}_1 - \bar{\mathbf{C}}^H\mathbf{W}). \tag{12}$$

The solution of $\partial L(\mathbf{W})/\partial\mathbf{W} == 0$ is $\mathbf{W} = \tilde{\mathbf{R}}^{-1}\bar{\mathbf{C}}\mu$. Substituting $\mathbf{W}$ into $\mathbf{W}^H\bar{\mathbf{C}} = \bar{\mathbf{e}}_1^H$, we can obtain that $\mu = (\bar{\mathbf{C}}^H\tilde{\mathbf{R}}^{-1}\bar{\mathbf{C}})^{-1}\bar{\mathbf{e}}_1$. Finally, μ is substituted into $\mathbf{W}$.

The optimal weight vector of the CME-LCSS approach can be expressed as follows:

$$\mathbf{W}_{CME-LCSS}(\bar{r}) = \tilde{\mathbf{R}}^{-1}\bar{\mathbf{C}}(\bar{\mathbf{C}}^H\tilde{\mathbf{R}}^{-1}\bar{\mathbf{C}})^{-1}\bar{\mathbf{e}}_1 \,. \tag{13}$$

Similar to the LCSS approach, the optimal number $\bar{r}'_{opt}$ of linear constraints for the CME-LCSS approach, which needs to be determined to ensure that the average output power of the sector $\Delta\theta_i$ is lower than the pre-set value η, can be expressed as:

$$\bar{r}'_{opt} = \arg\min_{r'=[1,2,\cdots,2N-1]} q(\bar{r}') \le \eta \,, \tag{14}$$

where $q(\bar{r}') = \mathbf{W}_{CME-LCSS}^H(\bar{r}')\bar{\mathbf{Q}}\mathbf{W}_{CME-LCSS}(\bar{r}')$.

DL can be selectively used to improve the stability of the LCSS approach, and the loading to noise ratio (LNR) is $10dB$. The performance of the CME-LCSS approach can also be further improved with DL with the same $LNR = 10dB$.

B. Theoretical analysis

Firstly, the relationship between the sample covariance matrix and the expanded covariance matrix is illustrated. According to Schmidt's orthogonal subspace resolution theory, the sample covariance matrix can be expressed as:

$$\hat{\mathbf{R}} = \hat{\mathbf{U}}\hat{\mathbf{\Sigma}}\hat{\mathbf{U}}^H \,, \tag{15}$$

where $\hat{\mathbf{U}}$ is a matrix containing the orthonormal eigenvectors of $\hat{\mathbf{R}}$, and $\hat{\mathbf{\Sigma}}$ is a diagonal matrix

containing the eigenvalues of $\hat{\mathbf{R}}$ in a decreasing order. The eigenvectors in $\hat{\mathbf{U}}$ correspond to the incident directions of signals and interferences. The eigenvalues in $\hat{\mathbf{\Sigma}}$ correspond to the power of signals and interferences.

Substituting formula (15) into formula (8) and using the properties of Kronecker product [22], we know that:

$$\begin{aligned}\tilde{\mathbf{R}} &= \mathbf{I}\otimes\hat{\mathbf{R}}\\ &= \mathbf{I}\otimes\left(\hat{\mathbf{U}}\hat{\mathbf{\Sigma}}\hat{\mathbf{U}}^{H}\right)\\ &= \left(\mathbf{I}\otimes\hat{\mathbf{U}}\right)\left(\mathbf{I}\cdot\mathbf{I}^{H}\otimes\hat{\mathbf{\Sigma}}\hat{\mathbf{U}}^{H}\right)\\ &= \left(\mathbf{I}\otimes\hat{\mathbf{U}}\right)\left(\mathbf{I}\otimes\hat{\mathbf{\Sigma}}\right)\left(\mathbf{I}\otimes\hat{\mathbf{U}}\right)^{H}\\ &= \tilde{\mathbf{U}}\tilde{\mathbf{\Sigma}}\tilde{\mathbf{U}}^{H}\end{aligned}, \quad (16)$$

where:

$$\begin{aligned}\tilde{\mathbf{U}} &= \mathbf{I}\otimes\hat{\mathbf{U}}\\ \tilde{\mathbf{\Sigma}} &= \mathbf{I}\otimes\hat{\mathbf{\Sigma}}\end{aligned}. \quad (17)$$

It can be seen from formula (17) that both $\hat{\mathbf{U}}$ and $\hat{\mathbf{\Sigma}}$ are expanded with an eye matrix. Therefore, the information of the incident directions and the power contained in the expanded matrix $\tilde{\mathbf{R}}$ is the same as that in the sample covariance matrix $\hat{\mathbf{R}}$.

Secondly, the relationship between the steering vectors of the real antenna array and the virtual antenna array is illustrated.

Since the antenna array is an ULA, its steering vector $\mathbf{a}(\theta)=\left[1, e^{j\frac{2\pi}{\lambda}d\sin\theta}, \cdots, e^{j\frac{2\pi}{\lambda}(N-1)d\sin\theta}\right]^{T}$ is a vector of $N\times 1$ order. According to formula (9), we know that $\mathbf{b}(\theta)$ is a vector of $N^2\times 1$ order, in which there are $2N-1$ non-repetitive elements. To describe this more clearly, the expansion of steering vector is shown in Fig. 2 as follows.

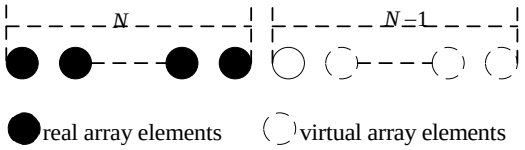

Fig. 2. Schematic diagram of expansion of the steering vector of the antenna array.

It is observed from Fig. 2 that the antenna array is expanded and virtual array elements are formed. There are $2N-1$ non-repetitive array elements, therefore more linear constraints can be constructed compared with the real antenna array. The computational load of the proposed approach is increased as the price. The computation complexity of the LCSS approach is $O(JN^2)+O(N^3)$, where J is the number of sampled points in $\Delta\theta_i$. The computation complexity of the CME-LCSS approach is $O(JN^4)+O(N^6)$, which is greater than that of the LCSS approach. Therefore, the CME-LCSS approach is more applicable to enhancing the situation where the LCSS approach for broadening nulls is not effective because the number of array elements is not large enough.

V. NUMERICAL EXAMPLES AND SIMULATION

Assuming that the noncoherent narrowband excitation sources are far away from the antenna array and the element space is equal to one-half wavelength. The desired signal illuminates on the antenna array in the direction of 0°. Three independent interferences are from the directions of -50°, 20° and 60°. The signal to noise ratio (SNR) is $0dB$. The interferences to noise ratio (INR) is $30dB$. The number of snapshots is 200. With these given conditions, we demonstrate the performance of the CME-LCSS approach and the LCSS approach via computer simulations. In the end, numerical simulation procedures are described.

A. Example 1

The number of array elements is 15. Assume that the widths of broad nulls are set to 10°. Broad nulls are formed around the three directions of -50°, 20° and 60°. To compare the CME-LCSS approach with the LCSS approach, Fig. 3 shows the beam patterns of the two approaches versus the azimuth angle.

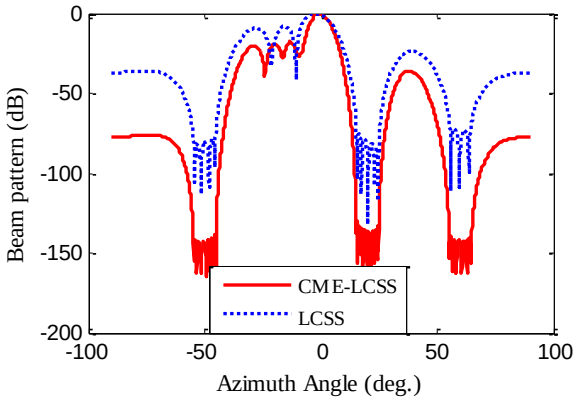

Fig. 3. Beam patterns of the two approaches.

It can be observed from Fig. 3 that broad nulls are formed around the three interferences. The null depth of

the CME-LCSS approach is about $-130dB$, while the null depth of the LCSS approach is about $-75dB$. Compared with the LCSS approach, deeper nulls can be obtained by the CME-LCSS approach.

B. Example 2

The number of array elements is 10. Assume that the broad nulls, whose widths are both set to 10°, are formed around the directions of -50° and 60°. To compare the CME-LCSS approach with the LCSS approach when the null widths are equal, Fig. 4 shows the beam patterns of the two approaches versus the azimuth angle.

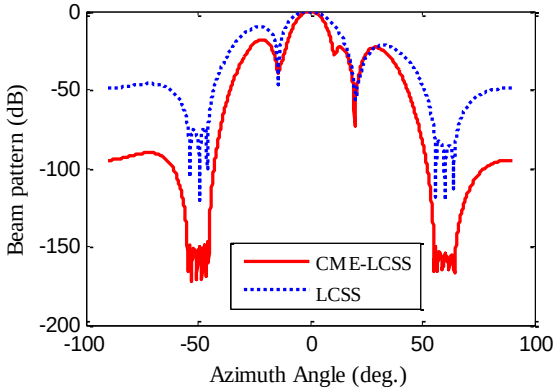

Fig. 4. Beam patterns of the two approaches.

It can be observed from Fig. 4 that broad nulls can be formed around the interferences selectively. Besides, the null depth of the CME-LCSS approach is about $-140dB$, while the null depth of the LCSS approach is about $-80dB$. Compared with the LCSS approach, deeper nulls can be obtained by the CME-LCSS approach.

C. Example 3

Simulation conditions are the same as example 2. While the null width of the CME-LCSS approach is 20° and the LCSS approach is 10°, the performance of the CME-LCSS approach is compared with that of the LCSS approach. Figure 5 shows the beam patterns of the two approaches. Figure 6 shows the output SINR versus the snapshots of the two approaches. Figure 7 shows the output SINR versus the input SNR of the two approaches.

It is observed from Fig. 5 that the null depth of the CME-LCSS approach is about $-110dB$ when the null width is 20°, and the null depth of the LCSS approach is about $-80dB$ when the null width is 10°. Compared with the LCSS approach, deeper and wider nulls can be obtained by the CME-LCSS approach.

From Fig. 6, we know that both approaches need a certain number of snapshots to obtain the stable output SINR, and the output SINR of the CME-LCSS is always higher than that of the LCSS approach.

It can be observed from Fig. 7 that when the input SNR exceeds $10dB$, the output SINR of the two approaches will tend to be stable. Besides, the output SINR of the CME-LCSS approach is always higher than that of the LCSS approach.

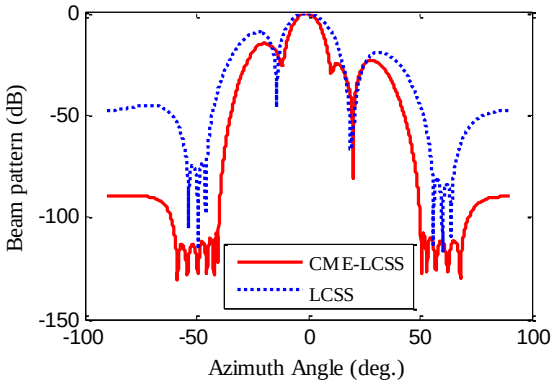

Fig. 5. Beam patterns of the two approaches.

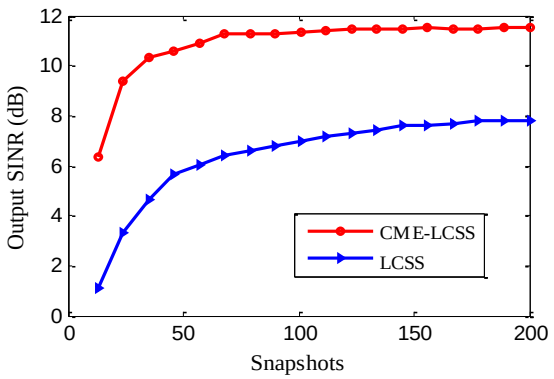

Fig. 6. Output SINR versus snapshots.

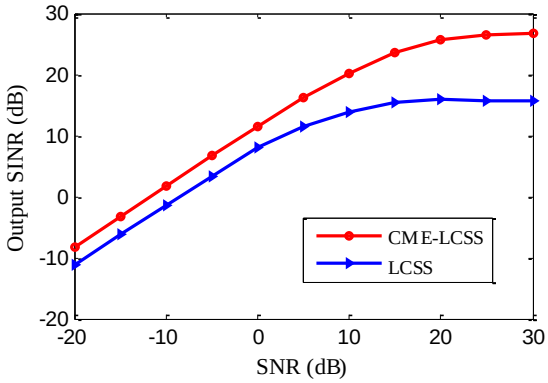

Fig. 7. Output SINR versus input SNR.

D. Example 4

Simulation conditions are the same as Example 3. Both of the CME-LCSS and the LCSS approach are used with DL ($LNR = 10dB$). Figure 8 shows the output SINR versus input SNR of the two approaches.

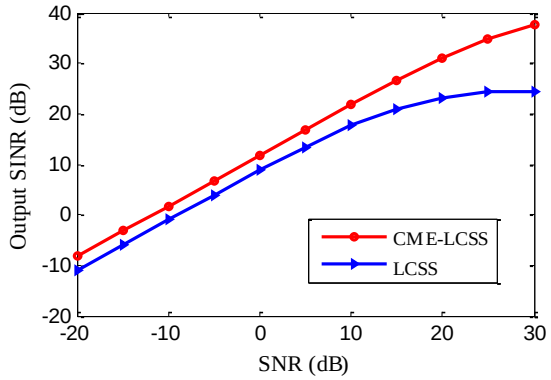

Fig. 8. Output SINR versus input SNR with DL.

It is observed from Fig. 8 that the output SINR of the two approaches will tend to stable when the input SNR exceeds $20dB$, that is to say, the performance of the two approaches are both improved.

E. Example 5

The CME-LCSS approach is used in an array with 10 elements, while the LCSS approach is used in an array with 19 elements. Broad nulls with widths of both 20°, are formed around the directions of -50° and 60°. Figure 9 shows the beam patterns of the two approaches.

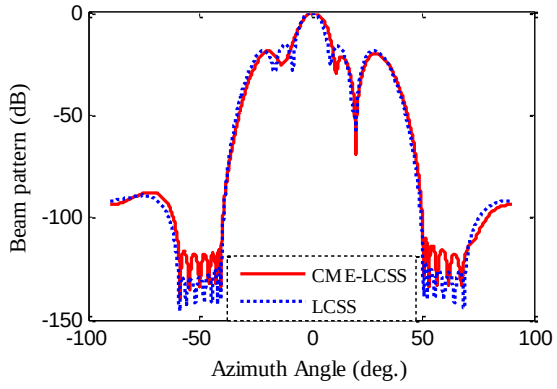

Fig. 9. Beam patterns of the two approaches.

It is observed form Fig. 9 that the beam patterns of the two approaches are similar. Therefore, approximate performance can be obtained by the CME-LCSS approach with fewer array elements compared with the LCSS approach.

F. Numerical simulation procedures

To numerically calculate formula (10), discrete points are taken in $\Delta\theta_i$ with equal spacing, and the integral operation is approximately obtained though the summing operation as follows:

```
theta0=lb:0.01:rb;
 for i=1:length(theta0)
   A=exp(-j*2*pi *[0:N-1]'*sin(theta0(i)) *d /lamda);
   B=kron(A, A);
   Q_bar=B*B'+Q_bar;
 end
```

where 'lb' and 'rb' stand for the boundary of $\Delta\theta_i$, 'kron' stands for the Kronecker product, 'A' stands for $\mathbf{a}(\theta)$ and 'B' stands for $\mathbf{b}(\theta)$. As the number of discrete points increases, the accuracy of $\bar{\mathbf{Q}}$ will increase. However, the computation complexity of the CME-LCSS approach will be greater.

The matrix of linear constraints $\bar{\mathbf{C}}$ in formula (11) can be calculated as follows:

```
[V, D]=eig(Q_bar);
C_bar=[kron(Ad, Ad), V (:,1:lc)];
```

where 'eig' stands for eigen-decomposition, 'V' stands for the eigenvectors matrix of $\bar{\mathbf{Q}}$, 'D' stands for the eigenvalues matrix of $\bar{\mathbf{Q}}$, 'Ad' stands for the steering vector of the desired signal, and 'lc' stands for the number of linear constraints that corresponding to the large eigenvalues of $\bar{\mathbf{Q}}$. Then, the optimal weight vector of the CME-LCSS approach can be obtained using formula (13).

VI. CONCLUSION

A covariance-matrix-expansion-based linear constraint sector suppressed (CME-LCSS) beamforming approach is proposed in this paper. Numerical solution procedures of CME-LCSS are provided and computation complexity is analyzed and compared between CME-LCSS and LCSS. It is verified by simulations that, compared with the LCSS approach, more linear constraints can be constructed by the CME-LCSS approach, so wider and deeper nulls can be obtained with equal number of array elements, or similar performance can be obtained with fewer number of array elements.

ACKNOWLEDGMENT

This paper was supported by National Defense "973" Basic Research Development Program of China (No. 6131380101). This paper is also supported by Pre-Research Fund of the 12th Five-Year Plan

(No. 4010403020102) and the Fundamental Research Funds for the Central Universities (HEUCFD1433, HEUCF1508).

REFERENCES

[1] Z. D. Zaharis, C. Skeberis, and T. D. Xenos, "Improved antenna array adaptive beamforming with low side lobe level using a novel adaptive invasive weed optimization method," *Progress In Electromagnetics Research*, vol. 124, pp. 137-150, 2012.

[2] W. X. Li, X. J. Mao, W. H. Yu, Y. S. Li, and C. Y. Yue, "Robust adaptive array beamforming based on modified norm constraint algorithm," *Applied Computational Electromagnetics Society*, vol. 29, no. 12, pp. 1060-1066, 2014.

[3] A. Khabbazibasmenj, S. A. Vorobyov, and A. Hassanien, "Robust adaptive beamforming based on steering vector estimation with as little as possible prior information," *IEEE Trans. Signal Processing*, vol. 60, no. 6, pp. 2974-2987, 2012.

[4] R. L. Haupt, "Adaptive arrays," *Applied Computational Electromagnetics Society*, vol. 24, pp. 541-549, 2009.

[5] M. S. Hossain, G. N. Milford, M. C Reed, and L. C. Godara, "Robust efficient broadband antenna array pattern synthesis Technique," *IEEE Trans. Antennas and Propagation*, vol. 62, no. 2, pp. 4537-4546, 2014.

[6] A. B. Gershman, U. Nickel, and J. F. Bohme, "Adaptive beamforming algorithms with robustness against jammer motion," *IEEE Trans. Signal Processing*, vol. 45, no. 7, pp. 1878-1885, 1997.

[7] P. D. Karaminas and A. Manikas, "Super-resolution broad null beamforming for cochannel interference cancellation in mobile radio networks," *IEEE Trans. Vehicular Technology*, vol. 49, no. 3, pp. 689-697, 2000.

[8] R. J. Mailloux, "Covariance matrix augmentation to produce adaptive pattern troughs," *Electronics Letters*, vol. 31, no. 10, pp. 771-772, 1995.

[9] M. Zatman, "Production of adaptive array troughs by dispersion synthesis," *Electronics Letters*, vol. 31, no. 25, pp. 2141-2142, 1995.

[10] J. G. Guerci, "Theory and application of covariance matrix tapers for robust adaptive beamforming," *IEEE Trans. Signal Processing*, vol. 47, no. 4, pp. 977-985, 1999.

[11] F. L. Liu, G. Z. Sun, J. K. Wang, and R. Y. Du, "Null broadening and side lobe control algorithm via multi-parametric quadratic programming for robust adaptive beamforming," *Applied Computational Electromagnetics Society*, vol. 29, no. 4, pp. 307-315, 2014.

[12] M. H. Er, "Technique for antenna array pattern synthesis with controlled broad nulls," *IEE Proceedings H*, vol. 135, no. 6, pp. 375-380, 1988.

[13] L. C. Godara and M. R. Sayyah Jahromi, "An optimized sector nulling technique for broadband antenna array," *International Conference on Signal Processing and Communication System*, 2008.

[14] A. Amar and M. A. Doron, "A linearly constrained minimum variance beamformer with a pre-specified suppression level over a pre-defined broad null sector," *Signal Processing*, vol. 109, pp. 165-171, 2015.

[15] W. X. Li, Y. P. Li, L. L. Guo, and W. H. Yu, "An effective technique for enhancing anti-interference performance of adaptive virtual antenna array," *Applied Computational Electromagnetics Society*, vol. 26, no. 3, pp. 234-240, 2011.

[16] W. X. Li, Y. P. Li, and W. H. Yu, "On adaptive beamforming for coherent interference suppression via virtual antenna array," *Progress In Electromagnetics Research*, vol. 125, pp. 165-184, 2012.

[17] W. X. Li, X. J. Mao, W. H. Yu, and C. Y. Yue, "An effective technique for enhancing direction finding performance of virtual arrays," *International Journal of Antennas and Propagation*, 2014.

[18] M. C. Dogan and J. M. Mendel, "Applications of cumulants to array processing. I. Aperture extension and array calibration," *IEEE Trans. Signal Processing*, vol. 43, no. 5, pp. 1200-1216, 1995.

[19] A. Massoud, A. Osman, and A. Noureldin, "DOA estimation based on fourth order cumulant beamforming for nonuniform linear array of DIFAR sonobuoys," *Computers & Electrical Engineering*, vol. 38, no. 4, pp. 986-993, 2012.

[20] B. Porat and B. Friedlander, "Direction finding algorithms based on high-order statistics," *IEEE Trans. Signal Processing*, vol. 39, no. 9, pp. 2016-2024, 1991.

[21] R. O. Schmidt, "Multiple emitter location and signal parameter estimation," *IEEE Trans. Antennas and Propagation*, vol. 34, no. 2, pp. 276-280, 1986.

[22] J. Brewer, "Kronecker products and matrix calculus in system theory," *IEEE Trans. Circuits and Systems*, vol. 25, no. 9, pp. 772-781, 1978.

Radar Cross Section Reduction of Microstrip Antenna Using Dual-Band Metamaterial Absorber

Alireza Shater [1] and Davoud Zarifi [2]

[1] School of Electrical and Computer Engineering
University of Tehran, Tehran, Iran
a.shater@ut.ac.ir

[2] School of Electrical and Computer Engineering
University of Kashan, Kashan, Iran
zarifi@kashanu.ac.ir

Abstract ─ This paper deals with the design and experimental verification of a dual-band metamaterial radar absorbing structure for the reduction of radar cross section (RCS) of a microstrip antenna. A Metamaterial Absorber (MMA) is designed to work in X-band with absorption rate near 100%. To demonstrate the effective performance of the proposed structure, its influence on RCS and performance of a microstrip antenna is investigated. According to the numerical and measurement results, one can find that the designed antenna shows dual-band RCS reduction within X-band for wide incident angles, while the radiation characteristics of the antenna are sustained without undesired changes.

Index Terms ─ Dual-band absorber, metamaterial, microstrip antenna, radar absorbing materials, radar cross section.

I. INTRODUCTION

Radar cross section (RCS) reduction has long been an interest of the research community. Stealth technology, which reduces visibility to detection radar, has become a more important and interesting research topic. With the development of the modern stealth technology, RCS reduction has received more attention, especially for the military platforms. For example, a stealth platform should have design features that give it a low RCS. For such low RCS platforms, the antennas which are designed to be effective radiators, have also been the main contributors total RCS. The RCS of a conventional antenna can be very large making it an easy target to pick up on basic radar systems. In fact, if such antenna is placed on a stealthy platform, it will destroy the low RCS properties. Thus, research on RCS reduction for antennas is extremely meaningful.

In recent years, many novel techniques have been proposed to RCS reduction of antennas, such as antenna shaping [1], using radar absorbing materials (RAM) [2-4], and using cancellation technology [5], [6]. Antenna shaping is widely used to reduce RCS of antenna. With this technique, RCS can be reduced by changing the structures of the original antennas. Another way is the use of RAMs. For in-band frequencies, it is difficult to reduce the RCS using conventional RAMs; because they would severely degrade the performance of the antenna. However, the use of RAMs for the RCS reduction of antenna usually requires a trade-off between radiation characteristics of antennas and RCS reduction effects. Another way to RCS reduction of antennas is the use of Frequency Selective Surface (FSS) radomes [7-11]. In this case, the FSS is transparent to electromagnetic waves in the operating band of antennas, while the signal outside the operating band is reflected. For out-of-band frequencies, FSS can be employed to reduce the RCS of antenna. However, in order to obtain favorable RCS reduction, a complex conformal shape should be designed which increases the complexity, weight and costs.

In 2008, the design of resonant metamaterial absorber (MMA) with near perfect absorptivity has been proposed at microwave band [12]. Later, many efforts have been made on MMA to achieve wide-angle and polarization-insensitive absorption [13-16], multiband absorption [17-19], and broadband absorption [20], [21]. In this contribution, the objective of the present work is to investigate the effect of a dual-band MMA to RCS reduction of microstrip antennas. The proposed antenna exhibits undisturbed radiation performance and dual-band out-of-band RCS reduction for wide incident angles. Also, this approach keeps the advantages of lightweight, low-profile, easy conformal and easy manufacturing nature of the original antenna.

II. DESIGN OF DUAL-BAND MMA STRUCTURE

The layout of the dual-band MMA structure is shown in Fig. 1. The unit cell of this structure constructed

Submitted On: September 29, 2016
Accepted On: December 10, 2016

by two metal loops patterned on the FR-4 board. The relative dielectric constant of FR-4 board is 4.35 with a dielectric loss tangent of 0.02. The electromagnetic properties of our proposed structure are characterized using full-wave simulations. Numerical simulations are performed by using periodic boundary condition template and the frequency-domain solver of the CST Microwave Studio (Computer Simulation Technology GmbH, Dermstadt, Germany), which uses a finite element method to determine transmission and reflection coefficients. Unit cell boundary conditions with a tetrahedral mesh were used in the frequency solver, in which case the wave ports were automatically added in the direction of normal incidence to the substrate. The variations of resonant frequency of single-band MMA with parameter l_1 are presented in Fig. 2. It can be clearly seen that, with variation of from 4 to 7 mm, the resonant frequency changes from 12.1 to 5.5 GHz. The presented curve can be used to design arbitrary MMA absorbers. In addition, the proposed dual-band MMA structure can be scaled to achieve desired resonant frequencies.

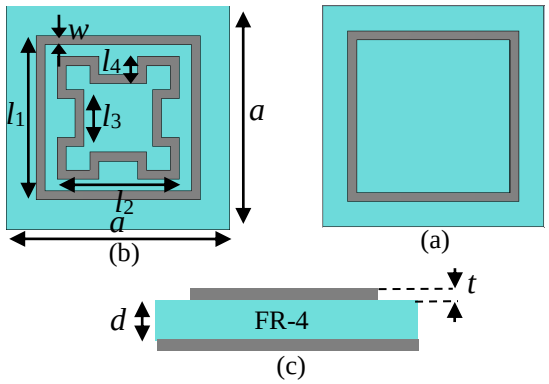

Fig. 1. Unitcell of: (a) single- and (b) dual-band MMA. The dimensions are: a = 7.5, l_1 = 5.5, l_2 = 4.1, l_3 = 1.9, l_4 = 0.9, w = 0.3, and d = 0.8.

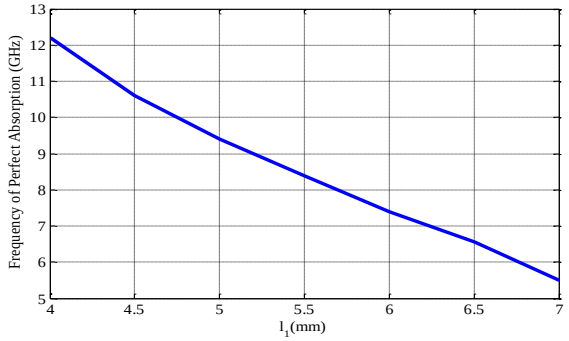

Fig. 2. Variations of resonant frequency of the single-band MMA with parameter l_1.

The designed idea is to adjust the effective and independently by varying the dimensions of loops in the unit cell so as to match the effective impedance of the structure to free space and achieve a large resonant dissipation in the meantime. Thus, wave transmission and reflection are minimized simultaneously and absorption is maximized. Based on this, the geometry and dimensions of the loops are optimized to achieve two resonance frequencies at the X-band. The numerical simulations are executed in a frequency range of 8–12 GHz. The absorption is calculated as $A(\omega) = 1 - R(\omega) - T(\omega)$, where $R(\omega) = |S_{11}|^2$ and $T(\omega) = |S_{21}|^2$ are the reflectance and the transmittance, respectively. In this case, the metal backing results in $T(\omega) = 0$.

The simulated absorption as a function of frequency is calculated and shown in Fig. 3 for both TE and TM polarizations at various angles of incidence. Observe that for the both TE and TM case, at normal incidence there appear two absorbing peaks that are attributed to two resonant modes. Two perfect absorptivity peaks operating at 8.4 GHz and 10.9 GHz can be obtained; whose absorptivity ratios come up to 99%, and with increasing angle of incidence, the absorption remains quite large. Briefly, the simulation results show that the performance of the absorption of the structure is independent of the angle of incidence and polarization of electromagnetic wave.

The mechanism of the resonance for the MMA structure can be understood by studying the surface current distributions as shown in Fig. 4. Observe that in the first resonance, the majority of induced currents flow on the larger loop. Similarly, in the second frequency band, the majority of induced currents flow on the smaller loop. This shows that the effective frequency bands of this structure are independent and can be simply adjusted. In fact, with poising the length of larger loop and varying of the length of smaller loop, the first frequency band is fixed, while the second one is replaced. The physical mechanism of the absorption of structure is similar to presented discussion in [22], which uses a model based on the destructive and constructive interferences at interfaces.

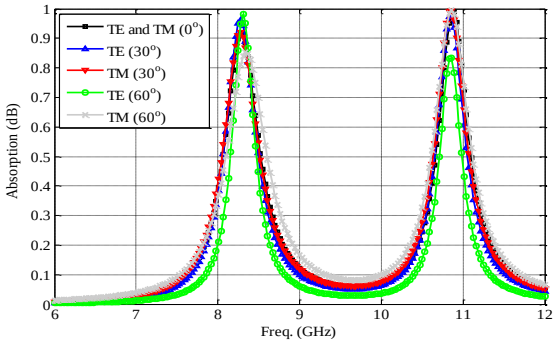

Fig. 3. Absorption of dual-band MMA for various angles of incidence for TE and TM polarizations.

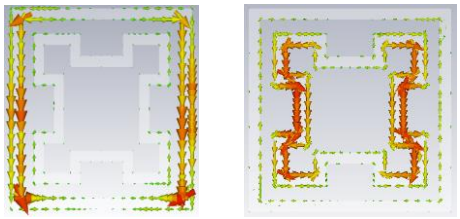

(a) (b)

Fig. 4. The surface current distributions on the unit cell of dual-band MMA at the frequencies of: (a) 8.4 GHz and (b) 10.9 GHz.

III. DESIGN OF LOW RCS MICROSTRIP ANTENNA

The geometry of a microstrip patch antenna is shown in Fig. 5. The microstrip patch antenna can be fed by a variety of methods, such as microstrip line feed, coaxial feed, aperture coupled feed, and proximity coupled feed. Here, due to the simplicity, the coaxial or probe feed is used. In the coaxial feed, the input impedance can be adjusted by the probe's location. The optimized location for feed is in x_f = -2.1, y_f = 0.

The dual-band MMA is applied to the microstrip patch antenna in order to reduce the radar cross section without compromising the performance of antenna. As shown in Fig. 6, this composite structure can act as an antenna as well as an electromagnetic wave absorber.

The simulated S_{11} and radiation pattern of the designed patch antennas with and without MMA are shown in Figs. 7-8. Observe that both of the two microstrip antennas resonated at almost the same frequency of 6.4 GHz with deviation of 50 MHz. Also, according to the results, one can find that the radiation patterns of the proposed antennas in the φ = 0 and φ = 90 planes are almost the same. The gain of antenna with MMA approaches 7.15 dB at 6.4 GHz, while the common antenna without MMA has gain of 7.2 dB. The total efficiency of the designed antennas with and without MMA are 52% and 51%, respectively.

The simulated RCS of the microstrip antenna with and without single- and dual-band MMA are calculated and presented in Fig. 9. It can be seen that the frontal RCS of the antenna with dual-band MMA declined from -10 to -30 dBsm and from -8 to -19 dBsm at the frequencies of 8.35 and 11.1 GHz, respectively. Notice that the resonance frequencies of the MMA obtained in the prior sections are valid for a very large structure consisting of many unit cells. Here, due to the physical constraints, the transverse dimensions of the practical MMA should be finite. So, the little difference between the resonance frequencies of the MMA with and without the antenna is due to the finite dimensions of composite structure.

In order to further studies and to illustrate the variation of in-band RCS versus the theta angle, the RCS of antenna with and without MMA in terms of theta angle are shown in Fig. 10. The results show that the RCSs have been effectively reduced within the angular ranges.

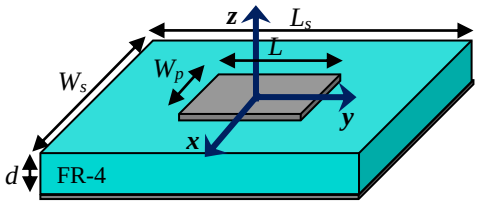

Fig. 5. Microstrip antenna with dimensions of: L_p = 14.6 mm, W_p = 10.6 mm, L_s = 52.5 mm, W_s = 52.5 mm, l_4 = 2.9 mm, and d = 0.8 mm.

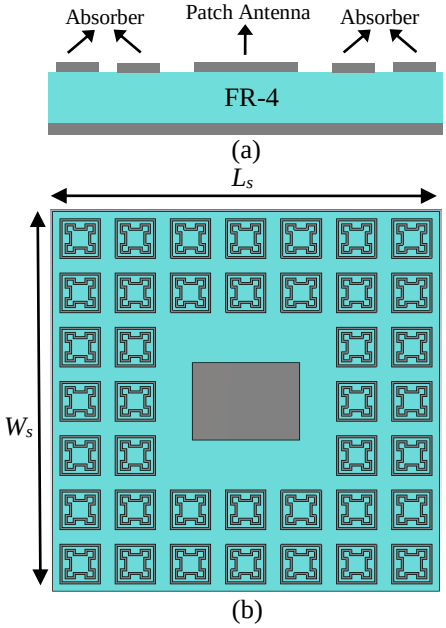

Fig. 6. Configuration of low RCS microstrip antenna. (a) Side view and (b) top view.

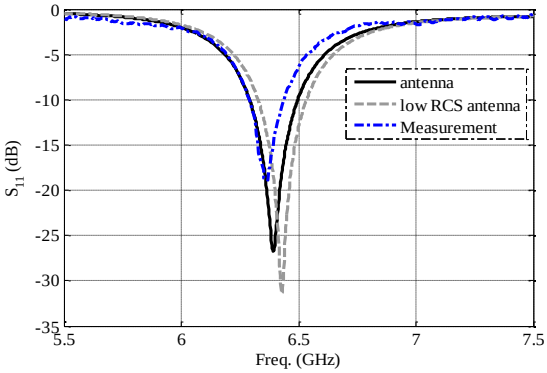

Fig. 7. Simulated reflection coefficients of microstrip antenna with and without MMA.

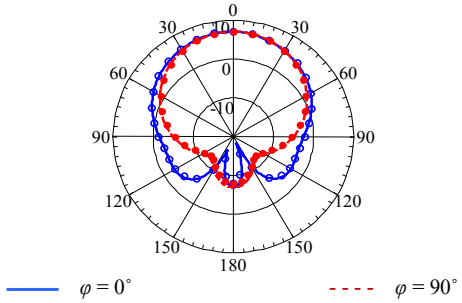

Fig. 8. Comparison of simulated radiation patterns of microstrip antenna with and without MMA at 6.4 GHz. The patterns of low RCS antenna are shown with solid and hollow circles.

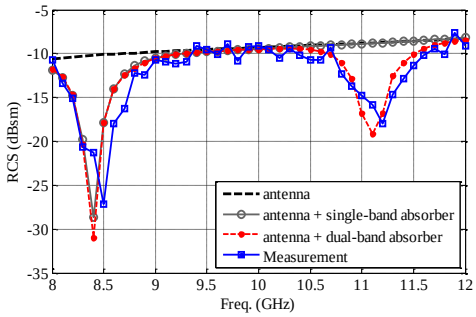

Fig. 9. Comparison of monostatic RCS of microstrip antenna with and without MMA absorber.

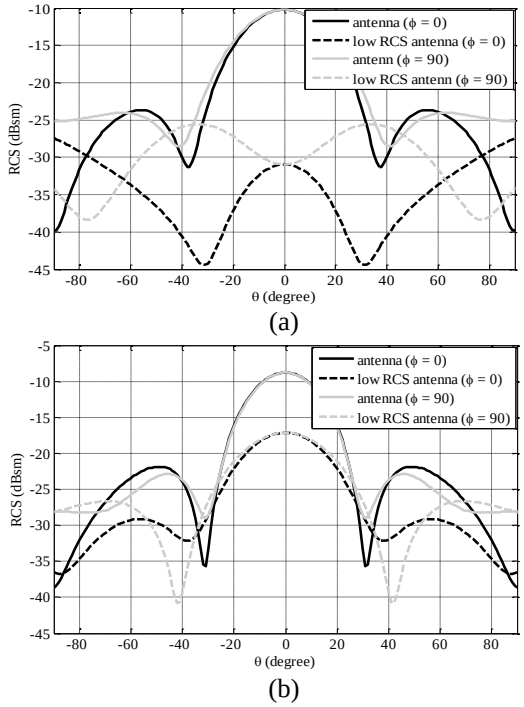

Fig. 10. Simulated monostatic RCS of microstrip antenna with and without absorber at under normal incidence at: (a) 8.4 and (b) 11.1 GHz.

IV. FABRICATION AND MEASUREMENT

To validate the design strategies above, the proposed microstrip antenna with MMA absorber is physically fabricated and practically measured. The photograph of fabricated low RCS antenna is shown in Fig. 11.

The input reflection coefficient measured by an HP8720 network analyzer is depicted in Fig. 7 along with the simulated values. Observe that the numerical and experimental reflection coefficients are in very good agreement. The measured center resonance frequency is 6.38 GHz and the measured S_{11} show a small frequency shifts compared with the simulated one. This discrepancy can be attributed to substrate errors and fabrication precision. The monostatic RCS of microstrip antenna with MMA is measured and shown along with the simulated values in Fig. 9. The simulated and measured backward RCS are in very good agreement. Also, the measured and simulated radiation patterns of low RCS antenna at frequency of 6.38 GHz are compared in Fig. 12.

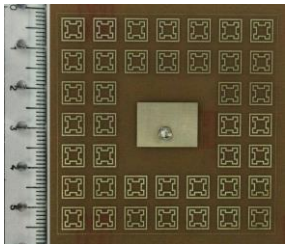

Fig. 11. Photograph of fabricated antenna. The dimensions are: 52.5 × 52.5 × 0.8 mm^3.

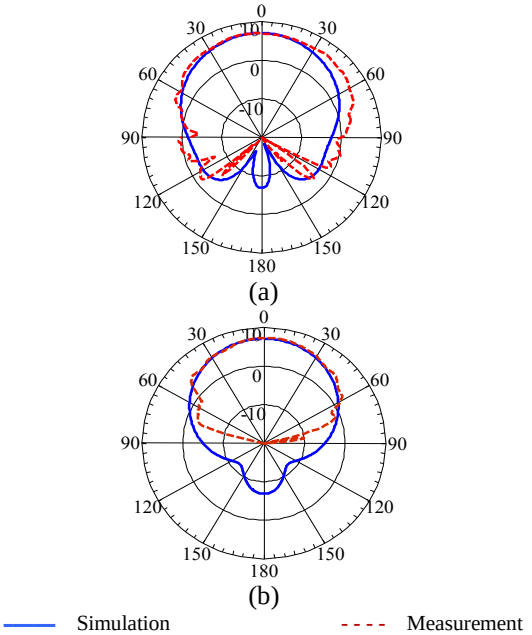

Fig. 12. Comparison of simulated and measured radiation patterns of low RCS microstrip antenna at 6.38 GHz. (a) $\varphi = 0^\circ$ and (b) $\varphi = 90^\circ$.

V. CONCLUSION

Major contribution to the research community discussed in this paper is the RCS reduction of microstrip antenna by using a dual-band MMA. The numerical and experimental results exhibit that it is possible to acquire dual-band RCS reduction by combining microstrip antennas and MMAs. Meanwhile, the performance of microstrip antenna is preserved when the MMA is used. The measured results show that the antenna obtains 20 and 10 dB RCS reduction almost in 8.5 and 11.2 GHz, while its out-band radiation performance is preserved favorably.

REFERENCES

[1] S.-C. Zhao, B.-Z. Wang, and Q.-Q. He, "Broadband radar cross section reduction of a rectangular patch antenna," *Progress In Electromagnetics Research*, vol. 79, pp. 263-275, 2008.

[2] E. F. Knott, J. F. Shaeffer, and M. T. Tuley, *Radar Cross Section*. Raleigh, NC, USA: SciTech, 2004.

[3] K. I. Hopcraft and P. R. Smith, "Geometrical properties of backscattered radiation and their relation to inverse scattering," *J. Opt. Soc. Amer. A*, vol. 6, no. 4, pp. 508-516, 1989.

[4] H. Chen, P. Zhou, L. Chen, and L. Deng, "Study on the properties of surface waves in coated ram layers and monostatic RCS performances of the coated slab," *Progress in Electromagnetics Research M*, vol. 1, pp. 123-135, 2010.

[5] W. Jiang, Y. Liu, S. X. Gong, and T. Hong, "Application of bionics in antenna radar cross section reduction," *IEEE Antennas Wireless Propag. Lett.*, vol. 8, pp. 1275-1278, 2009.

[6] H.-Y. Xu, H. Zhang, K. Lu, and X.-F. Zeng, "A holly-leaf-shaped monopole antenna with low RCS for UWB application," *Progress In Electromagnetics Research*, vol. 117, pp. 35-50, 2011.

[7] H. K. Jang, W. J. Lee, and C. G. Kim, "Design and fabrication of a microstrip patch antenna with a low radar cross section in the X-band," *Smart Mater. Struct.*, vol. 20, p. 015007, 2011.

[8] S. Genovesi, F. Costa, and A. Monorchio, "Low profile array with reduced radar cross section by using frequency selective surfaces," *IEEE Trans. Antennas Propag.*, vol. 60, no. 5, pp. 2327-2335, 2012.

[9] F. Costa, S. Genovesi, and A. Monorchio, "A frequency selective absorbing ground plane for low-RCS microstrip antenna arrays," *Progr. Electromagn. Res.*, vol. 126, pp. 317-332, 2012.

[10] F. Costa and A.Monorchio, "A frequency selective radomes with wideband absorbing properties," *IEEE Transactions on Antennas and Propagation*, vol. 60, no. 6, pp. 2740-2747, 2012.

[11] H. Zhou, S. Qu, B. Lin, and J. Wang, "Filter-antenna consisting of conical FSS radome and monopole antenna," *IEEE Transactions on Antennas and Propagation*, vol. 60, no. 6, pp. 3040-3045, 2012.

[12] N. I. Landy, D. R. Smith, and W. J. Padilla, "A perfect metamaterial absorber," *Phys. Rev. Lett*, vol. 100, p. 207402, 2008.

[13] T. Hu, C. M. Bingham, A. C. Strikwerda, D. Pilon, D. Shrekenhamer, N. I. Landy, K. Fan, X. Zhang, W. J. Padilla, and R. D. Averitt, "Highly-flexible wide angle of incidence terahertz metamaterial absorber," *Phys. Rev. B.*, vol. 78, p. 241103, 2008.

[14] B. Zhu, Z. Wang, C. Huang, Y. Feng, J. Zhao, and T. Jiang, "Polarization insensitive metamaterial absorber with wide incident angle," *Progr. Electromagn. Res.*, vol. 10, no. 1, pp. 231-239, 2010.

[15] F. Dincer, M. Karaaslan, E. Unal, K. Delihacioglu, and C. Sabah, "Design of polarization and incident angle insensitive dual - band metamaterial absorber based on isotropic resonators," *Progr. Electromagn. Res.*, PIER 144, pp. 123-132, 2014.

[16] D. Sood and C. C. Tripathi, "A wideband wide - angle ultra - thin metamaterial microwave absorber," *Progr. Electromagn. Res.*, vol. 44, pp. 39-46, 2015.

[17] Q. Y. Wen, H. W. Zhang, Y. S. Xie, Q. H. Yang, and Y. L. Liu, "Dual band terahertz metamaterial absorber: Design, fabrication, and characterization," *Appl. Phys. Lett.*, vol. 95, p. 241111, 2009.

[18] Y. Liu, Y. Hao, Y. Jia, and S.-X. Gong, "A low RCS dual-frequency microstrip antenna with complementary split-ring resonators," *Progress In Electromagnetics Research*, vol. 146, pp. 125-132, 2014.

[19] G.-D. Wang, J.-F. Chen, X. Hu, Z.-Q. Chen, and M. Liu, "Polarization-insensitive triple-band microwave metamaterial absorber based on rotated square rings," *Progress In Electromagnetics Research*, vol. 145, pp. 175-183, 2014.

[20] J. Lee and S. Lim, "Bandwidth-enhanced and polarisation-insensitive metamaterial absorber using double resonance," *Electron. Lett.*, vol. 47, no. 1, pp. 8-9, 2011.

[21] S. Gu, J. P. Barrett, T. H. Hand, B. I. Popa, and S. A. Cummer, "A broadband low-reflection metamaterial absorber," *J. Appl. Phys.*, vol. 108, p. 064913, 2010.

[22] S. Jamilan, M. N. Azarmanesh, and D. Zarifi, "Design and characterization of a dual-band metamaterial absorber based on destructive interferences," *Progress In Electromagnetics Research C*, vol. 47, pp. 95-101, 2014.

Alireza Shater was born in Iran in 1985. He received the M.Sc. degree from the University of Tehran, Tehran,

Iran, in 2014 in Electrical Engineering. His research interests are inverse problems and metamaterials.

Davoud Zarifi was born in Kashan, Iran, in 1987. He received the Ph.D. degree from the Iran University of Science and Technology, Tehran, Iran, in 2015 in Electrical Engineering. Presently, he is an Assistant Professor in the School of Electrical and Computer Engineering, University of Kashan, Kashan, Iran. His research interests are inverse problems in electro-magnetic, metamaterials and gap waveguide technology.

Noise Suppression Detection Method Based on Time Reversed Signal Waveform Similarity

Bing Li

School of Electrical Engineering
Southwest Jiaotong University, Chengdu 610031, China
bllijess@outlook.com

Abstract ─ A novel time reversal detection (TRD) algorithm for noise suppression is presented. The targets can be located accurately by analyzing the cross-correlation character of TR echo signals received by sub-arrays. Compared with conventional TR algorithm, the performance of proposed method is superior, especially under low signal-to-noise ratio (SNR) condition.

Index Terms ─ Cross-correlation, noise suppression, sub-arrays, time reversal.

I. INTRODUCTION

Time-reversal (TR) methods have attracted much significant attention and interest recently due to their promising use in a wide range of applications. Its basic principle is able to be described as follows: firstly, the channel state information can be extracted by observing the received signal from the sources or scatterers; then, this received signal is time-reversed in time domain (or phase conjugated in the frequency domain) and retransmitted from the respective receiver used as transmitter in this stage; finally, according to the spatial reciprocity principle, the rebroadcast wavefields focus at the locations of the original sources or scatterers. This effect is valuable for many applications in which the energy of acoustic or electromagnetic waves needs to be physically focused at the desired destination, e.g., in communications or biomedical applications [1-4].

Most current TR methods require a large number of echo signals, such as the time reversal multiple-signal-classification (TR-MUSIC) algorithm and decomposition of the time-reversal operator (DORT), these two algorithms need to measure N×N echo signals for constructing the multistatic data matrix (MDM) whose size is N×N, where N is the total number of transceivers [5-8]. Moreover, the conventional TR method also needs to measure a lot of echo signals for improving TR-focusing quality (resolution) and suppressing noise interference.

TR system becomes more practical, low cost and exploitable if few echo signals can be successfully utilized, since making use of few echo signals purports to employ few detection elements [9]. However, when few echo signals are used, the MDM may be unavailable, or multiple spurious images which can be misinterpreted as scatterers may be appearance under noisy conditions.

To address the aforementioned issues, I propose a new TRD approach which can suppress incoherent noise effectively. The general idea of this new approach is as follows: firstly, the detection array is divided into several looks (sub-arrays). Secondly, the echoes received by each sub-array are separately time reversed. Finally, the detection map is able to be obtained by calculating the cross-correlation of TR signals of the sub-arrays. Since the noise is irrelevant to the TR-focusing signal, the proposal method can effectively suppress the noise, even in a situation where few echo signals are available.

Furthermore, the TR signal is easy to be interfered by noise in a simple environment, since the TR-focusing effect gets weak. In contrast, the TR-focusing effect can be strengthened in the cluttered environment where the focal signal can be improved. Therefore, the detection method which works well to suppress noise in the simple environment is able to have a better performance in the cluttered environment. As a result, in this study, an experiment was arranged to investigate the proposal algorithm in a simple environment [8].

It is worthwhile mean that, in order to estimate the impact of noise on the algorithm accurately, the measured experiment was taken in a microwave chamber to obtain low-noise echo signals. And then an extra additive white Gaussian noise is added to the low-noise echoes, so as to obtain the high-noise echo signals. And this additive white Gaussian noise is a good candidate to simulate background noise, thermal noise, inner noise of system, etc. and is often assumed to be zero mean in the image denoising literature [10].

II. NOVEL TRD METHOD

Assume a target located at $\mathbf{r}_s$, an array of N transceivers, and the nth transceiver's receiver and transmitter separately located at $\mathbf{r}_n$ and $\mathbf{r}'_n$. A time domain probing pulse $x(t)$ is emitted from the nth

Submitted On: September 8, 2015
Accepted On: December 24, 2016

transmitter. The Fourier transform of incident signal at the target's location can be represented as:

$$S(\omega,\mathbf{r_s}) = G(\mathbf{r_s},\mathbf{r'_n},\omega)X(\omega), \tag{1}$$

where $X(\omega)$ is the Fourier transform of $x(t)$ and $G(\mathbf{r_s},\mathbf{r'_n},\omega)$ is the background Green function that satisfies the reduced wave equation [11] representing the "propagator" from location $\mathbf{r'_n}$ to $\mathbf{r_s}$. In the presence of additive white Gaussian noise $w_n(t)$ which is called noise for short thereafter, the signal received by the corresponding receiver at $\mathbf{r_n}$ could be modeled as:

$$\begin{aligned}\mathbf{y}(t,\mathbf{r_n},\mathbf{r'_n}) = \frac{1}{2\pi}\int[&G(\mathbf{r_n},\mathbf{r_s},\omega)G(\mathbf{r_s},\mathbf{r'}_n,\omega)X(\omega)\\ &+W_n(\omega)]\mathrm{e}^{i\omega t}\,d\omega,\end{aligned} \tag{2}$$

where $W_n(\omega)$ is the Fourier transform of $w_n(t)$.

Since a TR signal in time domain is equivalent to taking the complex conjugate in frequency domain, the TR version of this response becomes, with the length of the time-window being denoted as T,

$$\begin{aligned}\mathbf{y}_{TR}(T-t,\mathbf{r_n},\mathbf{r'_n}) = \frac{1}{2\pi}\int[&\mathrm{G}^*(\mathbf{r_n},\mathbf{r_s},\omega)G^*(\mathbf{r_s},\mathbf{r'}_n,\omega)X^*(\omega)\\ &+W_n^*(\omega)]\mathrm{e}^{-i\omega T}\,\mathrm{e}^{i\omega t}\,d\omega,\end{aligned} \tag{3}$$

where "$*$" represents the complex conjugate.

Accounting for propagation from the nth transmitter at $\mathbf{r'_n}$ and the nth receiver at $\mathbf{r_n}$ to any point at $\mathbf{r_k}$ in the detection domain, the TR signal for a generic observation point $\mathbf{r_k}$ can be illustrated as:

$$\begin{aligned}f(t,\mathbf{r_k},\mathbf{r_n},\mathbf{r'_n}) = \frac{1}{2\pi}\int[&G^*(\mathbf{r_n},\mathbf{r_s},\omega)G^*(\mathbf{r_s},\mathbf{r'_n},\omega)X^*(\omega)+W_n^*(\omega)]\\ &\times G(\mathbf{r_k},\mathbf{r'_n},\omega)G(\mathbf{r_n},\mathbf{r_k},\omega)\mathrm{e}^{-i\omega T}\,\mathrm{e}^{i\omega t}\,d\omega.\end{aligned} \tag{4}$$

In the proposal method, the transceivers are divided into several sub-arrays (looks), before the received signals are time reversed and resubmitted. Assume each sub-array includes L adjacent transceivers. Therefore, the number of sub-arrays is N-L+1. According to (4), at point $\mathbf{r_k}$, the TR signal of the ath sub-array containing transceivers $n_a....n_a+L-1$ is:

$$\begin{aligned}f_a(t,\mathbf{r_k}) &= \sum_{n=n_a}^{n_a+L-1} f(t,\mathbf{r_k},\mathbf{r_n},\mathbf{r'}_n)\\ &= \frac{1}{2\pi}\int\sum_{n=n_a}^{n_a+L-1} G^*(\mathbf{r_n},\mathbf{r_s},\omega)G^*(\mathbf{r_s},\mathbf{r'_n},\omega)G(\mathbf{r_k},\mathbf{r'_n},\omega)\\ &\quad\times G(\mathbf{r_n},\mathbf{r_k},\omega)X^*(\omega)\mathrm{e}^{-i\omega T}\,\mathrm{e}^{i\omega t}\,d\omega\\ &\quad+\frac{1}{2\pi}\int\sum_{n=n_a}^{n_a+L-1} G(\mathbf{r_k},\mathbf{r'}_n,\omega)G(\mathbf{r_n},\mathbf{r_k},\omega)W_n^*(\omega)\mathrm{e}^{-i\omega T}\,\mathrm{e}^{i\omega t}\,d\omega\\ &= v_a(t,\mathbf{r_k})+u_a(t,\mathbf{r_k}),\end{aligned} \tag{5}$$

where

$$\begin{aligned}v_a(t,\mathbf{r_k}) = \frac{1}{2\pi}\int\sum_{n=n_a}^{n_a+L-1} &G^*(\mathbf{r_n},\mathbf{r_s},\omega)G^*(\mathbf{r_s},\mathbf{r'_n},\omega)G(\mathbf{r_k},\mathbf{r'}_n,\omega)\\ &\times G(\mathbf{r_n},\mathbf{r_k},\omega)X^*(\omega)\mathrm{e}^{-i\omega T}\,\mathrm{e}^{i\omega t}\,d\omega,\end{aligned} \tag{6}$$

$$u_a(t,\mathbf{r_k}) = \frac{1}{2\pi}\int\sum_{n=n_a}^{n_a+L-1} G(\mathbf{r_k},\mathbf{r'_n},\omega)G(\mathbf{r_n},\mathbf{r_k},\omega)W_n^*(\omega)\mathrm{e}^{-i\omega T}\,\mathrm{e}^{i\omega t}\,d\omega. \tag{7}$$

Likewise, $f_b(t,\mathbf{r_k})$, $v_b(t,\mathbf{r_k})$ and $u_b(t,\mathbf{r_k})$ can be got in the same way, and calculate the cross-correlation function between $f_a(t,\mathbf{r_k})$ and $f_b(t,\mathbf{r_k})$,

$$\begin{aligned}D_p(t,\mathbf{r_k}) &= \int_{-\infty}^{\infty} f_a^*(\tau,\mathbf{r_k})\,f_b(t+\tau,\mathbf{r_k})d\tau\\ &= \int_{-\infty}^{\infty} v_a^*(\tau,\mathbf{r_k})v_b(t+\tau,\mathbf{r_k})d\tau+\int_{-\infty}^{\infty} u_a^*(\tau,\mathbf{r_k})v_b(t+\tau,\mathbf{r_k})d\tau\\ &\quad+\int_{-\infty}^{\infty} v_a^*(\tau,\mathbf{r_k})u_b(t+\tau,\mathbf{r_k})d\tau+\int_{-\infty}^{\infty} u_a^*(\tau,\mathbf{r_k})u_b(t+\tau,\mathbf{r_k})d\tau.\end{aligned} \tag{8}$$

Then, the target image can be built by using the following function:

$$I(\mathbf{r_k}) = \sum_{p=1}^{C(N-L+1,\,2)} \left|D_p(0,\mathbf{r_k})\right|, \tag{9}$$

where $C(N-L+1,\,2)$ is the number of 2-combinations from N-L+1 elements. Due to the space focusing and temporal compression of TR signal at point $\mathbf{r_s}$, $f_a(t,\mathbf{r_k})$ is similar to $f_b(t,\mathbf{r_k})$ near the time reference t=T. Therefore, according to Equation (8), the maximum value of cross-correlation function can be obtained at t=0. Furthermore, at the point $\mathbf{r_k}$ ($\mathbf{r_k}\neq\mathbf{r_s}$), $f_a(t,\mathbf{r_k})$ is irrelevant to $f_b(t,\mathbf{r_k})$. That means the value of cross-correlation function at the point $\mathbf{r_s}$ are larger than those at off-target points, namely, $\left|D_p(0,\mathbf{r_s})\right| > \left|D_p(0,\mathbf{r_k})\right|$, ($\mathbf{r_k}\neq\mathbf{r_s}$). With the use of Equation (9), the detection map is built, and the point with the maximum value is the position of target.

In addition, $u_a(t,\mathbf{r_k})$ and $u_b(t,\mathbf{r_k})$ are random and uncorrelated, that means,

$$\int_{-\infty}^{\infty} u_a^*(\tau,\mathbf{r_k})u_b(\tau,\mathbf{r_k})d\tau \cong 0. \tag{10}$$

And the TR echo signals without noise are irrelevant to noise. Therefore, we can get

$$\begin{cases}\int_{-\infty}^{\infty} u_a^*(\tau,\mathbf{r_k})v_b(\tau,\mathbf{r_k})d\tau \cong 0\\ \int_{-\infty}^{\infty} v_a^*(\tau,\mathbf{r_k})u_b(\tau,\mathbf{r_k})d\tau \cong 0\end{cases}. \tag{11}$$

Furthermore, the impacts of noise on the reconstructed image $I(\mathbf{r_k})$ can be neglected. In other words, the proposed method can effectively suppress the noise interference.

III. EXPERIMENT AND DISCUSSION

To verify and investigate the performance of the proposed method, two experiments were taken. Firstly, a numerical experiment was taken to investigate the availability of sub-arrays' constitution. Then, a measured experiment was executed to prove the feasibility of the proposed method in the applications where few echo signals were used.

A. Numerical experiment

In this section, The Gaussian modulated pulse of 0.5-ns duration centered at 3.5 GHz, which is suitable for medium/long range search radars was chosen as detection pulse. A rectangle scatterer S1 modeled with 4 scattering points (-0.6m, 0.7m), (-0.55m, 0.7m), (-0.5m, 0.7m), (-0.45m, 0.7m) was chosen as an extended target, and a scatterer S2 modeled with one scattering point (0m, 0.45m) was employed as a point-like target, as shown in Fig. 1. It is worth mention that four transceivers were employed for simplicity. The specific positions of the transmitter and receiver of each transceiver are listed in Table 1. The standard noise is added to the echo signals.

Table 1: The specific locations of each transceiver in numerical experiment (unit: m)

	Transmitter's Location	Receiver's Location
Transceiver 1	X=-0.125, Y=0	X=-0.175, Y=0
Transceiver 2	X=-0.025, Y=0	X=-0.075, Y=0
Transceiver 3	X=0.075, Y=0	X=0.025, Y=0
Transceiver 4	X=0.175, Y=0	X=0.125, Y=0

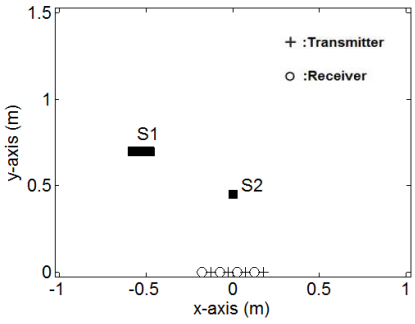

Fig. 1. Setup of the numerical experiment.

The sub-arrays are constituted in three ways, as shown in Table 2. In case 1, three sub-arrays are made, and each sub-array consists of two adjoining transceivers. In cases 2 and 3, two sub-arrays are got, and each sub-array consists of three adjoining transceivers in case 2, while there are two adjoining transceivers in case 3 whose total number of transceivers are three.

By using the proposed method, the results based on the aforementioned three cases are shown in Figs. 2 and 3. At SNR=0 dB, two targets can be distinguished obviously from all the detection maps. Precisely, the shapes and positions of this extended target and point-like target can be obtained, and there are hardly ghost images appearance in the detection maps. Moreover, compared with case 1 and case 2, although the imaging resolution of case 3 is a little declined, both the extended target and point-like target can be differentiated evidently, and these two targets are able to be detected easily. Investigate its germ, on the one hand, the increase of transceivers contained in each sub-array can improve the TR-focusing effort; on the other hand, according to Equation (9), the increase of sub-arrays can enhance the pixel value at target's location due to the superposition that reduces the influence of noise. Thus, cases 1 and 2 are able to remove the artifacts better, compared with case 3.

Furthermore, when the SNR drops to -10 dB, two targets including shapes and locations are still able to be distinguished in all cases by using the proposed algorithm. And also compared with cases 1 and 2, the imaging resolution decreases a little, the reason is the same as discussed above. Moreover, the target images are not influenced by noise, while the images created by the background are influenced by noise dramatically. Thus, this method can suppress noise effectively.

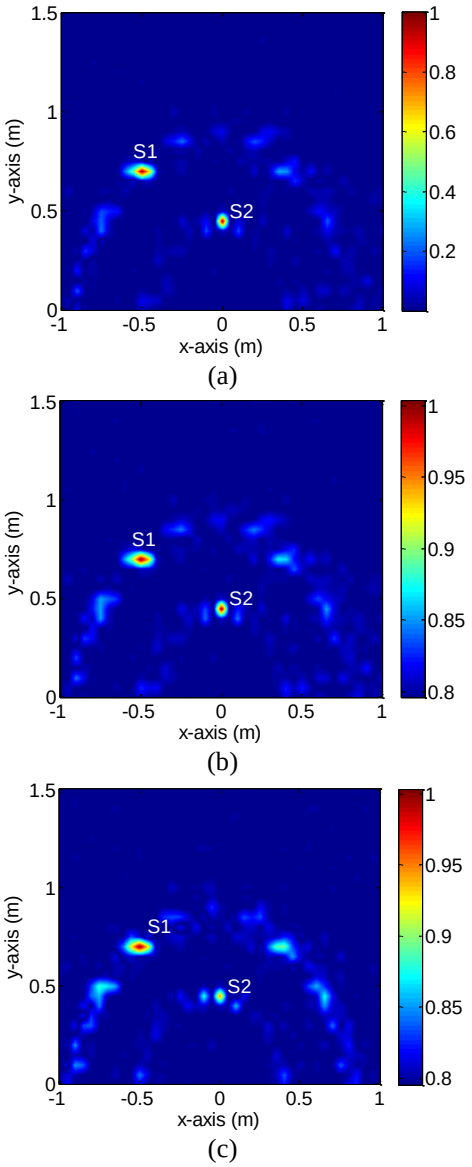

Fig. 2. Detection results based on various constitutions of the sub-arrays at SNR=0 dB: (a) Case 1, (b) Case 2, and (c) Case 3.

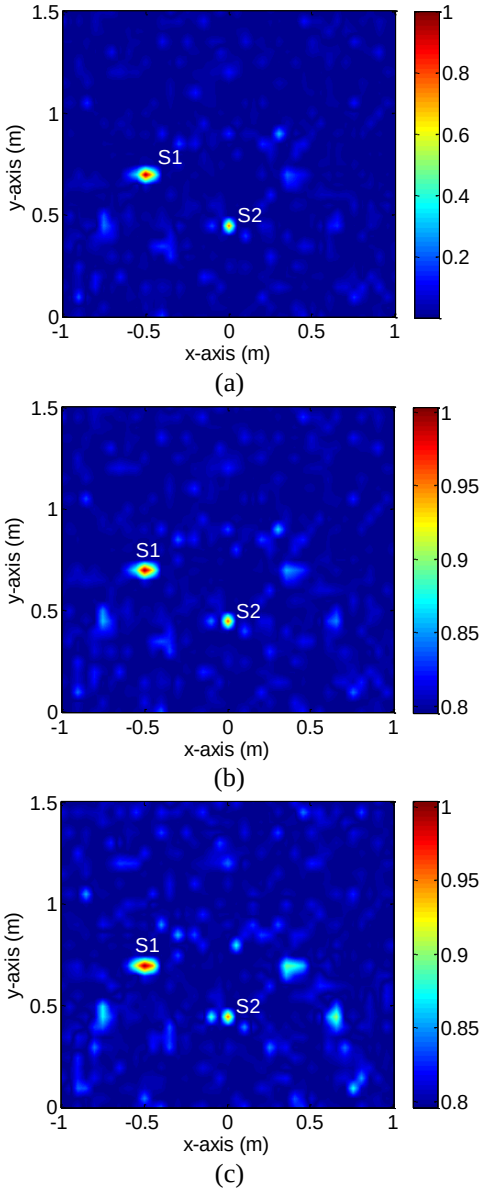

Fig. 3. Detection results based on various constitutions of the sub-arrays at SNR=-10 dB: (a) Case 1, (b) Case 2, and (c) Case 3.

Table 2: The constitution of the sub-arrays in numerical experiment

	Case 1	Case 2	Case 3
Sub-array 1	Transceiver 1 Transceiver 2	Transceiver 1 Transceiver 2 Transceiver 3	Transceiver 1 Transceiver 2
Sub-array 2	Transceiver 2 Transceiver 3	Transceiver 2 Transceiver 3 Transceiver 4	Transceiver 2 Transceiver 3
Sub-array 3	Transceiver 3 Transceiver 4		

B. Measured experiment

In this experiment, to evaluate the impact of using few echo signals on the performance of the proposed method, three transceivers were employed to obtain three echo signals. And these three transceivers are separated into two sub-arrays according to case 3 of Table 2.

The measured experimental setup is illustrated in Fig. 4, which is a 2-D construct. A cylinder metal pot whose diameter is 15cm was centered at (0m, 0.295m), and used as the scatterer. Three transceivers were used to detect the scatterer. Specific positions of the transmitting and receiving antennas of each transceiver are listed in Table 3. The Gaussian modulated pulse used in numerical experiment was also employed in this measured experiment.

Table 3: Specific positions of the transmitting and receiving antennas of each transceiver (unit: m)

Transceiver	Transmitting Antenna's Position	Receiving Antenna's Position
1	x=-0.125, y=0	x=-0.175, y=0
2	x=0.025, y=0	x=-0.025, y=0
3	x=0.175, y=0	x=0.125, y=0

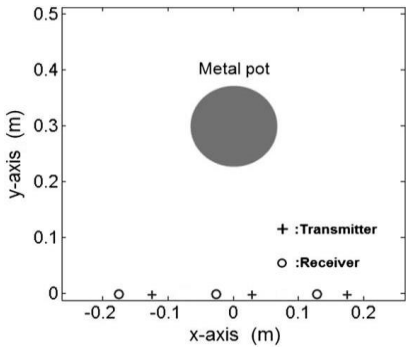

Fig. 4. Setup illustration of measured experiment.

The schematic diagram and the corresponding photo of the measured experimental are shown in Figs. 5 (a) and 5 (b). In each transceiver's location, the probing signal from a Tektronix AWG 7122B arbitrary waveform generator was amplified and used to drive a directional vivaldi antenna whose maximum direction of radiation is toward metal pot, and bandwidth is from 0.8 GHz to 8 GHz. The echo signal was received by an omnidirectional bow-tie antenna which has a bandwidth ranging from 2 to 12 GHz and recorded by Tektronix DSA 72004B.

I considered to process the echo signals in two cases, namely, the low-noise case and the high-noise case. In the low-noise case, the echo signals received by transceivers were processed directly. However, in the high-noise case, an extra noise was added to the realistic echo signals to achieve a SNR of -10 dB, where the SNR

was defined as the ratio between the amplitude of realistic echo signals and the standard deviation of the noise amplitude, and then the new signals were acquired. The results obtained by using the conventional TR algorithm and the proposed algorithm in the both cases are shown in Figs. 6 and 7, respectively.

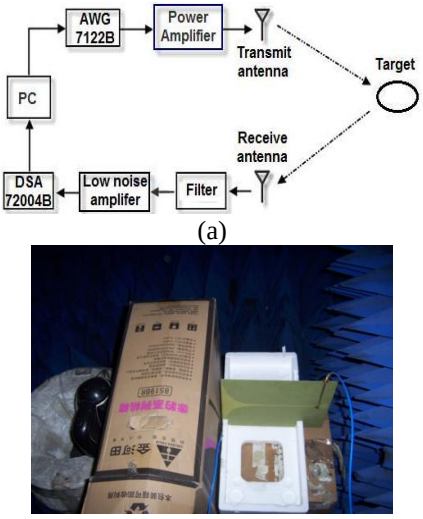

Fig. 5. Schematic diagram and photo of the measured experiment: (a) schematic diagram and (b) photo.

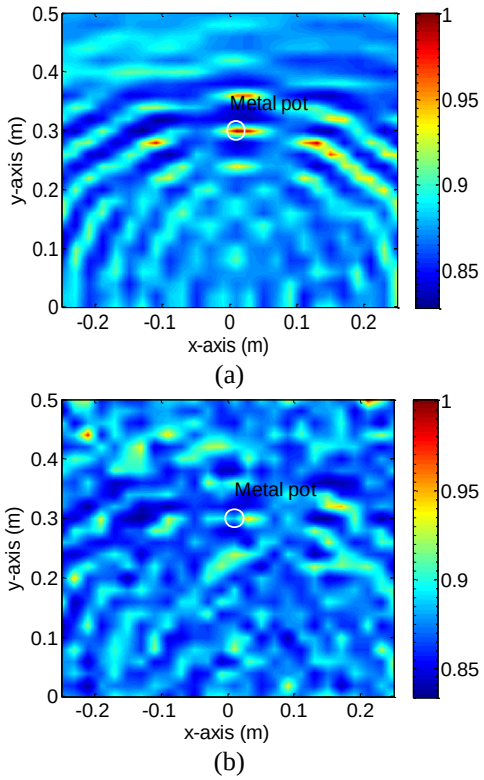

Fig. 6. Detection results by using the conventional TR in both cases: (a) low-noise and (b) high-noise.

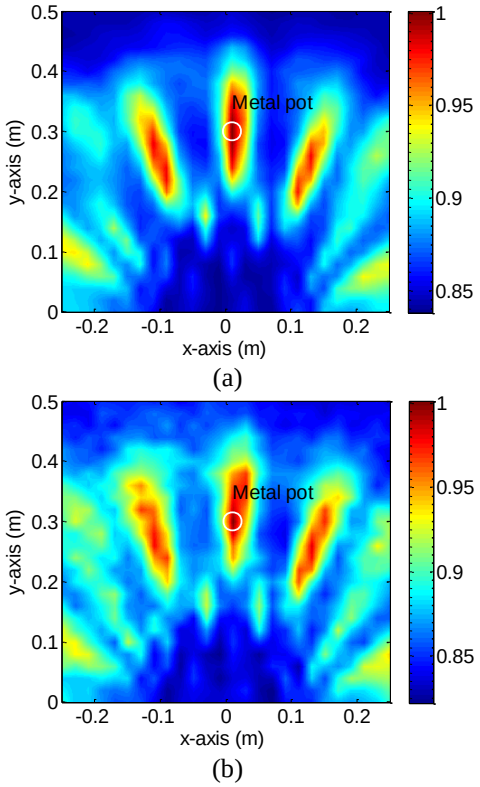

Fig. 7. Detection results by using the proposed algorithm in both cases: (a) low-noise and (b) high-noise.

Shown in Fig. 6 are detection results constructed by using the conventional TR algorithm. In low-noise case, the obtained image clearly reveals the correct target supports. The beneficial effect quickly disappeared, however, after adding noise. In high-noise case, the strong noise leads to several ghost images whose pixel values even exceed the pixel value in target's location. Clearly, Fig. 6 (b) is not an accurate reconstruction of the target's position. Such degradation performance is most likely a result of using few echo signals in the TR system.

Compared with Fig. 6, Fig. 7 can give a good idea of the scatterer's position in both situations. It can be seen that the detection maps based on the proposal method are not almost influenced by the enhancement of noise. Those mean the proposed algorithm outperforms the conventional TR method under few echo signals and strong noise interference conditions.

In order to facilitate comparison, the distributions of the maximum pixel values based on the two detection methods in both cases are able to be extracted from Fig. 6 and Fig. 7 and are also listed in Table 4. It can be found that the image peaks based on the proposal method appear at the same position that is the scatterer's location. In contrast, the conventional TR algorithm can point out the scatterer's location in the low-noise case, the maximum pixel value shifts to wrong position when noise enhances.

Table 4: The distributions of the maximum pixel values (unit: m)

	High-noise	Low-noise
The proposal algorithm	x=0.01,y=0.3	x=0.01,y=0.3
The conventional TR algorithm	x=0.21,y=0.5	x=0.01,y=0.3

In general, the decrease of the number of echo signals can weaken the TR-focusing effect, so that the peak of noise can exceed the peak of focusing signal under strong noise conditions. Therefore, the conventional TR algorithm which reconstructs the detection map by using the amplitude of TR signal at the focusing time, leads to a false image. However, since the proposal method utilizes the signal waveform similarity to reconstruct the detection map, the interference of strong noise is suppressed effectively. Thus, the target can be detected accurately by taking advantaging of the proposed method, even under the situation of strong noise.

Otherwise, the number of each sub-array's transceivers and the number of sub-arrays can be increased by adding employed transceivers. Both of them can improve the performance of the proposed method, as mentioned before. Therefore, the proposed method can work better when the number of employed transceivers are more than three. Additionally, TR-MUSIC and DORT cannot be applied in the experiment, since their MDM whose size is 3×3, cannot be constructed just by using 3 echo signals [5-8].

IV. CONCLUSIONS

In this paper, a novel TRD algorithm which uses the cross-correlation character of TR signals as the detection function is presented. Since the noise is irrelevant to TR-focusing signal, the proposal algorithm can effectively suppress the interference of noise, even in a situation where few echo signals are available. The result shows that the new method can utilize only three echo signals to distinguish the scatterer's location even under a SNR of -10 dB condition. Thus, compared with the conventional TR method, the proposed TRD algorithm is shown to be both practical and exploitable.

REFERENCES

[1] Y. Song, N. Guo, and R. C. Qiu, "Implementation of UWB MIMO time-reversal radio testbed," *IEEE Antennas Wireless Propag. Lett.*, vol. 10, pp. 796-799, 2011.

[2] B. B. Wang, Y. L. Wu, F. Han, et al., "Green wireless communications: a time-reversal paradigm," *IEEE J. Sel. Areas Commun*., vol. 29, pp. 1698-1710, 2011.

[3] S. Ding, B. Z. Wang, G. D. Ge, and D. S. Zhao, "Sub-wavelength array with embedded chirped delay lines based on time reversal technique," *IEEE Trans. Antennas Propag.*, vol. 61, pp. 2868-2873, 2013.

[4] X. F Liu, B. Z. Wang, S. Q. Xiao, and S. J. Lai, "Post-time-reversed MIMO ultrawideband transmission scheme," *IEEE Trans. Antennas Propag.*, vol. 58, pp. 1731-1738, 2010.

[5] Y. Labyed and L. J. Huang, "Super-resolution ultrasound imaging using a phase-coherent MUSIC method with compensation for the phase response of transducer elements," *IEEE Trans. Ultrason. Ferroelectr. Freq. Control.*, vol. 60, pp. 1048-1060, 2013.

[6] M. D. Hossain, A. S. Mohan, and M. J. Abedin, "Beamspace time-reversal microwave imaging for breast cancer detection," *IEEE Antennas Wireless Propag. Lett.*, vol. 12, pp. 241-244, 2013.

[7] Y. Labyed and L. J. Huang, "Ultrasound time-reversal MUSIC imaging with diffraction and attenuation compensation," *IEEE Trans. Ultrason. Ferroelectr. Freq. Control.*, vol. 59, pp. 2186-2200, 2012.

[8] X. F. Liu, B. Z. Wang, and J. L. Li, "Transmitting-mode time reversal imaging using MUSIC algorithm for surveillance in wireless sensor network," *IEEE Trans. Antennas Propag.*, vol. 60, pp. 220-230, 2012.

[9] T. J. Ulrich, M. Griffa, and B. E. Anderson, "Symmetry-based imaging condition in time reversed acoustics," *J. Appl. Phys.*, vol. 104, pp. 1-8, 2008.

[10] W. Liu and W. S. Lin, "Additive white Gaussian noise level estimation in SVD domain for images," *IEEE Trans. Image Process.*, vol. 22, no. 3, pp. 872-883, 2013.

[11] L. Borcea, G. Papanicolaou, and C. Tsogka, "Theory and applications of time reversal and interferometric imaging," *Inverse Prob*., vol. 19, pp. S139-S164, 2003.

A Compact Microstrip Lowpass Filter with Flat Group-delay and Ultra High Figure-of-Merit

M. Hayati [1,2], M. Ekhteraei [1], and F. Shama [1]

[1] Electrical Engineering Department
Kermanshah Branch, Islamic Azad University, Kermanshah, Iran
Mohsen_hayati@yahoo.com, m.ekhteraei.ir@ieee.org, f.shama@aut.ac.ir

[2] Electrical Engineering Department
Razi University, Tagh-E-Bostan, Kermanshah-67149, Iran

Abstract ─ This paper presents a new design of a microwave low pass filter (LPF) using coupled stepped impedance patches. The designed LPF has specifications such as ultra sharp roll-off, ultra wide stopband, low insertion-loss and high return-loss in the passband. The designed LPF has -3 dB cut-off frequency of 1.38 GHz. The transition-band is 0.12 GHz that is from 1.38 to 1.50 GHz with the attenuation levels of -3 and -20 dB, respectively. Maximum insertion-loss at about 80% of the passband is 0.1 dB. The simulation and experimental results are close to each other. The proposed LPF achieved to a remarkable figure-of-merit of 171622.

Index Terms ─ Bended structure, group delay, lowpass filter, microstrip.

I. INTRODUCTION

Within the development of modern communication technologies, demands for pure signals are increasing rapidly. So, in order to get pure signals, high performance LPFs have been widely used. Recently, many microstrip LPFs are realized by various structures. In [1], a structure consists of high-impedance meandered transmission lines loaded by triangular and polygonal resonant patches is presented. Although the filter has wide stopband but it has a low return-loss in the passband. An LPF consists of radial resonators is presented in [2]. The structure has a sharp roll-off and compact size but the stopband is not so wide. Dual-transmission line is suggested to design an LPF in [3]. The filter has sharp roll-off and high return-loss in the passband, but it has also poor specifications such as very large size and narrow stopband width. In [4], an LPF employs rat-race directional couplers properly arranged to operate as bandstop transversal filtering sections (TFSs) is presented, which has a sharp roll-off but also suffers from a large size. A compact LPF using a T-shaped patch and stepped impedance resonators with sharp roll-off is presented in [5]. But the value of return-loss in the passband is not high. An LPF structure which consists of a high impedance microstrip line (HIML) and a pair of radial stubs (RSs) loaded at its center and a pair of stepped impedance open stubs (SIOSs) loaded on both ends of HIML, is designed in [6]. Despite having a wide stopband and high return-loss, it has poor characteristics such as large size and gradual cut-off. In this paper, a compact microstrip lowpass filter using coupled stepped impedance patches with ultra wide stopband, remarkable roll-off rate and noticeable figure-of-merit (FOM) of 171,622 is designed.

II. DESIGN PROCEDURE

At the first step, the resonator is analyzed and the process of designing the resonator is represented step by step; at the second step, the suppressor is analyzed and designed as well.

A. Design and analysis of the resonator

The main idea in the resonator design contains to have a two resonator which occupies a one resonator area (each resonator creates a one transmission zero nearby the cut-off frequency and results in a sharp roll off). This case can be occurred using the bending technique, which allows the resonators to fold in each other, which results a compact size.

1) First resonator design

The LC circuit and layout of the prototype resonator are shown in Fig. 1. Based on the basic concepts and theories of microstrip filters, a short open circuited stub of a lossless microstrip line can be considered as a shunt capacitor and a similar short-circuited stub can be considered as a shunt inductor. The parameters of the transmission line of the prototype resonator as well as the physical lengths of the low and high impedance lines are obtained as follows [7]:

Submitted On: August 23, 2016
Accepted On: November 27, 2016

$$l_{Li} = \frac{\lambda_{g_{Li}}}{2\pi} \sin^{-1}\left(\frac{Z_0 \times g_i}{Z_{0L_i}}\right), \quad (1)$$

$$l_{Ci} = \frac{\lambda_{g_{Ci}}}{2\pi} \sin^{-1}\left(\frac{Z_{0C_i} \times g_i}{Z_0}\right), \quad (2)$$

where Z_{0C_i} and Z_{0L_i} represent the impedance transmission lines with low and high impedance, respectively, g_i is the element value of each part of the prototype layout, $\lambda_{g_{Li}}$ and $\lambda_{g_{Ci}}$ is the guided wavelength of high and low impedance lines, respectively.

A comparison of the S-parameters of LC model and layout of the prototype resonator is shown in Fig. 1. As shown, the frequency response has a low insertion loss in the passband, but the transition band is not sharp enough. Moreover, to achieve a lower cut-off frequency, in conventional type the size should be increased, which is not desired. Therefore, to improve the performance, bending technique is employed. Bending in designing microstrip structures is a technique for reducing the size of the filters [7].

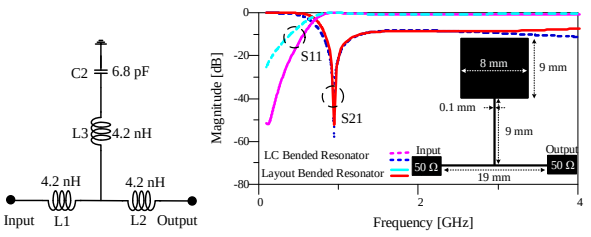

Fig. 1. The prototype resonator, the LC circuit, the layout and the simulated S-parameters.

The first bended resonator, its equivalent LC circuit and a comparison of the S-parameters of LC model and layout of the bended resonator are shown in Fig. 2 (a). In comparison with the structure shown in the Fig. 1, the size of the bended structure is more compact.

2) Second resonator design

By Similar procedure, another bended resonator is designed to have a new transmission zero nearby the previous one in first resonator; the LC model, layout of the second resonator and a comparison of the S-parameters of this resonator and its LC model are shown in Fig. 2 (b).

3) Combination of first and second resonator

With merging the first and second bended resonators, as shown in Fig. 2 (c) (with specifications of bended technique, the overall size of the resonator has not been increased), a sharper transition band can be achieved in order to have two transmission zeros nearby each other. The LC model and a comparison of the simulated S-parameters of the merged resonator and its LC model are illustrated in Fig. 2 (c). The merged resonator has two transmission zeros at 1.1 and 1.36 GHz, which creates a transition band of 0.26 GHz from -3 dB to -40 dB. But unfortunately, as highlighted in Fig. 4 (b), the insertion loss has a significant value in the passband.

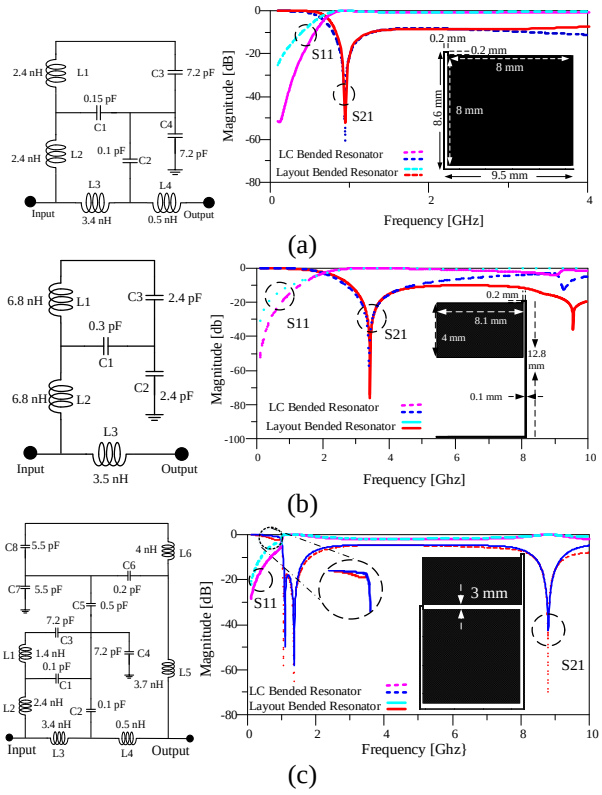

Fig. 2. The LC model, the layout and the simulated S-parameters: (a) the first bended resonator, (b) the second bended resonator, and (c) the merged resonator.

4) The proposed modified resonator

To achieve a better performance especially a low insertion loss, the structure of the merged resonator is modified by defecting the squired-shaped open stubs as shown in Fig. 3 (a). In this figure, the dimensions are indicated on this structure. The LC equivalent circuit is illustrated in Fig. 3 (b). The defection procedure not only results a better roll-off and higher return loss in the passband region, but also guarantee a small circuit area. Figure 3 (c) shows a comparison of the S-parameters of LC model and layout of the proposed modified resonator.

B. Design and analysis of the suppressor

To obtain an LPF with desired characteristics such as an ultra-wide rejection band, a modified radial patch cell (MRPC) is used as the suppressor. The LC model, layout of a prototype radial patch cell (RPC) and a comparison of the LC model and simulated S-parameters of this cell are shown in Fig. 4. As shown, this resonator cannot provide a wide rejection band, also the attenuation level is not sufficient in this region. To achieve wide rejection band and preferred attenuation level the

bending technique has been used to have a MRPC as shown in Fig. 5. The LC equivalent circuit of the MRPC and a comparison of the LC model and simulated S-parameters of MRPC are shown in Fig. 5.

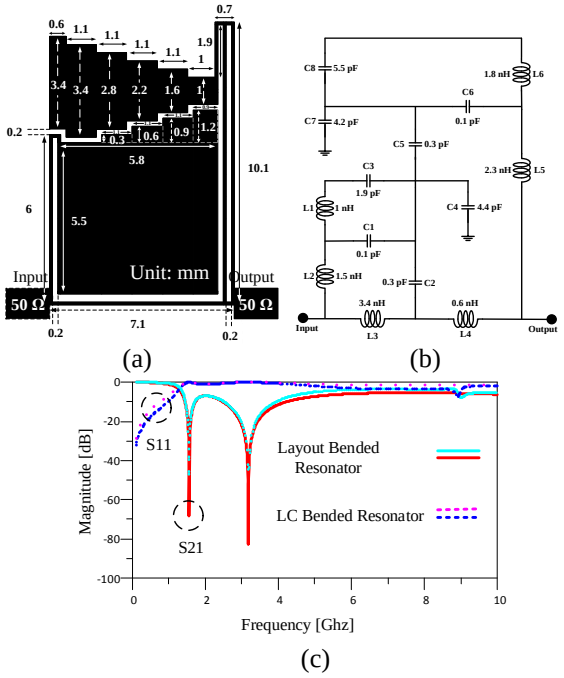

Fig. 3. The proposed modified resonator: (a) layout, (b) LC model, and (c) the simulated S-parameters.

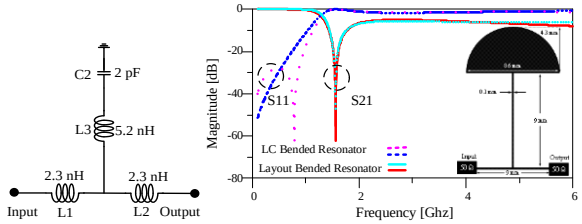

Fig. 4. A prototype RPC; the LC model, the layout and the simulated S-parameters.

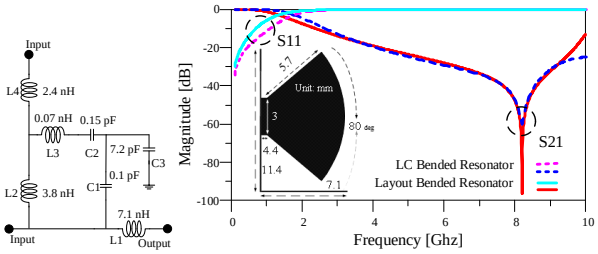

Fig. 5. A MRPC; the LC model, the layout and the simulated S-parameters.

As seen from this figure, the simulated S-parameters of this suppressor results in a wide stopband (4.2 to 9.7 GHz, with corresponding attenuation level of -20 dB), which is created by a transmission zero at 8.2 GHz with attenuation level of -96 dB. Also, the proposed MRPC occupies a smaller area than the conventional RPC.

III. LPF DESIGN

Merging the proposed modified resonator and MRPC, results in a primal LPF before loading a triangle-shaped microwave cell, which is shown in Fig. 6. From the simulated frequency response as illustrated in this figure, the filter has a very sharp transition band and wide stopband from 1.50 to 10 GHz with corresponding attenuation level of -20 dB, but the insertion loss in the passband is not low enough. Also, a wider rejection band is desired to have an ultra-wide stopband. So, by using the free spaces between the feeding lines and the radial open stub in the proposed MRPC, two stubs can be loaded to have a high performance LPF and without size increment.

Firstly, as indicated in Fig. 6, the free space between feeding lines and the upper side of MRPC is loaded by a triangle-shaped microstrip cell. As considered from this figure stopband region is dramatically suppressed from 1.50 to 18.8 GHz with corresponding attenuation level of -20 dB. Finally, the proposed LPF can be obtained as indicated in Fig. 7, which the free space below the MRPC has been loaded by a tapered microstrip cell.

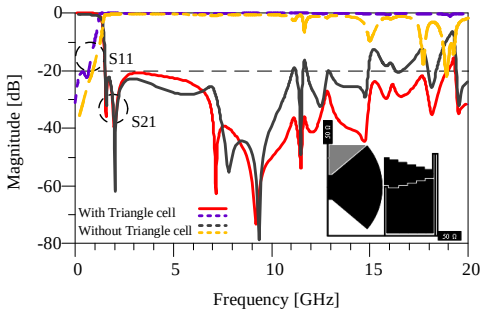

Fig. 6. Comparison between the simulated S-parameters of the layout and the triangle-shaped microwave cell before and after loading.

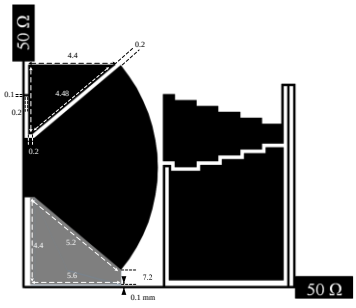

Fig. 7. The proposed LPF and the dimensions of triangle-shaped and tapered microstrip cell.

The dimensions of the loaded triangle-shaped and tapered microstrip cells to the proposed MRPC are shown in this figure.

IV. SIMULATION AND MEASUREMENT

The simulations are performed by ADS software and the measurements are carried out by an HP8757 Network Analyzer as shown in Fig. 8. As seen in Fig. 8, the final proposed filter is fabricated on the RT/Duriod 5880 substrate ($\varepsilon_r = 2.2$, thickness = 15 mil, loss tangent of 0.0009). As concluded from the final measurements, the LPF has -3 dB cut-off frequency at 1.38 GHz. The transition band is only 0.12 GHz. Maximum insertion loss is less than 0.08 dB in 78% and less than 0.2 dB in the 82% of the passband region. It has an ultra-wide stopband from 1.38 to 22.5 GHz with the attenuation level of -20 dB. The performance comparison of the proposed LPF within other published LPFs is summarized in Table 1. In this Table, the ξ is roll-off rate. RSB is the relative stop bandwidth and SF is the considered suppressing factor for the stopband. NCS is the normalized circuit size. AF is the architecture factor. Finally, FOM is the figure-of-merit for a LPF. All of these factors are defined in appendix section. As seen in Table 1, the proposed LPF has the highest FOM (171,622) among the referred LPFs.

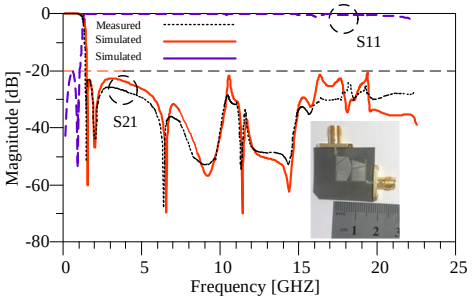

Fig. 8. The Simulated and measured S-parameters of the final proposed LPF and photograph of the proposed LPF.

A flat group delay for an LPF is desirable in the passband region [7]. As seen in Fig. 9, the maximum variation of the measured group delay in the passband is a dispensable value of 0.212 ns. The measured group delay can be determined using cure fitting as exponential functions as shown in Fig. 9. So the group delay equation can be written as bellows:

$$Group\ delay\ (s) = ae^{bf} + ce^{df}. \quad (3)$$

The group delay is considered using below equation:

$$Group\ delay\ (s) = -\frac{d\varphi}{d\omega}, \quad (4)$$

where φ is the total phase shift in radians (in this case from the parameter of S21), and ω is the angular frequency in radians per unit time, equal to $2\pi f$, where f is the frequency in hertz. From Equations (1-2) and with considering $= 2\pi f$:

$$-\frac{1}{2\pi}\frac{d\varphi}{df} = ae^{bf} + ce^{df}, \quad (5)$$

$$\int d\varphi = -2\pi \int_{0.1GHz}^{1GHz} (ae^{bf} + ce^{df})df, \quad (6)$$

$$\varphi(S_{21})|_{0.1GHz}^{1GHz} = -2\pi\left({}^{a}/_{b}\, e^{bf} + {}^{c}/_{d}\, e^{df}\right). \quad (7)$$

As shown in Fig. 10, the calculated phase of S21 parameter is illustrated in comparison with the simulated one using ADS software. As seen, it is good agreement between the measurements and simulations in this case.

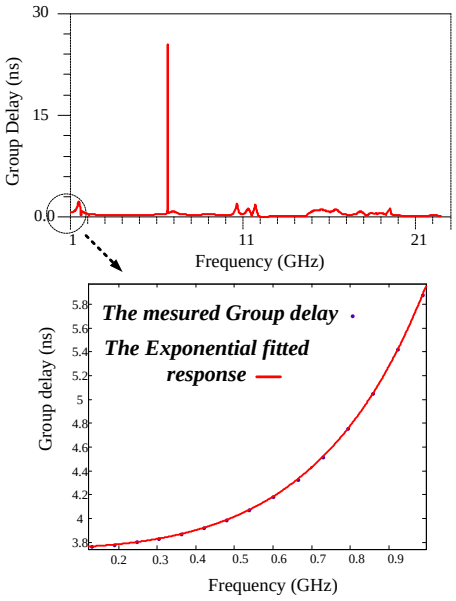

Fig. 9. The group delay in the passband for the proposed LPF.

Table 1: Comparison between the characteristics of the proposed LPF and other similar types

Ref.	f_c (GHz)	ζ	NCS	RSB	R-L (dB)	SF	AF	FOM
[1]	2.44	178.9	0.0232	1.73	12	2	1	26912
[2]	4.24	130.7	0.014	1.26	20	2	1	23526
[5]	4	425	0.0551	1.30	15.2	2	1	78928
[6]	1.07	56.67	0.0089	1.70	20	2	1	21649
[7]	1.11	58.62	0.0088	1.54	18.2	2	1	20495
[8]	1.5	81	0.017	1.72	20	2	1	16400
[9]	3.2	5.28	0.0075	1.66	16	2	1	1160
[10]	0.85	18	0.0072	1.73	17	1.5	1	6479
[11]	2	43.9	0.015	1.63	10	1	1	4771
[12]	2.4	92.5	0.037	1.35	11	3	1	10106
[13]	1.67	21.2	0.0064	1.49	12	1	1	4936
[14]	1.65	57.8	0.012	1.61	12	3.5	1	27142
[15]	1.18	36.3	0.0061	1.32	32	1.5	1	11543
[16]	3.6	370	0.01496	0.98	16	2	1	49672
This Work	1.38	324.25	0.0058	1.74	20	2	1	171622

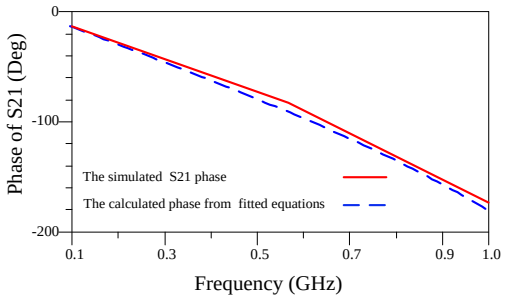

Fig. 10. The phase of S21 parameter.

V. CONCLUSION

A microstrip LPF with sharp transition band and ultra-wide stopband has been presented. By applying bended structures, without increasing the size, the cut-off frequency has been decreased. The filter passes frequencies through L-band range and highly suppresses in the higher ranges. The fabricated LPF with flat group delay in the passband can be expected to use in microwave circuits for suppressing the unwanted harmonics and signals.

ACKNOWLEDGEMENT

The authors would like to thank the Kermanshah Branch, Islamic Azad University for the financial support of this research project.

APPENDIX

In Table 1, the roll of rate (ζ) is used to evaluate the sharpness which is defined as [7]:

$$\zeta = \frac{\alpha\, max - \alpha min}{f_s - f_c} \quad (dB/GHz), \tag{8}$$

where α_{max} is the 20 (or 40 dB) attenuation point, α_{min} is the 3 dB attenuation point; f_s is the 20 dB stopband frequency; and f_c is the 3 dB cut-off frequency. The relative stopband bandwidth (RSB) is given by [7]:

$$RSB = \frac{stopbband\ bandwidth}{stopband\ center\ frequency}. \tag{9}$$

The suppression factor (SF) is based on the stopband suppression. A higher suppression degree in the stopband leads to a greater SF. For instance, if the stopband bandwidth is calculated under 20 dB restriction, then the SF is considered as 2. The normalized circuit size (NCS) is given by [7]:

$$NCS = \frac{phisical\ size\ (length*Width)}{\lambda_{g^2}}. \tag{10}$$

This is applied to measure the degree of miniaturization of diverse filters, where λ_g is the guided wavelength at 3 dB cut-off frequency, the architecture factor (AF) can be recognized as the circuit complexity factor which is signed as 1 when the design is 2D and 2 when the design is 3D. Finally, the figure of merit (FOM) is defined as [7]:

$$FOM = \frac{\zeta * RSB * SF}{NCS * AF}. \tag{11}$$

REFERENCES

[1] M. Hayati and A. Abdipour, "Compact microstrip lowpass filter with sharp roll-off and ultra-wide stopband," *Electronics Letters*, vol. 49, no. 18, pp. 1159-1160, Aug. 2013.

[2] M. Hayati, S. Naderi, and F. Jafari, "Compact microstrip lowpass filter with sharp roll-off using radial resonator," *Electronics Letters*, vol. 50, no. 10, pp. 761-2, May 2014.

[3] V. K. Velidi and S. Sanyal, "Dual-transmission-line microstrip equiripple lowpass filter with sharp roll-off," *ETRI Journal*, vol. 33, no. 6, pp. 985-8, Dec. 2011.

[4] G. R. Gómez, M. A. Sánchez-Soriano, M. Sánchez-Renedo, G, Torregrosa-Penalva and E. Bronchalo, "Extended-stopband microstrip lowpass filter using rat-race directional couplers," *Electronics Letters*, vol. 49, no. 4, pp. 272-4, Feb. 2013.

[5] M. Hayati and A. Sheikhi, "Microstrip lowpass filter with very sharp transition band using T-shaped, patch, and stepped impedance resonators," *ETRI Journal*, vol. 35, no. 3, pp. 538-41, June 2013.

[6] J. Xu, Y. X. Ji, W. Wu, and C. Miao, "Design of miniaturized microstrip LPF and wideband BPF with ultra-wide stopband," *IEEE Microwave and Wireless Components Letters*, vol. 23, no. 8, pp. 397-9, Aug. 2013.

[7] M. Hayati, F. Shama, and H. Abbasi, "Compact microstrip lowpass filter with wide stopband and sharp roll-off using tapered resonator," *International Journal of Electronics*, vol. 100, no. 12, pp. 1751-9, Dec. 2013.

[8] M. Hayati, H. Abbasi, and F. Shama, "Microstrip lowpass filter with ultrawide stopband and sharp roll-off," *Arabian Journal for Science and Engineering*, vol. 39, no. 8 pp. 6249-53, Aug. 2014.

[9] K. Ma, K. S. Yeo, and W. M. Lim, "Ultra-wide rejection band lowpass cell," *Electronics Letters*, vol. 48, no. 2, pp. 99-100, Jan. 2012.

[10] J. Wang, H. Cui, and G. Zhang, "Design of compact microstrip lowpass filter with ultra-wide stopband," *Electronics Letters*, vol. 48, no. 14, pp. 854-6, July 2012.

[11] F. Wei, L. Chen, and X. W. Shi, "Compact lowpass filter based on coupled-line hairpin unit," *Electronics Letters*, vol. 48, no. 7, pp. 379-381, Mar. 2012.

[12] J. L. Li, S. W. Qu, and Q. Xue, "Compact microstrip lowpass filter with sharp roll-off and wide stop-band," *Electronics Letters*, vol. 45, no. 2, pp. 110-1, Jan. 2009.

[13] X. B. Wei, P. Wang, M. Q. Liu, and Y. Shi, "Compact wide-stopband lowpass filter using stepped impedance hairpin resonator with radial

stubs," *Electronics Letters*, vol. 47, no. 15, July 2011.
[14] B. Zhang, S. Li, and J. Huang, "Compact lowpass filter with wide stopband using coupled rhombic stubs," *Electronics Letters*, vol. 51, no. 3, pp. 264-6, Jan. 2015.
[15] J. Wang, L. Xu, J. S. Zhao, Y. X. Guo, and W. Wu, "Compact quasi-elliptic microstrip lowpass filter with wide stopband," *Electronics Letters*, vol. 46, no. 20, pp. 1384-1385, Jan. 2015.
[16] M. Hayati, S. Roshani, S. Roshani, and F. Shama, "A novel miniaturized Wilkinson power divider with n th harmonic suppression," *Journal of Electromagnetic Waves and Applications*, vol. 27, no. 6, pp. 726-735, Apr. 2013.

Mohsen Hayati is currently a Professor in Electrical Engineering Department, Razi University, Kermanshah, Iran. He has authored or co-authored over 185 papers published in international, domestic journals and conference proceedings. His current research interests include microwave and millimeter-wave devices and circuits, application of computational intelligence, artificial neural networks, fuzzy systems, neuro fuzzy systems, electronic circuit synthesis, and modeling and simulations.

Milad Ekhteraei is currently working toward the Ph.D. degree in Electrical Engineering in Azad University, Kermanshah, Iran. His research interests include design and analysis of the microstrip filters, and antennas.

Farzin Shama is currently a Assistant Professor in the Electrical Engineering Department, Azad University, Kermanshah Branch, Iran. His research interests include the microwave engineering, passive and active circuits design. He has published more than 40 papers in international and domestic journals and conferences. He was proud to achieve Superior Researcher in the Engineering Faculty of Razi University, in 2011 and 2012. He has been selected as Top Student of Iran, awarded by First Vice President of Iran in 2015.

Compact Wideband Parallel-Coupled Microstrip Line Bandpass Filter with In-Line Structure

Chuan Shao [1], Yang Li [1], Liang Wang [1], and Chen Jin [2]

[1] School of Electronics and Information
Jiangsu Vocational College of Business, 48 Jiangtong Road, Nantong, Jiangsu Province, P. R. China
ch_shao@126.com

[2] Xinglin College
Nantong University, 9 Seyuan Road, Nantong, 226019, Jiangsu Province, P. R. China
jc_uu@126.com

Abstract ─ A compact wideband microstrip bandpass filter constructed by a parallel-coupled microstrip line and a parallel-connected half-wavelength ($\lambda_g/2$) microstrip line is proposed in this letter. The proposed bandpass filter showcases wideband bandpass response with four transmission zeros within the operating bandwidth from DC to $2f_0$ (f_0 center frequency). The transmission zeros located at DC and $2f_0$ are inherently generated by the parallel-coupled microstrip line while the other two are realized by the parallel-connected $\lambda_g/2$ microstrip line. For validation, a wideband bandpass filter centered at 4.15 GHz with bandwidth of 3 GHz is designed, fabricated and measured. The size of the in-line bandpass filter is $0.27\lambda_g \times 0.045\lambda_g$, which features very compact size and can be integrated conveniently with other microwave components.

Index Terms ─ In-line structure, parallel-coupled microstrip line, transmission zero, wideband filter.

I. INTRODUCTION

Compact microwave wideband microstrip line bandpass filters are the most widely used filter structures, as they can be integrated with other passive or active microwave components conveniently, benefitting from the advantages of planar structure, easy fabrication and low cost. The parallel-coupled microstrip line (PCML) has been widely employed in the design of multistage bandpass filters [1-9]. Nevertheless, the conventional PCML filters may suffer from several disadvantages. One major disadvantage is that the occupied sizes of this kind of filters are too large, especially when the filter order becomes high to achieve good selectivity for the filter or other multi-functional microwave device [10]. Another disadvantage is that the first spurious passband of this type of bandpass filter appears at twice of the fundamental ($2f_0$), which is resulted from the unequal even and odd-mode phase velocities. These advantages may be the main limitation for the application of this type of filters.

In order to expand the application range for the PCML bandpass filters, several approaches have been adopted accordingly. In [1-2], meandered PCMLs and capacitive termination have been employed respectively to achieve size minimization. By taking these measures in [1-2], the reported PCML filters can achieve at least 25% size minimization compared with the conventional PCML filters of same order and specification. To reject the second harmonic response at $2f_0$, several methods have been reported [3-6]. In [3], the re-entrant coupling structure was applied in the design of parallel-coupled microstrip bandpass filter to realize a wide bandwidth and the suppression of spurious [3]. A certain height of substrate suspension [4] and grooved substrate [5] were used to equalize the even- and odd-mode phase velocities, and the second harmonic response can be rejected accordingly. In [6-9], defected ground structure (DGS) has been reported in designing microwave filter for rejecting spurious responses. However, filters employed DGS have etched patterns in the ground plane, which will cause a problem for package and lowering the reliability of the microwave systems.

In this letter, a compact wideband bandpass filter realized by PCML and a parallel-connected half-wavelength ($\lambda_g/2$) microstrip line is proposed. The PCML is used to provide wideband bandpass response while the $\lambda_g/2$ microstrip line is employed to generate two more transmission zeros and enhance the bandwidth of the proposed bandpass filter. In order to adjust the bandwidth of the filter for different kind of practical applications, the $\lambda_g/2$ microstrip line has been folded to form a parallel-connected coupled line. And the bandwidth of the bandpass filter can be shifted by changing the coupling coefficient of the parallel-connected coupled line. In addition, as the parallel-connected coupled line was compact, and it could be placed into the 50Ω

Submitted On: September 18, 2016
Accepted On: December 24, 2016

microstrip line and a wideband bandpass filter with in-line structure was realized. Owing to this in-line structure, the size of the bandpass filter is only 12mm×1.9mm, which corresponds to $0.27\lambda_g \times 0.045\lambda_g$ in electrical size.

II. ANALYSIS OF THE PARALLEL-COUPLED MICROSTRIP BANDPASS FILTER

The ideal circuit for the traditional PCML is shown in Fig. 1. In this figure, Z_{oe} and Z_{oo} are the even-mode and odd-mode characteristic impedances of the PCML and θ is the electrical length. The ideal responses for the circuit under different coupling coefficient K (K=(Z_{oe}-Z_{oo})/(Z_{oe}+Z_{oo})) in Fig. 1 are presented in Fig. 2. As we may see from this figure, the transmission poles will move away from the center frequency f_0 as the coupling coefficient K of the PCML increases. Therefore, the bandwidth of this structure can be controlled accordingly. There is a pair of transmission zeros located at DC and $2f_0$ within the operating bandwidth, however, the selectivity of the bandpass filter is not good enough. Therefore, a parallel-connected half-wavelength (λ_g/2) microstrip line is added to generate another two transmission zeros.

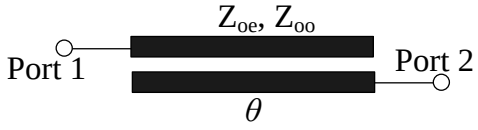

Fig. 1. Ideal circuit for the PCML.

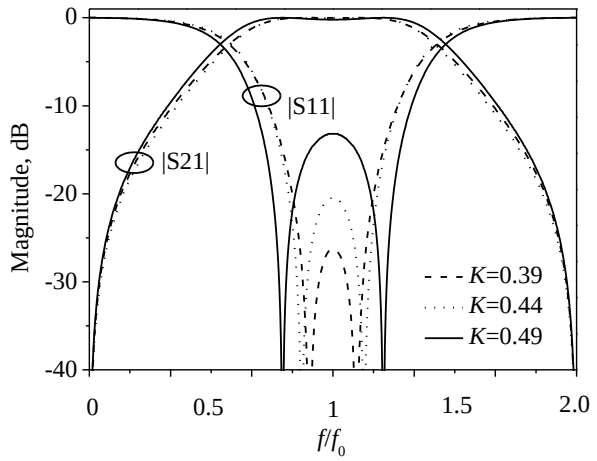

Fig. 2. Simulated responses for the traditional PCML under different coupling coefficient K.

A. Analysis of the transmission zeros

The ideal circuit for the proposed parallel-coupled filter with a parallel-connected λ_g/2 microstrip line is presented in Fig. 3. The ideal responses for the circuits in Fig. 1 and Fig. 3 are compared and plotted in Fig .4. According to Fig. 4, a pair of transmission has been added for the proposed wideband bandpass filter.

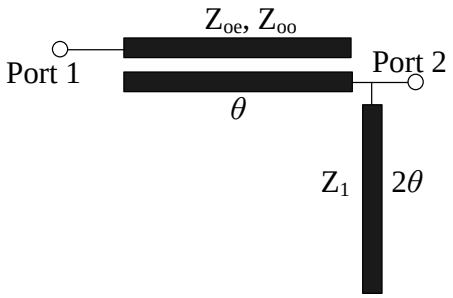

Fig. 3. Proposed PCML filter with a parallel-connected λ_g/2 microstrip line.

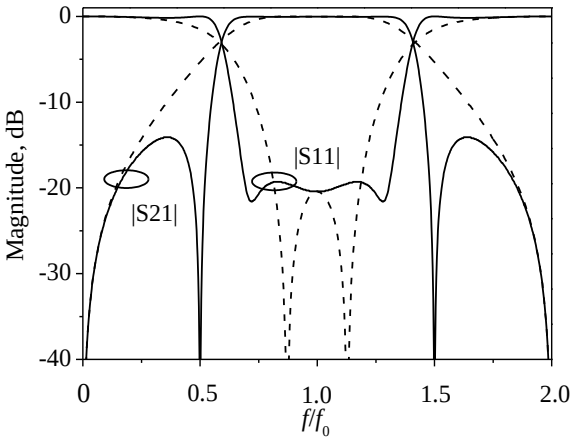

Fig. 4. Simulated responses for the circuits in Fig. 1 and Fig. 3 (Z_{oe}=180Ω, Z_{oo}=70Ω, Z_1=100Ω).

The *ABCD* matrices of the PCML and the parallel-connected λ_g/2 microstrip line are given as [11]:

$$M_p = \begin{bmatrix} A_p & B_p \\ C_p & D_p \end{bmatrix} = \begin{bmatrix} \frac{Z_{oe}+Z_{oo}}{Z_{oe}-Z_{oo}}\cos\theta & j\frac{(Z_{oe}-Z_{oo})^2-(Z_{oe}+Z_{oo})^2\cos^2\theta}{2(Z_{oe}+Z_{oo})\sin\theta} \\ j\frac{2\sin\theta}{Z_{oe}-Z_{oo}} & \frac{Z_{oe}+Z_{oo}}{Z_{oe}-Z_{oo}}\cos\theta \end{bmatrix}, \quad (1)$$

$$M_s = \begin{bmatrix} A_s & B_s \\ C_s & D_s \end{bmatrix} = \begin{bmatrix} 1 & 0 \\ j\frac{\tan 2\theta}{Z_1} & 1 \end{bmatrix}. \quad (2)$$

For the proposed bandpass filter, the *ABCD* matrices is $M_p \times M_s$, then the *S*-parameters of the wideband bandpass filter can be illustrated as [12]:

$$S_{11} = \frac{A + B/Z_0 - CZ_0 - D}{A + B/Z_0 + CZ_0 + D}, \quad (3)$$

$$S_{21} = \frac{2}{A + B/Z_0 + CZ_0 + D}. \quad (4)$$

When S_{21}=0, two transmission zeroes can be obtained as:

$$\theta_{z1} = \pi/4, \quad (5)$$

$$\theta_{z2} = 3\pi/4. \quad (6)$$

Moreover, three transmission poles reflect that S_{11}=0 has three real solutions when the values of Z_{oe}, Z_{oo} and Z_1 are properly selected.

B. Analysis of the parallel-connected $\lambda_g/2$ microstrip line

In Fig. 5, simulated transmission coefficient for the proposed bandpass filter versus Z_1 is presented. Bandwidth of the proposed bandpass filter will increase when the value of Z_1 decreases. Nevertheless, the out-of-band rejection level becomes bad while the bandwidth increases. Therefore, large value of Z_1 has been adopted in this design. In order to adjust the bandwidth even further, the parallel- parallel-connected half-wavelength ($\lambda_g/2$) microstrip line has been folded to form a parallel-connected coupled line as depicted in Fig. 6. The bandwidth of the proposed bandpass filter can be adjusted by changing the coupling coefficient K_1 (K_1=(Z_{oe1}-Z_{oo1})/(Z_{oe1}+Z_{oo1})) of the parallel-connected coupled line, as shown in Fig. 7.

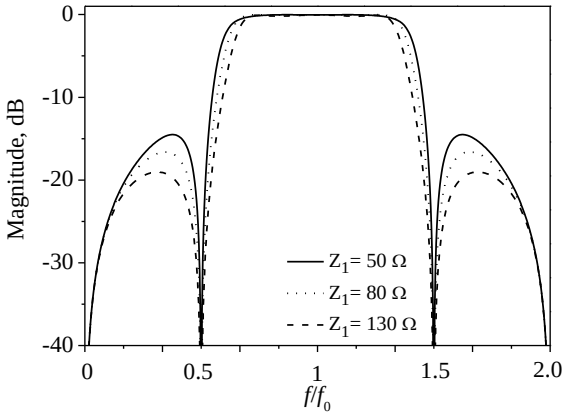

Fig. 5. Simulated transmission coefficients for the circuit in Fig. 3 versus Z_1 (Z_{oe}=180Ω, Z_{oo}=70Ω).

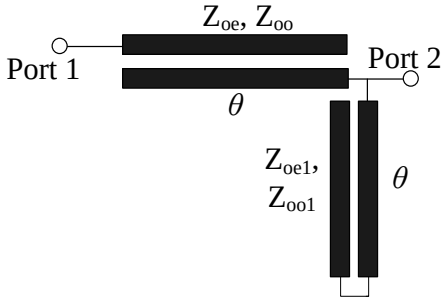

Fig. 6. Ideal circuit for the proposed PCML filter with a parallel-connected coupled line.

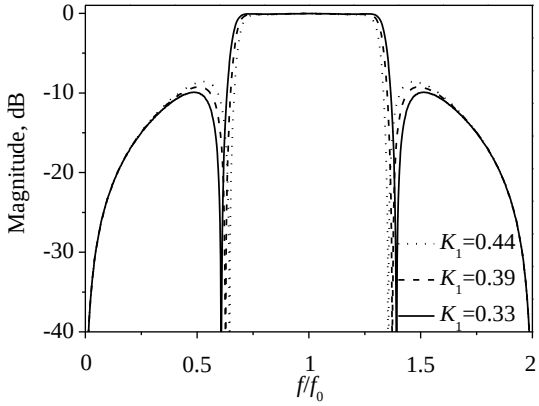

Fig. 7. Simulated transmission coefficients for the circuit in Fig. 6 versus K_1 (Z_{oe}=180Ω, Z_{oo}=70Ω).

III. FILTER DESIGN AND RESULTS

Based on the analysis given above, the final parameters for the circuit in Fig. 6 are obtained as follows: Z_{oe}=180Ω, Z_{oo}=70Ω, Z_{oe1}=160Ω, Z_{oo1}=80Ω, f_0=4.15 GHz, θ=90°. One prototype of the proposed PCML bandpass filter is fabricated on a RO4003c substrate with ε_r = 3.55, h = 32mil, and tanδ = 0.0027. The layout of the filter and the photograph of the fabricated filter are shown in Fig. 8, while the ideal, simulated and measured S-parameters and group delay are depicted in Fig. 9.

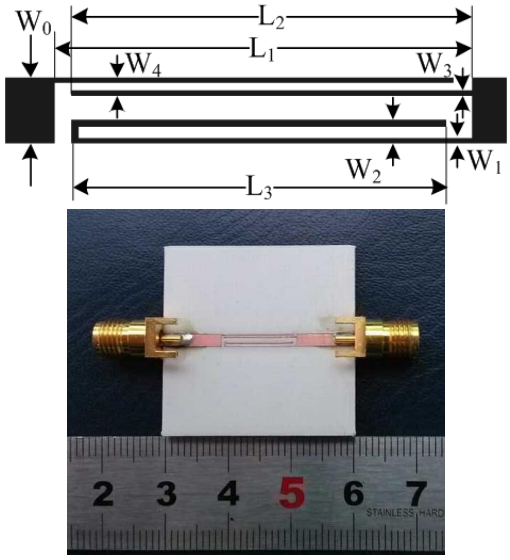

Fig. 8. Layout and photography of the fabricated in-line bandpass filter (L_1=12mm, L_2=11.5mm, L_3=11mm, W_0=1.9mm, W_1=0.2 mm, W_2=0.8mm, W_3=0.15mm, W_4=0.5mm).

As can be seen from Fig. 9, the results match with each other very well. The proposed wideband bandpass filter is centered at 4.15 GHz with 3-dB bandwidth of

3 GHz, which corresponds to 72.3% fractional bandwidth. Two transmission zeros generated by parallel-connected coupled line are located at 2.5 GHz and 5.8 GHz, which have greatly improved the selectivity of the bandpass filter. The minimum insertion loss is less than 0.55 dB while the return loss is over 10 dB within the passband. The ideal, simulated and measured group delay of this wideband bandpass filter are flat and less than 0.50 ns across the entire passband. As a result of the in-line structure, the total size of the proposed bandpass filter is $0.27\lambda_g \times 0.045\lambda_g$.

To further demonstrate the performance of the proposed bandpass filter, comparison between the proposed bandpass filter in this letter and previously reported filter structures are listed in Table 1. As can be seen from Table 1, the insertion loss of the proposed bandpass filter is much lower than most of the reported structures. Besides, the proposed bandpass filter is free of the spurious passband at $2f_0$ and possesses the most compact size.

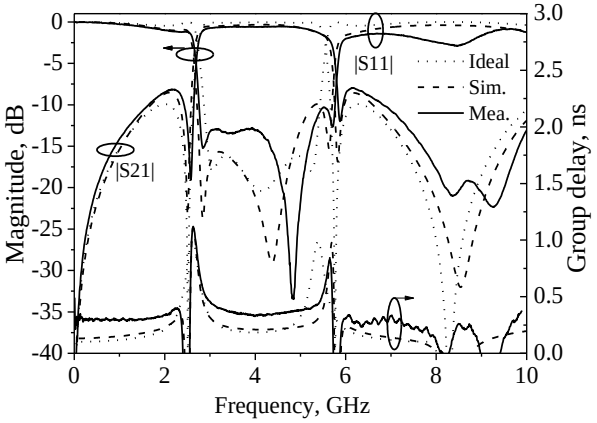

Fig. 9. Ideal, simulated and measured S-parameters and group delay of the proposed bandpass filter.

Table 1: Performance comparison with previously reported PCML filters

Ref.	f_0 (GHz)	3-dB Bandwidth	Insertion Loss (dB)	Transmission Zeros (DC to $2f_0$)	First Spurious Passband	Size ($\lambda_g \times \lambda_g$)
[1]	1.0	50%	NA	3	$>2f_0$	0.19×0.14
[2]	0.9	10%	1.0	2	$>3f_0$	0.8×0.06
[3]	5.0	70%	0.9	3	$>2f_0$	0.88×0.31
[4]	2.45	10%	NA	2	$3f_0$	1.33×0.17
[5]	1	20%	2	2	$3f_0$	NA
[6]	3	10%	1.0	3	$>2f_0$	NA
This work	4.15	>70%	0.53	4	$3f_0$	0.27×0.045

Where λ_g is the guided wavelength at the center frequency of the bandpass filters.

IV. CONCLUSION

In this letter, a compact PCML bandpass filter with in-line structure has been presented. Based on the traditional PCML, a parallel-connected half-wavelength ($\lambda_g/2$) microstrip line was added to realize two extra transmission zeroes, which have not only improved the selectivity of the filter but also enhanced the bandwidth. In addition, the parallel-connected $\lambda_g/2$ was folded and placed into the 50Ω microstrip line forming an in-line bandpass filter while the bandwidth of the filter can be tuned by changing the coupling coefficient of the parallel-connected coupled line. Compact size and good selectivity are realized for this wideband bandpass filter, which indicates a good candidate for modern wideband microwave communication applications.

ACKNOWLEDGMENT

The work was supported by the Nantong Science and Technology Project under Grants No. GY12015037.

REFERENCES

[1] S.-M. Wang, C.-H. Chi, M.-Y. Hsieh, and C.-Y. Chang, "Miniaturized spurious passband suppression microstrip filter using meandered parallel coupled lines," *IEEE Trans. Microw. Theory Tech.*, vol. 53, no. 2, pp. 747-753, Feb. 2005.

[2] P. Cheong, S.-W. Fok, and K.-W. Tam, "Miniaturized parallel coupled-line bandpass filter with spurious-response suppression," *IEEE Trans. Microw. Theory Tech.*, vol. 53, no. 5, pp. 1810-1815, May 2005.

[3] K.-S. Chin, Y.-P. Chen, K.-M. Lin, and Y.-C. Chiang, "Compact parallel coupled-line bandpass filter with wide bandwidth and suppression of spurious," *Microwave Opt. Technol. Lett.*, vol. 51, no. 8, pp. 1795-1800, Aug. 2009.

[4] J.-T. Kuo, M. Jiang, and H.-J. Chang, "Design of parallel-coupled microstrip filters with suppression

of spurious resonances using substrate suspension," *IEEE Trans. Microw. Theory Tech.*, vol. 52, no. 1, pp. 83-89, Jan. 2004.

[5] M. Moradian and M. Tayarani, "Spurious-response suppression in microstrip parallel-coupled bandpass filters by grooved substrates," *IEEE Trans. Microw. Theory Tech.*, vol. 56, no. 7, pp. 1707-1713, July 2008.

[6] J.-S. Park, J.-S. Yun, and D. Ahn, "A design of the novel coupled-line bandpass filter using defected ground structure with wide stopband performance," *IEEE Trans. Microw. Theory Tech.*, vol. 50, no. 9, pp. 2037-2043, Sep. 2002.

[7] F. Karshenas, A. R. Mallahzadeh, and J. Rashed-Mohassel, "Size reduction and harmonic suppression of parallel coupled line bandpass filters using defected ground structure," *Applied Computational Electromagnetics Society (ACES) Journal*, vol. 25, no. 2, pp. 149-155, Feb. 2010.

[8] Y. Li, H.-C. Yang, Y.-W. Wang, and S.-Q. Xiao, "Ultra-wideband bandpass filter based on parallel-coupled microstrip lines and defected ground structure," *Applied Computational Electromagnetics Society (ACES) Journal*, vol. 28, no. 1, pp. 21-26, Jan. 2013.

[9] M. N. Moghadasi, "Harmonic suppression of parallel coupled-line bandpass filters using defected microstrip structure," *Applied Computational Electromagnetics Society (ACES) Journal*, vol. 31, no. 5, pp. 568-573, May 2016.

[10] P.-H. Deng and L.-C. Dai, "Unequal Wilkinson power dividers with favorable selectivity and high-isolation using coupled-line filter transformers," *IEEE Trans. Microw. Theory Tech.*, vol. 60, no. 6, pp. 1810-1815, June 2012.

[11] G. L. Matthaei, L. Young, and E. M. T. Jones, *Microwave Filters, Impedance-Matching Networks, and Coupling Structures*. Dedham, MA: Artech House, 1980.

[12] D. M. Pozar, *Microwave Engineering*. 4th ed., New York: Wiley, 2012.

Chuan Shao was born in Tengzhou Shandong Province, China in 1988. He received B.E. and M.S. degree in Nantong University, Jiangsu Province, China, in 2012 and 2015 respectively. His research interests include microwave passive components, etc.

Shao is Reviewer of ACES Journal and International Journal of Microwave and Wireless Technologies.

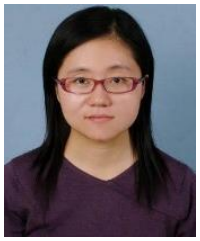

Yang Li was born in Yichang Hubei Province, China in 1980. She received B.E. degree in Central China Normal University, Hubei Province, China, in 2002. She received M.S. and Ph.D degree in Hefei University of Technology, Anhui Province, China, in 2007 and 2013 respectively. Her main research interests include VLSI design and test, circuit aging, embedded system, built-in self-test, etc.

Wang Liang was born in Nantong Jiangsu Province, China in 1978. He received B. E. degree in Nantong University, Jiangsu Province, China, in 2000. He received M.E. degree in Jiangsu University, Jiangsu Province, China, in 2010. His main research interests include the application of Internet of thing, RFID, and network security technology.

Chen Jin received the B.E. degree and M.S. degree in from Nanjing University of Posts and Telecommunications, Nanjing, China, in 2011 and Nantong University, Jiangsu Province, China, in 2015 respectively. Since 2015, she has been with Xinglin College, Nantong University, Jiangsu Province, China. Her research interests include microwave filters and antennas.

LTCC Wideband Bandpass Filter Based on Multi-layered Coupling

Xin Gao, Wenjie Feng*, and Wenquan Che

Department of Communication Engineering
Nanjing University of Science and Technology, Nanjing, 210094, China
fengwenjie1985@163.com

Abstract ─ A novel wideband bandpass filter (BPF) based on multi-layered coupling using low temperature co-fired ceramic (LTCC) technology is proposed. Four folded quarter-wavelength layered coupled lines are distributed in 3D space to achieve compact circuit structure. Two transmission zeros near edges of the passband response can be easily realized by the two quarter-wavelength open/short coupled lines. Besides over 15-dB out-of-band rejection, the insertion loss of less than 0.7 dB is realized in the passband. A prototype with 3-dB fractional bandwidth of 25.7% operated at 2.95 GHz is designed and fabricated.

Index Terms ─ Bandpass filter, LTCC, multi-layered coupling, open/short coupled lines, wideband.

I. INTRODUCTION

With the rapid development of wireless communication system, low temperature co-fired ceramic (LTCC) technology has been widely used in many microwave devices, due to its characteristics of low dielectric loss, high frequency, high Q value, multilayer layout and high integration. As vital passive components, more and more researches have been focused on bandpass filters (BPFs) with LTCC technology. At the early stage, LTCC BPFs based on lumped elements are popular and easy- implemented [1]-[3]. In [1], a capacitor connected between the input and output is utilized to create a feedback path to introduce two finite zeros near the passband. A compact BPF using negative coupling structure has been proposed; however, the selectivity of the passband is not so good due to lacking of transmission zeros at the upper stopband [2]. In addition, a wideband BPF with multiple transmission zeros are fabricated by cascading a high- and low-pass filter [3]. In order to improve the flexibility of the implement, semilumped elements are introduced in some LTCC BPFs [4]-[5]. Recently, several LTCC BPFs based on distributed elements were presented [6]-[7]. In [6], a compact LTCC BPF with wide stopband is proposed using discriminating coupling scheme, but the passband is not wide. Moreover, a LTCC wideband BPF based on the dual-mode stepped-impedance resonator was designed and fabricated [7].

In this letter, a novel LTCC wideband BPF based on multi-layered coupling is presented. The filter is completely constructed by distributed elements, which include two quarter-wavelength open/short coupled lines and two quarter-wavelength open coupled lines. The two transmission zeros near the passband can be independently controlled by the coupling value of two quarter-wavelength open/short coupled lines. The compact size can be easily realized by the folded transmission lines and multilayer technology. Due to the symmetry of the circuit, even/odd-mode method can be applied to analyze the characteristic of the filter.

II. DESIGN OF PROPOSED LTCC WIDEBAND BANDPASS FILTER

A. Analysis of planar structure of the filter

As shown in Fig. 1 (a), two quarter-wavelength open coupled lines (Z_{e1}, Z_{o1}, θ) are located between port 1 and 2, and two quarter-wavelength open/short coupled lines (Z_{e2}, Z_{o2}, θ) are shunted connected in the two ports as well as characteristic impedance $Z_0 = 50\ \Omega$. The planar circuit is symmetric along the plane AA′, when the even/odd-mode are excited, a virtual open/short appears along AA′, and the even/odd-mode input admittances Y_{even} and Y_{odd} of the equivalent circuits in Figs. 1 (b) and (c) can be illustrated as:

$$Y_{even} = j\frac{2\tan\theta}{Z_{e1}+Z_{o1}} + j\frac{(Z_{e2}+Z_{o2})\sin 2\theta}{(Z_{e2}+Z_{o2})^2\cos^2\theta-(Z_{e2}-Z_{o2})^2}, \quad (1)$$

$$Y_{odd} = j\frac{(Z_{e1}+Z_{o1})\sin 2\theta}{(Z_{e1}+Z_{o1})^2\cos^2\theta-(Z_{e1}-Z_{o1})^2} + j\frac{(Z_{e2}+Z_{o2})\sin 2\theta}{(Z_{e2}+Z_{o2})^2\cos^2\theta-(Z_{e2}-Z_{o2})^2}. \quad (2)$$

And the S-parameters of the filter can be expressed as:

$$S_{21} = \frac{Y_0(Y_{odd}-Y_{even})}{(Y_0+Y_{even})(Y_0+Y_{odd})}, S_{11} = \frac{{Y_0}^2-Y_{even}Y_{odd}}{(Y_0+Y_{even})(Y_0+Y_{odd})}, \quad (3)$$

where $Y_0 = 1/Z_0$, when $S_{21} = 0$, the two transmission zeros of the circuit in Fig. 1 (a) can be obtained as:

$$\theta_{tz1} = \arccos\frac{Z_{e2}-Z_{o2}}{Z_{e2}+Z_{o2}}, \quad \theta_{tz2} = \pi - \theta_{tz1}. \quad (4)$$

Submitted On: August 24, 2016
Accepted On: December 3, 2016

Consequently, the locations of the transmission zeros are only determined by the coupling coefficient k_2 ($k_2 = (Z_{e2}-Z_{o2})/(Z_{e2}+Z_{o2})$).

Figure 2 (a) shows the even/odd-mode input admittances versus θ, and Fig. 2 (b) shows $|S_{21}|$ versus the normalized frequency f/f_0. The bandwidth of the bandpass filter is mainly determined by the two even-modes (f_{e1}, f_{e2}). As shown in Fig. 2 (c), the in-band return loss improves as k_1 ($k_1 = (Z_{e1}-Z_{o1})/(Z_{e1}+Z_{o1})$) increases, but the out-of-band rejection level improves as k_1 decreases. Moreover, the 3-dB bandwidth and locations of transmission zeros have no changes as k_1 varies. It should be pointed that k_2 can be seen as independent parameters for adjusting the locations of two transmission zeros (f_{tz1}, f_{tz2}) as shown in Fig. 2 (d). When k_2 increases, the 3-dB bandwidth increases and f_{tz1}, f_{tz2} move far away from each other. The above transmission characteristic reduces the design complexity of the filter effectively.

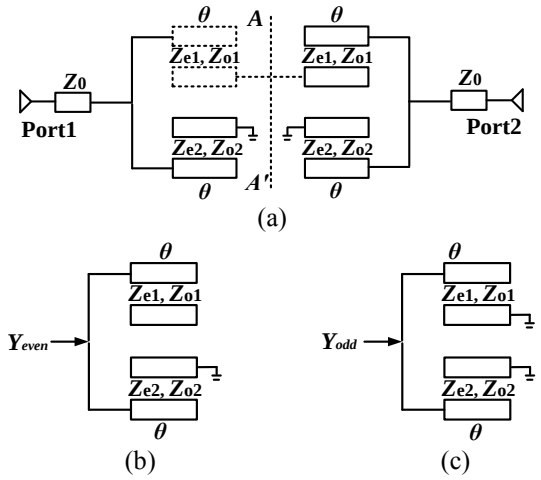

Fig. 1. The planar circuit diagram of proposed wideband BPF. (a) Ideal circuit of the filter, (b) even-mode equivalent circuit, and (c) odd-mode equivalent circuit.

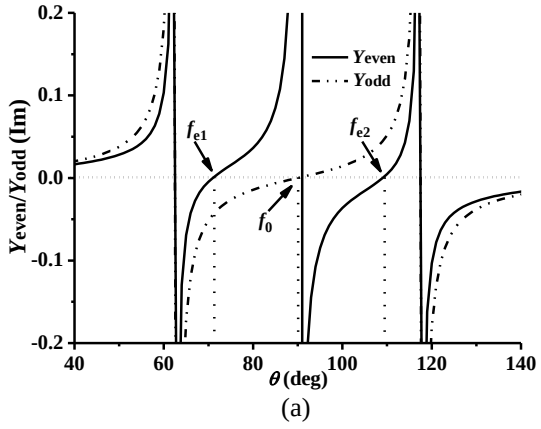

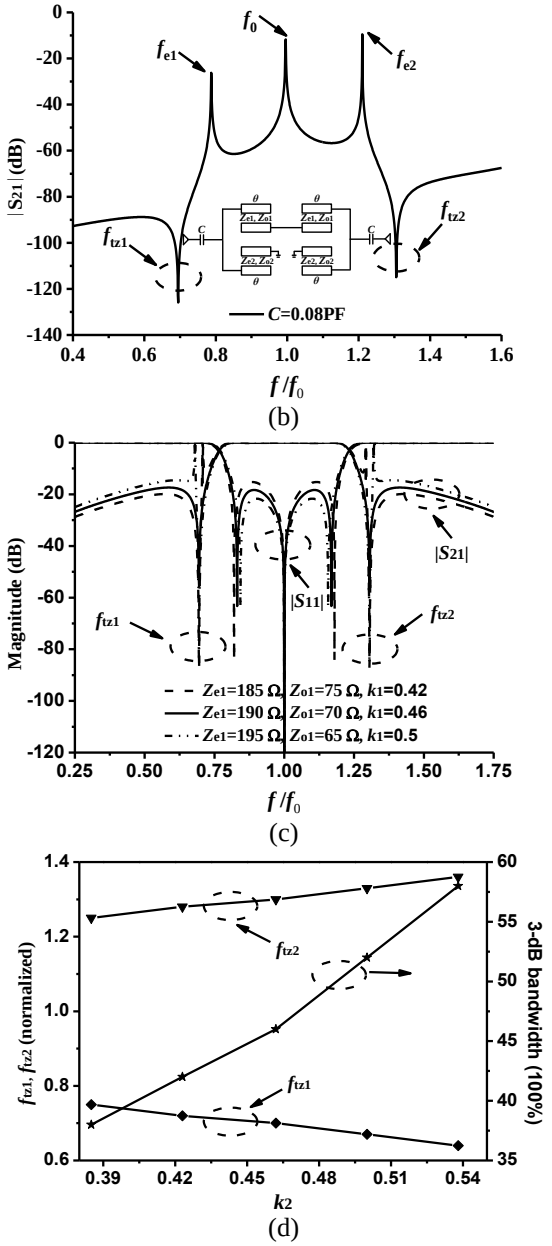

Fig. 2. Simulated frequency responses of Fig. 1. (a) Even/odd-mode resonant frequencies versus θ, (b) analysis of resonator frequencies under weak coupling, $Z_{e1} = Z_{e2} = 190\ \Omega$, $Z_{o1} = Z_{o2} = 70\ \Omega$, (c) $|S_{21}|\&|S_{11}|$ of Fig. 1 (a) versus k_1, $Z_{e2} = 190\ \Omega$, $Z_{o2} = 70\ \Omega$, and (d) f_{tz1}, f_{tz2} and 3-dB bandwidth versus k_2, $Z_{e1} = 90\ \Omega$, $Z_{o1} = 70\ \Omega$.

B. Constructions of LTCC 3D model of the filter

In order to obtain the compact size of the filter, the planar circuit can be converted into the LTCC 3D structure. As shown in Fig. 3 (a), the proposed filter is fabricated on a 14-layer LTCC substrate with the dielectric constant of 5.9 and loss tangent of 0.002. And the dielectric thickness of each layer is 0.1 mm. As we

can see, the planar edge-coupled structures have been improved to multi-layered coupled structures. In addition, the folded coupled lines can decrease its size efficiently. Figure 3 (b) shows the filter is composed of five metal layers. On the layer 1 are the G-S-G ports, and the rectangular metal sheets on the layer 2 linked between the ground and ports can be used to match the port impedance. The coupled quarter-wavelength resonators are on the layer 7 and 11, so the coupling gap (h_1) between coupled lines is 0.4 mm. It should be pointed that, the coupling gap of open/short coupled lines is $h_{1\text{-s}}$, and the coupling gap of open coupled lines is $h_{1\text{-o}}$. The ground plane is on the layer 15, and h_2 is also 0.4 mm. All the interconnection and grounding are realized by via-holes. The layout of each layer is shown in Figs. 3 (c)-(e), the parameters are determined as follows: w_1 = 0.37 mm, w_2 = 0.13 mm, w_3 = 0.5 mm, w_4 = 0.15 mm, w_5 = 0.3 mm, l_1 = 2 mm, l_2 = 12.3 mm, l_3 = 10.4 mm, l_4 = 21 mm, l_5 = 11.3 mm, l_6 = 7.2 mm, l_7 = 8.55 mm, s_1 = 0.8 mm. When $h_{1\text{-s}}$ increases, the two transmission zeros move towards each other and the bandwidth of the filter decreases as shown in Fig. 4 (a). As we know, the coupling coefficient k_2 decreases as $h_{1\text{-s}}$ increases, so the simulated results in Fig. 4 (a) are corresponding to the Equation (4). By contrast, Fig. 4 (b) shows the locations of the transmission zeros and bandwidth nearly have no changes when $h_{1\text{-o}}$ varies.

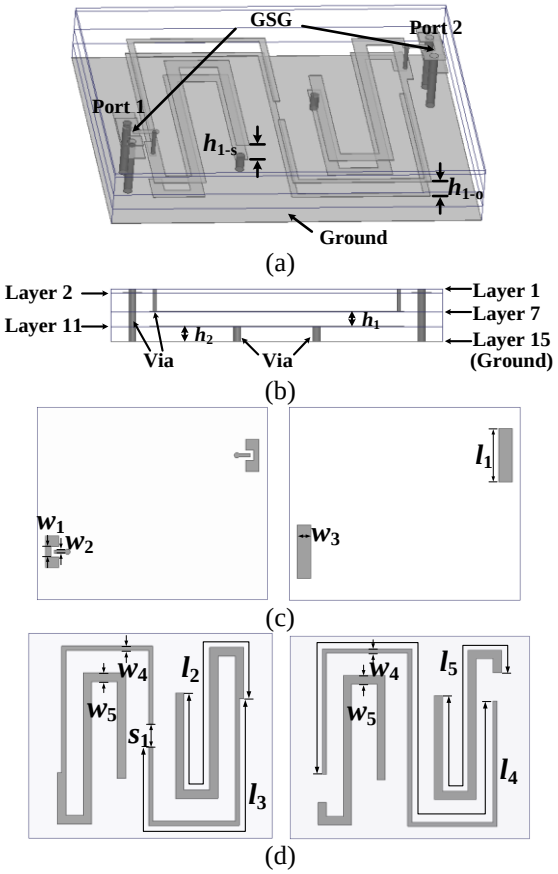

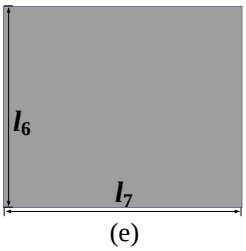

Fig. 3. Proposed LTCC wideband BPF configuration. (a) 3D structure, (b) side view, (c) layer 1 and layer 2, (d) layer 7 and layer 11, and (e) layer 15.

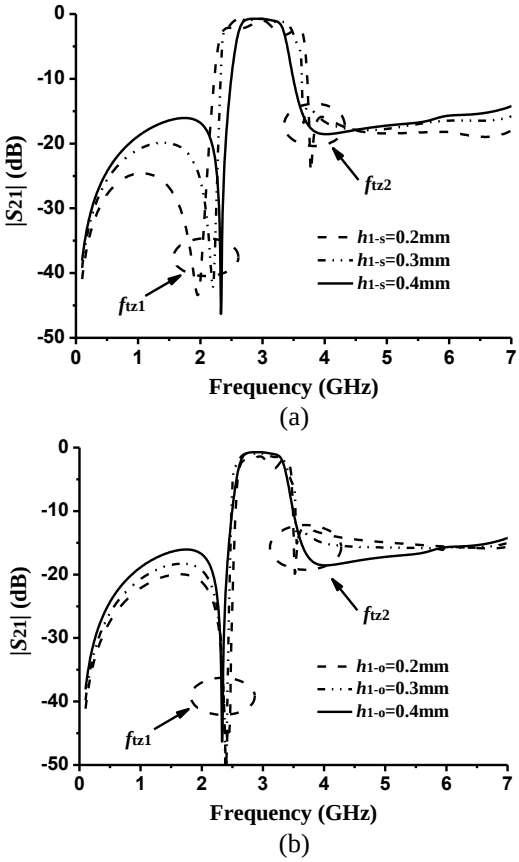

Fig. 4. Simulated frequency responses $|S_{21}|$ of the LTCC wideband BPF. (a) Versus $h_{1\text{-s}}$, $h_{1\text{-o}}$ = 0.4 mm, h_2 = 0.4 mm, and (b) versus $h_{1\text{-o}}$, $h_{1\text{-s}}$ = 0.4 mm, h_2 = 0.4 mm.

III. EXPERIMENT AND RESULTS

The measured and simulated results of the LTCC wideband BPF are illustrated in Fig. 5, which show good agreement. The measured centre frequency of the filter is 2.95 GHz with the 3-dB fractional bandwidth of 25.7%. The in-band return loss is greater than 20 dB, and the minimum insertion loss is only 0.7 dB. Over 15-dB out-of-band suppression can be realized by the two transmission zeros near the passband which are located at 2.32 and 3.88 GHz. In addition, the upper stopband

rejection is achieved from 3.52 to 7 GHz (2.37f_0). The photograph of the filter is also shown in Fig. 5, and its overall size is only 8.55mm×7.2mm×1.4mm.

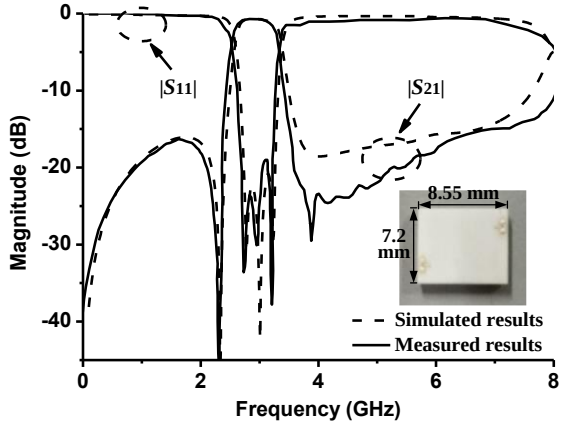

Fig. 5. Photograph, measured, simulated results of the LTCC wideband BPF.

IV. CONCLUSIONS

A novel LTCC wideband BPF based on multi-layered coupling is presented in this letter. The coupling amount of the quarter-wavelength resonators can be easily adjusted by the vertical spacing of the coupled lines. In addition, the two transmission zeros near the passband can be independently controlled by the quarter-wavelength open/short coupled lines, which reduces the complexity of the design obviously. Moreover, the advantages of compact size, good passband selectivity and wide out-of-band suppression of the proposed filter make it competitive for many wireless communication systems.

ACKONWLEGEMENT

This work is supported by the National Natural Science Foundation of China (61401206), Natural Science Foundation of Jiangsu Province (BK20140791) and the 2014 Zijin Intelligent Program of Nanjing University of Science and Technology.

REFERENCES

[1] L. K. Yeung and K.-L. Wu, "A compact second-order LTCC bandpass filter with two finite transmission zeros," *IEEE Trans. Microw. Theory Techn*., vol. 51, no. 2, pp. 337-341, Feb. 2003.

[2] W. Tung, Y. Chiang, and J. Cheng, "A new compact LTCC bandpass filter using negative coupling," *IEEE Microw. Wireless Compon. Lett*., vol. 15, no. 10, pp. 641-643, Oct. 2005.

[3] C. W. Tang and D. L. Yang, "Realization of multilayered wide- passband bandpass filter with low-temperature co-fired ceramic technology," *IEEE Trans. Microw. Theory Techn*., vol. 56, no. 7, pp. 1668-1674, July 2008.

[4] Y.-H. Jeng, S. F. R. Chang, and H.-K. Lin, "A high stopband-rejection LTCC filter with multiple transmission zeros," *IEEE Trans. Microw. Theory Techn*., vol.54, no. 2, pp. 633-638, Feb. 2006.

[5] K. W. Qian and X. H. Tang, "Design of LTCC wideband bandpass filter using semilumped resonators," *Electron. Lett*., vol. 47, no. 12, pp. 704-705, June 2011.

[6] X. Y. Zhang, X. Dai, H. L. Kao, B. H. Wei, Z. Y. Cai, and Q. Xue, "Compact LTCC bandpass filter with wide stopband using discriminating coupling," *IEEE Trans. Compon*., *Packag*., *Manuf. Technol*, vol. 4, no. 4, pp. 656-663, Apr. 2014.

[7] J. X. Chen, Y. Zhan, and Q. Xue, "Novel LTCC distributed-element wideband bandpass filter based on the dual-mode stepped-impedance resonator," *IEEE Trans. Compon*., *Packag*., *Manuf. Technol*, vol. 5, no. 3, pp. 372-380, Mar. 2015.

Xin Gao was born in Nantong, Jiangsu, China, on October 22, 1989. He received the B.S. degree from Nanjing University of Science and Technology (NUST), Nanjing, China, in 2012, where he is currently working toward the Ph.D. degree.

He worked as a Research Assistant in the Wireless Communication Laboratory, Faculty of Science and Technology, University of Macau from January 2015 to July 2015. He has authored or co-authored several international journal papers. His research interests include planar microstrip filters, diplexers, differential network, LTCC circuits and antennas.

Wenjie Feng was born in Shangqiu, Henan Province, China, in 1985. He received the B.Sc. degree from the First Aeronautic College of the Airforce, Xinyang, China, in 2008, the M.Sc. and Ph.D. degrees from the Nanjing University of Science and Technology (NUST), Nanjing, China, in 2010, 2013.

From November 2009 to February 2010, he was a Research Assistant with the City University of Hong Kong. From October 2010 to March 2011, he was an Exchange Student with the Institute of High-Frequency Engineering, Technische Universität München, Munich, Germany. He is currently a Teacher with the Nanjing University of Science and Technology, Nanjing, China. He has authored or co-authored over 120 internationally

referred journal and conference papers, including over 20 IEEE Transactions and Letters. He has obtained the Second Class Science and Technology Award and Best Dissertation Award of Jiangsu Province in 2015. His research interests include ultra-wideband (UWB) circuits and technologies, substrate integrated components and systems, planar filters and power dividers, balanced circuits and systems, LTCC circuits.

Feng is a Reviewer for over twenty internationally referred journal including ten IEEE Transactions and Letters, and TPC members for some conferences. He serves as an Associate Editor for the *International Journal of Electronics* from 2015.

Wenquan Che received the B.Sc. degree from the East China Institute of Science and Technology, Nanjing, China, in 1990, the M.Sc. degree from the Nanjing University of Science and Technology (NUST), Nanjing, China, in 1995, and the Ph.D. degree from the City University of Hong Kong (CITYU), Kowloon, Hong Kong, in 2003.

In 1999, she was a Research Assistant with the City University of Hong Kong. From March 2002 to September 2002, she was a Visiting Scholar with the Polytechnique de Montréal, Montréal, QC, Canada. She is currently a Professor with the Nanjing University of Science and Technology, Nanjing, China. From 2007 to 2008, she conducted academic research with the Institute of High Frequency Technology, Technische Universität München. During the summers of 2005–2006 and 2009–2012, she was with the City University of Hog Kong, as Research Fellow and Visiting Professor. She has authored or co-authored over 200 internationally referred journal papers and international conference papers. She has been a Reviewer for *IET Microwaves, Antennas and Propagation*. Her research interests include electromagnetic computation, planar/coplanar circuits and subsystems in RF/microwave frequency, microwave monolithic integrated circuits (MMICs) and medical application of microwave technology.

Che is a Reviewer for the IEEE Transactions on Microwave Theory and Techniques, IEEE Transactions on Antennas and Propagation, IEEE Transactions on Industrial Electronics, and IEEE Microwave and Wireless Components Letters. She was the recipient of the 2007 Humboldt Research Fellowship presented by the Alexander von Humboldt Foundation of Germany, the 5th China Young Female Scientists Award in 2008 and the recipient of Distinguished Young Scientist awarded by the National Natural Science Foundation Committee (NSFC) of China in 2012.

Compact Modified Quarter Mode Substrate Integrated Waveguide Resonator and Its Application to Filters Design

Y.-Z. Zhu*, W.-X. Xie, X. Deng, and Y.-F. Zhang

Department of Information Engineering
Engineering University of the Chinese People Armed Police, Xi'an, Shaanxi, 710086, P. R. China
*haiyihaiyi@hotmail.com, 1558125018@qq.com, 33591232@qq.com, 250578730@qq.com

Abstract ─ A novel compact modified quarter mode substrate integrated waveguide (QMSIW) resonator is proposed. The dominant resonant mode of the proposed resonator is TE_{101} mode. Using modified QMSIW resonator can reduce 97.3% in size with respect to its corresponding substrate integrated waveguide (SIW) counterpart. With the new coupling structures, the miniaturized cavity can be properly arranged in the filter design to minimize the footprint of the circuit. Two novel filters using compact modified QMSIW cavity are designed, and these proposed compact filters are fabricated to prove the predicted results in experiments, in which good agreement is obtained.

Index Terms ─ Filter, substrate integrated waveguide, TE_{101} mode.

I. INTRODUCTION

Substrate integrated waveguide (SIW) circuits have many advantages such as low cost and high quality factor, so they are well suited to realize passive components in microwave and millimeter wave integrated circuits. Nevertheless, the biggest drawback of SIW is that the physical dimension may be too large for lower microwave integrated circuits [1-4].

In 2006, the concept of half mode substrate integrated waveguide (HMSIW) was proposed, which can reduce the size of SIW components by half [5-6]. The field distribution of the HMSIW remains almost unchanged compared with that of the original SIW. The center symmetrical plane of the HMSIW is equivalent to a quasi-magnetic wall for some particular modes. The HMSIW can be further bisected into two parts again along the symmetrical plane. As a result, a quarter mode substrate integrated waveguide (QMSIW) can be achieved and its size is only the half of HMSIW resonator cavity [7-9]. An eighth-mode SIW (EMSIW) resonator cavity has been realized by bisecting the QMSIW. The cavity is only one-eighth the size of the SIW [10,11].

Another size miniaturization approach is folding in its thickness direction [12-19]. In 2005, folded SIW (SIFW) concept has been proposed [13]. SIFW exhibits similar cutoff frequency and propagation characteristics while only occupies half the room of its SIW equivalent structure, and then the double-folded SIW (DFSIW) [14-17] has been proposed. This DFSIW resonator cavity has the footprint only a quarter of the original SIW cavity, but still keeps similar high Q property. In [18,19], compared with classical SIW resonant cavity, the circuit area of the quadruple folded SIW (QFSIW) resonant cavity can be decreased to 89%.

Meanwhile, folded HMSIW (FHMSIW) has been applied in designing microwave devices. FHMSIW [20] and double folded HMSIW (DFHMSIW) [21] can be properly arranged in the filter design to minimize the footprint of the circuit. DFQMSIW are able to reduce the dimension of SIW components by approximately 94% [22,23].

In this paper, a compact modified QMSIW resonator is proposed and used to design high performance microwave filters in the paper. The compact modified QMSIW resonator is operated at TE_{101} mode, with more than 97.3% size reduction in contrast with the traditional SIW filter. Two novel filters using compact modified QMSIW cavity are designed, including single bandpass and dual bandpass filters. The results of the simulation and experimentation matched very well. Thus, the proposed method has been proved to be feasible.

II. COMPACT MODIFIED QMSIW CAVITY

Figures 1 (a) and (b) show the structure of a compact modified QMSIW cavity, which is composed of a bottom conductor plane, two dielectric layers, a middle metallic conductor plate with a C-shaped slot, and a top conductor plane. The top conductor plane and bottom conductor plane are united through the C-shaped slot as a whole. Its height is two times of the original SIW, because it has two layers of substrate with height of h. The length ($L^{'} = 2(L_1 + L_2)$) of the C-type slot obviously affects the miniaturization of the QMSIW cavity.

A conventional SIW cavity with $36 \times 36\,\mathrm{mm}^2$ area is designed on Rogers RT/Duriod 5880 substrate with the relative permittivity of 2.2 and the height of 0.508 mm.

Submitted On: September 19, 2016
Accepted On: December 13, 2016

Its $\tan\delta = 0.0009$. As a result a fundamental TE_{101} mode exists around 3.9 GHz. For a fixed QMSIW cavity resonator size, inserting C-type slot into the structure will reduce the resonance frequency. The miniaturization factor for a particular miniaturized resonator operating at a lower frequency of f_0 is computed using miniaturization factor (MF):

$$MF = \frac{A_{siw,f_0} - A_c}{A_{siw,f_0}} \times 100\%, \quad (1)$$

where A_{siw,f_0} is the area of a conventional SIW resonator, which fundamentally operates at f_0 and A_c is the area of the proposed modified QMSIW cavity resonators. This miniaturization factor contribution for each element is mentioned in the caption of Fig. 2 (a).

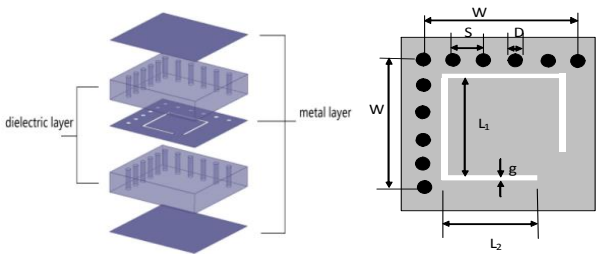

Fig. 1. The structure of a compact modified QMSIW cavity. (a) 3D configuration and (b) middle metal layer.

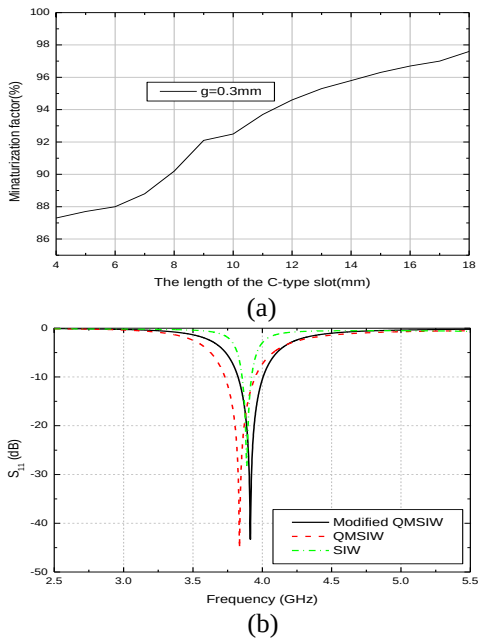

Fig. 2. (a) Miniaturization factor of the proposed modified QMSIW resonator for different C-type slot dimensions, and (b) simulated results of the compact modified QMSIW and SIW resonator.

Conventionally, the length of square SIW cavity with a dominant resonant mode of TE_{101} is of half wavelength. The resonant frequency of the TE_{101} mode is calculated usinEg equation (2) [24]:

$$f_{101}^{SIW} = \frac{C}{2\pi\sqrt{u_r\varepsilon_r}}\sqrt{(\frac{\pi}{W_{eff}^{SIW}})^2 + (\frac{\pi}{W_{eff}^{SIW}})^2}, \quad (2)$$

$$W_{eff}^{SIW} = W - 1.08\frac{(d)^2}{S} + 0.1\frac{(d)^2}{W}, \quad (3)$$

where u_r is the relative permeability of the substrate and ε_r is the permittivity of the substrate. C stands for the velocity of light in vacuum. W_{eff}^{SIW} represents the equivalent width of the corresponding original square SIW structure. W is the length and width of the original square SIW cavity resonator. d and s are the diameter of via and the distance between adjacent vias, respectively. The fundamental resonant mode in the compact modified QMSIW structure is still the TE_{101} mode, and its resonant frequency is given by Equation (4) [25]:

$$f_{101}^{Modeifed} = \frac{C}{p\sqrt{2u_r\varepsilon_r}W_{eff}^{Modified}}, \quad (4)$$

$$W_{eff}^{Modified} = W_{eff}^{SIW} / p + \Delta W, \quad (5)$$

where $W_{eff}^{Modified}$ is the equivalent width of compact modified QMSIW. P is the multiple of the length of the original substrate integrated waveguide with respect to the length of the proposed modified QMSIW substrate integrated waveguide. The value of P is mainly determined by the length of the C-type slot, which is between 2 and 6. ΔW is the additional width and achieved because of the change in feeding position. In fact, the magnetic walls are not ideal on account of fringing fields [25].

A compact modified QMSIW cavity with $6\times6\,mm^2$ area is designed on Rogers RT/Duriod 5880 substrate. The relative permittivity and the height of the substrate is 2.2 and 0.508 mm, respectively. Its $\tan\delta = 0.0009$, $L = 17.6mm$, $L_1 = 4.8mm$, $L_2 = 4mm$, $s = 1.2mm$, $D = 0.8mm$, g is fixed to 0.3mm. A conventional SIW cavity with 36×36 mm^2 area and a conventional single layer QMSIW cavity with $18\times18\,mm^2$ are designed in the same condition. Figure 2 (b) shows the simulated S-parameter curve of the modified QMSIW cavity, the conventional QMSIW cavity and the conventional SIW cavity. It is shown that the TE_{101} mode resonant frequency of the proposed compact modified QMSIW almost remains unchanged compared with that of the corresponding original SIW resonator cavity. When the width of compact modified QMSIW is nearly 1/6 of the corresponding SIW, the compact modified QMSIW can preserve similar propagation and cutoff characteristics with the SIW structure, with the advantages of simple structure, compact size and the merit of low-loss.

Therefore, the compact modified QMSIW cavity can be used for the circuit size reduction with its footprint about 2.7% of the conventional TE_{101} mode. However, the unloaded Q factor (Q_u) of the proposed compact modified QMSIW is smaller than that of the corresponding SIW in the same condition, because the open edges are not perfect magnetic walls and a certain amount of radiation may happen. In our design, Q_u is about 186. Under the same conditions, the Q_u of the corresponding SIW resonator is around 270. The E-field distribution of the upper layer is the same as that of the down layer. The field distribution of the compact modified QMSIW in the fundamental mode is different from that of SIW. The maximum electric field does not concentrate on the center. Instead, it is focused on the C-shaped slot region, as shown in Fig. 3. Table 1 lists the comparative results among different compact SIW resonant cavities.

It is demonstrated that our configuration is the smallest structure.

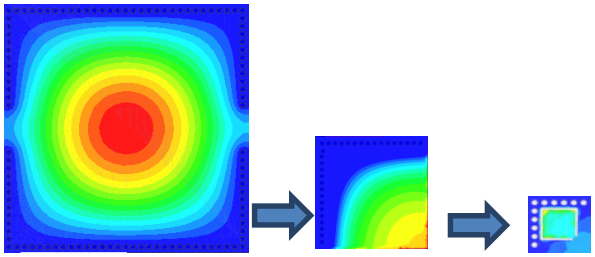

Fig. 3. Electric field distribution of different cavities. (a) SIW, (b) QMSIW, and (c) modified QMSIW.

Table 1: Comparison with different compact SIW resonant cavities

Type	f_g	Q_u	Dimensions(L×W×H)	ε_r
HMSIW in [5]	9.88 GHz	250	$0.52\lambda_0 \times 0.26\lambda_0 \times 0.008\lambda_0$	2.94
QMSIW in [7]	5.85 GHz	172.8	$0.195\lambda_0 \times 0.195\lambda_0 \times 0.005\lambda_0$	2.94
EMSIW [10]	3.29 GHz	Not calculated	$0.5\times(0.197\lambda_0 \times 0.197\lambda_0 \times 0.017\lambda_0)$	2.2
SIFW in [13]	10.03 GHz	206	$0.32\lambda_0 \times 0.16\lambda_0 \times 0.013\lambda_0$	5.9
DFSIW in [14]	30 GHz	94	$0.253\lambda_0 \times 0.253\lambda_0 \times 0.088\lambda_0$	7.8
QFSIW [19]	3.2 GHz	232	$0.128\lambda_0 \times 0.128\lambda_0 \times 0.01\lambda_0$	3.5
FHMSIW in [21]	5.5 GHz	Not calculated	$0.179\lambda_0 \times 0.258\lambda_0 \times 0.019\lambda_0$	2.2
DFHMSIW in [21]	5.5 GHz	Not calculated	$0.138\lambda_0 \times 0.147\lambda_0 \times 0.019\lambda_0$	2.2
QFQMSIW in the paper	3.19 GHz	186	$0.06\lambda_0 \times 0.06\lambda_0 \times 0.01\lambda_0$	3.5

f_g is resonating frequency; is resonating frequency; λ_0 is the wavelength in vacuum at f_g

III. COMPACT MODIFIED QMSIW FILTERS DESIGN

A. Design of three-order bandpass filter

In this section, the filter has a fractional bandwidth of 12.8% at 4.62 GHz. A three order Chebyshev filter with 20 dB of passband return loss is regarded as the prototype. The coupling coefficient and the external quality factor can be calculated by [26]:

$$M_{12} = 0.125; M_{23} = 0.125; Q_{e1} = 7.01; Q_{e3} = 7.01,$$

where $M_{i,i+1}$ represents the coupling coefficient between resonator i and resonator i+1, while Q_{e1} and Q_{e3} stand for the external quality factors of the input and output.

The schematic coupling topology of the proposed bandpass filter is depicted in Fig. 4. Because compact modified QMSIW cavity is not strictly symmetrical, M_{12} (the coupling between cavity 1 and cavity 2) and M_{23} (the coupling between cavity 2 and cavity 3) can't be realized in the same way. The layout of the proposed cascaded compact modified QMSIW filter is shown in Fig. 5. The magnetic coupling is achieved through the coupling window between cavity 1 and cavity 2. The coupling characteristic and coupling strength can be flexibly controlled and modified by adjusting the size (Lp) of the window. Meanwhile, a coupling slot and metallic via hole printed between cavity 2 and cavity 3 can produce mixed electric and magnetic coupling. The value of mixed coupling is mainly under the control of the slot size (Lt) and the number of the metallic via holes.

The filter is realized by using the substrate with Rogers RT/Duriod 5880, with thickness of 0.508 mm, and the dimensions are given as below: La=18mm, Wm=6.75mm, Ws=1.35mm, Ls=4.1mm, L1=3.95mm, L2=3.9mm, L3=3.5mm, Wp=1.9mm, Lp=4mm, Lt=4mm, s1=0.2mm. The proposed filter is shown in Fig. 6.

The data are measured by Agilent E5071C vector network analyzer (VNA). Figure 7 depicts the simulated and measured frequency responses. The measured bandwidth of the filter is 12.8% in the center frequency of 4.62 GHz. The measured return loss in the passband is more than 14 dB, while the measured minimum insertion loss is approximately 1.4 dBin the passband. Because TE_{102} mode of the square SIW resonator is not generated in compact modified QMSIW cavity, the

proposed filter has a very good suppression characteristic in the out-off-band, and the S_{21} parameter is better than 20 dB in relatively wide-band. The energy loss of the proposed filter mainly comes from the material and SMA connectors. The good agreement between measured and simulated results demonstrates that the presented method is effective. For modified QMSIW, the predicted resonance for TE_{202} mode is excited at 7.35 GHz, so there appears a ripple at around 7.35 GHz.

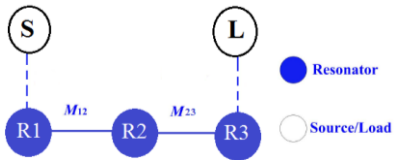

Fig. 4. Coupling scheme of the proposed three-cavity filter.

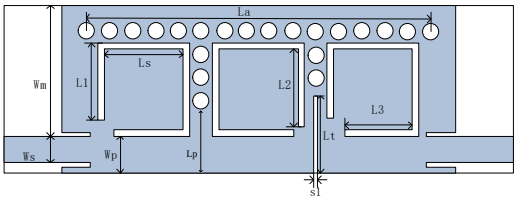

Fig. 5. Configuration of the middle conductor layer in the proposed three-cavity filter.

(a) (b) (c)

Fig. 6. Photograph of the proposed three-cavity filter prototype. (a) Top and bottom metal layer of the first substrate, (b) top and bottom metal layer of the second substrate, and (c) assembled filter prototype.

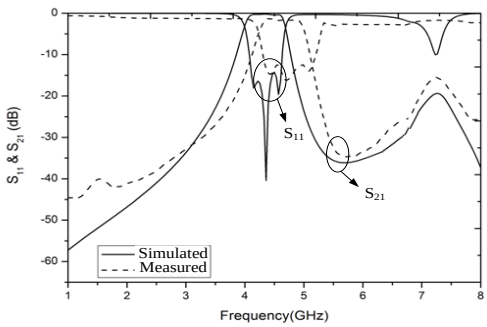

Fig. 7. Simulated and measured results of the three-cavity filter.

B. Design of four-cavity dual-band filter

In this section, a four-cavity dual-band filter is designed. The central first band frequency is f_1=3.6 GHz, the central second band frequency is f_2=4.8 GHz, and the corresponding bandwidths are BW=0.4 GHz and BW=0.3 GHz, respectively. The return loss is 20 dB in the both bands. The coupling matrix is obtained as follows:

$$\begin{bmatrix} 0 & 1.082 & 0 & 0 & 0 & 0 \\ 1.082 & 0 & 3.418 & 0 & -0.569 & 0 \\ 0 & 3.418 & 0 & -0.661 & 0 & 0 \\ 0 & 0 & -0.661 & 0 & 3.418 & 0 \\ 0 & -0.569 & 0 & 3.418 & 0 & 1.082 \\ 0 & 0 & 0 & 0 & 1.082 & 0 \end{bmatrix}$$

Here, the dual-band characteristic has been achieved by adjusting the position of the microstrip-probe coupling. The schematic coupling topology of the proposed four-cavity dual-band filter is shown in Fig. 8 (a). The physical model of the proposed compact modified QMSIW dual-band filter is shown in Fig. 8 (b).

The coupling between cavity 2 and cavity 3 can be flexibly controlled and modified by adjusting the position of the slot and the number of the metallic via holes. The coupling between cavity 1 and cavity 4 is produced by the common-slot. The coupling between cavity 1 and cavity 2 and the coupling between cavity 3 and cavity 4 can't be realized by the coupling window, because the structure makes transmission of energy hard. The coupling is achieved through the microstrip-probe between resonator 1(3) and resonator 2(4). The probe can generate higher mode, so dual-band characteristics can be obtained by adjusting the position and size of microstrip-probe. The dual-band filter is realized by using the substrate with Rogers RT/Duriod 5880 with the thickness of 0.508 mm. The configuration size of the proposed filter is shown in Fig. 9. By simulation and optimization, the dimensions are given as follows: La=14.6, Lb=14.6, m1=3, L1=4.1, L2=4.1, Lq=4.1, Wa=1.9, L3=3.75, L4=8.25, L5=4.88, Ls=5.8, Ws=1.1, s0=0.3, Lr=3.6, T1=12.7, P1=1.4, T2=11.9, P2=0.6, Lp=6, Lt=1.8, Rt=5.7 (all in mm).

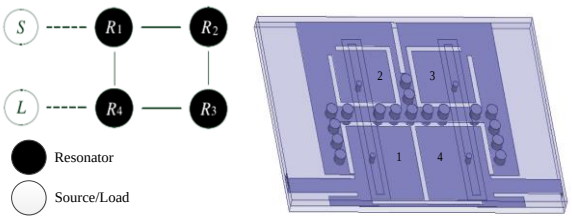

(a) (b)

Fig. 8. (a) Schematic coupling topology of the proposed filter (S: source, L: load, R: resonator), and (b) 3D configuration of the proposed compact cross-coupled dual-band filter using compact modified QMSIW resonators.

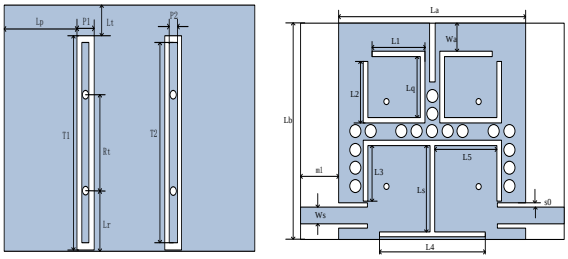

(a) (b)

Fig. 9. The configuration size of the proposed filter. (a) Top metal layer, and (b) middle metal layer.

Figure 10 shows a photograph of the filter. A HP network analyzer is chosen to measure the performance of the fabricated filter. In Fig. 11, the simulated and measured results are shown. The simulated and measured frequency responses demonstrate that an excellent agreement is obtained. A 3 dB fractional bandwidth of approximately 14% in the measured lower passband where the central frequency is about 3.62 GHz is presented, and the insertion loss in the lower passband is about 1.2 dB at the central frequency. Meanwhile, a 3 dB fractional bandwidth of approximately 6.25% in the measured upper passband where the central frequency is approximately 4.82 GHz is presented, and the insertion loss is about 2.1 dB at the central frequency. The return losses are better than 15 dB in the passband. It seems that the higher measured insertion loss at the higher passband is due to unfavorable coupling. There's something a little bit different between the passband bandwidths and the asymmetrical frequency response. It may be caused by certain minor cross coupling and structural difference.

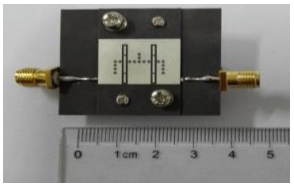

Fig. 10. Photograph of the proposed four-cavity filter.

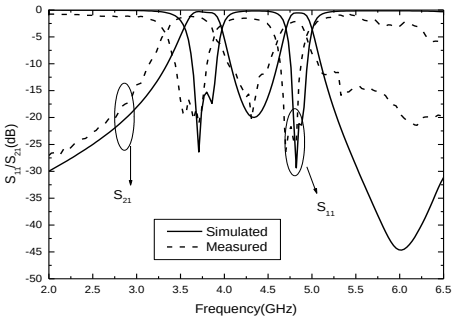

Fig. 11. Simulated and measured results of the four-cavity filter.

IV. CONCLUSION

A novel compact modified QMSIW resonator is designed, and the proposed compact modified QMSIW cavity has good performance, while the size reduction is up to 97.3% compared with the conventional SIW cavity. Thus, it is well suited for designing miniaturization circuit. Several novel filters using compact modified QMSIW cavity are designed, including single passband and dual passband filters. The designs of the proposed filters are based on full-wave electromagnetic simulation. The measured performance of these filters is in good agreement with the simulated ones.

ACKNOWLEDGMENT

This work was supported by the National Natural Science Foundation of China (No. 61302051); the Basic Research Program of ENGG University of the Chinese People Armed Police Force (No. WJY201606).

REFERENCES

[1] D. Deslandes and K. Wu, "Integrated microstrip and rectangular waveguide in planar form," *IEEE Microw. Wireless Compon. Lett*., vol. 11, no. 2, pp. 68-70, 2001.

[2] Y. L. Zhang, W. Hong, K. Wu, et al., "Design and realization of a novel substrate integrated waveguide filter," *Journal of Microwaves*, vol. 21, no. 4, pp. 138-141, 2005.

[3] H. Y. Wang, G. H. Li, Y. D. Wu, et al., "A novel triple-band filter based on triple-mode substrate integrated waveguide," *Progress in Electro-magnetics Research Letters*, vol. 58, pp. 59-65, 2016.

[4] K. Wang, S. W. Wong, G. H. Sun, et al., "Synthesis method for substrate integrated waveguide (SIW) bandpass filter with even-order Chebyshev response," *IEEE Transactions on Components Packaging & Manufacturing Technology*, vol. 6, no. 1, pp. 126-135, 2016.

[5] W. Hong, B. Liu, Y. Wang, et al., "Half mode substrate integrated waveguide: A new guided wave structure for microwave and millimeter wave application," *31st International Conference on Infrared and Millimeter Waves and 14th International Conference on Terahertz Electronics Proceedings*, pp. 18-22, 2006.

[6] Y. J. Chen, W. Hong, and K. Wu, "Half mode substrate integrated waveguide (HMSIW) directional filter," *IEEE Microw. Wireless Compon. Lett*., vol. 17, no. 7, pp. 504-506, 2007.

[7] Z. Zhang, "Substrate integrated waveguide devices and receiver systems for millimeter wave applications," *Ph.D. Dissertation, Dept. École Polytechnique de Montréal, Univ. Montreal*, Montreal, PQ, Canada, 2011.

[8] M. U. Memon and S. Lim, "Frequency-tunable compact antenna using quarter-mode substrate integrated waveguide," *IEEE Antennas & Wireless Propagation Letters*, vol. 14, no. 3, pp. 1606-1609, 2015.

[9] J. Chen and Z. Shen, "Compact triple-mode filter based on quarter-mode substrate integrated waveguide," *IEEE Transactions on Microwave Theory & Techniques*, vol. 62, no. 1, pp. 37-45, 2014.

[10] Y. Z. Zhu, "A source-load coupled bandpass filter using one-eighth mode substrate integrated waveguide cavity," *31st URSI General Assembly and Scientific Symposium*, pp. 1-4, 2014.

[11] H. Kang and S. J. Lim, "Compact right-angled triangle-shaped eight-mode substrate-integrated waveguide antenna," *Microwave and Optical Technology Letters*, vol. 57, no. 3, pp. 690-694, 2015.

[12] J. S. Hong, "Compact folded-waveguide resonators and filters," *IEEE Trans. Antennas Propag*, vol. 54, no. 4, pp. 325-329, 2006.

[13] L. S. Wu, X. L. Zhou, and W. Y. Yin, "A novel multilayer partial H-Plane filter implemented with folded substrate integrated waveguide (FSIW)," *IEEE Microw. Wireless Compon. Lett*., vol. 19, no. 8, pp. 494-496, 2009.

[14] H. Y. Chien, T. M. Shen, T. Y. Huang, et al., "Miniaturized bandpass filters with double-folded substrate integrated waveguide resonators in LTCC," *IEEE Transactions on Microwave Theory & Techniques*, vol. 57, no. 7, pp. 1774-1782, 2009.

[15] G. Yang, W. Liu, and F. L. Liu, "Two new electric coupling structures for double folded substrate integrated waveguide cavity filters with transmission zeros," *Microwave and Optical Technology Letters*, vol. 55, no. 8, pp. 1815-1818, 2013.

[16] L. J. Xu, J. P. Wang, Y. X. Guo, et al., "Double-folded substrate integrated waveguide band-pass filter with transmission zeros in LTCC," *Journal of Electromagnetic Waves & Applications*, vol. 27, no. 1, pp. 96-103, 2013.

[17] Q. Zhang, B. Z. Wang, W. Y. Yin, et al., "Design of a miniaturized dual-band double-folded substrate integrated waveguide bandpass filter with controllable bandwidths," *Progress in Electromagnetics Research*, vol. 136, pp. 211-223, 2013.

[18] T. Y. Huang, T. M. Shen, and R. B. Wu, "A miniaturized bandpass filter using quadruple folded laminated waveguide cavity resonators in LTCC," *IEEE Asia-Pacific Microwave Conference Proceedings (APMC)*, pp. 99-102, 2010.

[19] C. A. Zhang, Y. J. Cheng, and Y. Fan, "Quadri-folded substrate integrated waveguide cavity and its miniaturized bandpass filter applications," *Progress In Electromagnetics Research C*, vol. 23, pp. 1-14, 2011.

[20] G. H. Zhai, W. Hong, K. Wu, et al., "Folded half mode substrate integrated waveguide 3dB coupler," *IEEE Microw. Wireless Compon. Lett*., vol. 18, no. 8, pp. 512-514, 2008.

[21] W. Hong and K. Gong, "Miniaturization of substrate integrated bandpass filters," *IEEE Asia-Pacific Microwave Conference Proceedings (APMC)*, vol. 21, pp. 247-250, 2010.

[22] Y Z. Zhu, "A compact double folded quarter mode substrate integrated waveguide (DFQMSIW) filter," *IEICE Electronics Express*, vol. 13, no. 17, pp. 1-7, 2016.

[23] J. Zhou, Y. Z. Zhu, and Z. H. Liu, "A novel miniaturization double folded quarter mode substrate integrated waveguide filter design in LTCC," *Progress In Electromagnetics Research Letters*, vol. 60, pp. 127-132, 2016.

[24] F. Xu and K. Wu, "Guided-wave and leakage characteristics of substrate integrated waveguide," *IEEE Trans. Microw. Theory Tech*., vol. 53, no. 1, pp. 66-72, 2005.

[25] Q. Lai, C. Fumeaux, W. Hong, et al., "Characterization of the propagation properties of the half-mode substrate integrated waveguide," *IEEE Trans. Antennas Propag*., vol. 57, no. 8, pp. 1996-2004, 2009.

[26] J. S. Hong and M. J. Lancaster, *Microstrip Filters for RF-Microwave Applications*. New York: John Wiley & Sons, 2001.

Waveguide Filter Modeling and Simulation using Mode-matching, Fullwave Network Analysis and Swarm Optimization

I. Bouchachi [1,2], J. Mateu [3], and M. L. Riabi [1]

[1] Laboratory of Electromagnetism and Telecommunications
University Mentouri of Constantine, Algeria
i.bouchachi@crti.dz, ml.riabi@yahoo.fr

[2] Research Center in Idustrial Technologies CRTI, Algiers, Algeria

[3] Centre Technologic de Telecomunicacions de Catalunya (CTTC), Barcelona, Spain
jordi.mateu@cttc.cat

Abstract ─ This paper presents the modeling of waveguide bandpass filter synthesis. It consists of a combination of the most appropriate and reliable methods and techniques of analysis, simulation and optimization used in determined order and leading to a fast and accurate method of filter synthesis. An example of a forth-order filter synthesis is given, employing a symmetric configuration and symmetric response. The obtained results, reference measurement and commercial software simulator results are compared for validation.

I. INTRODUCTION

During the last two decades, there has been an extension and trivialization of passive microwave components. On one hand, this is due to the fact that an exponential rate of ICT users has stimulated more and more labs to focus their research on this field. On the other hand, the IT development of both sides, hard and soft, allowing a high-speed implementation of programs and softwares of synthesis, simulation and optimization.

Among these microwave components, we find filters and precisely the waveguide filters. After a first appearance in telecommunications few years before World War II [1], they still occupy an important role, because when it comes to design filters operating at microwaves with very high gains and conveying great power, the use of waveguides becomes inevitable.

The majority of filters are synthesized from an equivalent circuit or a coupling matrix [2]. By translating the circuits or matrices into a combination of inverters and resonators to create a filter, one can summarize the synthesis of a filter in 4 stages: first, the synthesis of the equivalent circuit or coupling matrix, the choice of the technology to use and computation of the initial dimensions of the filter, the simulation of the filter response, and optimization of its dimensions. Each step mentioned is in itself a vast field of research.

Over the years, different forms and filter topologies have been proposed. First, linear uniaxial filters, often Chebyshev or Butterworth [3] of a quite large size and a frequency response without transmission zeroes, Rhodes proposed bended structures to reduce the size of the filters [4]. Then, a big step was taken with dual mode filters proposed by Atia and Williams [5], where they assumed that each resonator of the filter can be coupled with all the others with a coupling factor M, allowing a reduction in the size of the filter and improving its frequency response. Later, a multitude of topologies (folded, box, cul-de-sac ...) were used [6-8].

Simultaneously, studies were conducted to study the behavior of electromagnetic fields through cavities and obstacles, either by treating the waveguides as a simple transmission line [9], or by a full-wave analysis that has been developed in order to take into account higher order modes. We can mention the method of moments [10], the spectral analysis [11] and mode matching [12], which offer high strength and reliability. Other numerical methods were used as the method of finite elements and finite differences [11], taking advantage of advances in computer science; these methods have been at the basis of several commercial software for microwave structures simulation, like Ansoft HFSS or CST STUDIO SUITE.

After several unsuccessful attempts to direct synthesis of waveguide filter without going through the optimization step, the latter has been proved essential. Often metaheuristic, iterative and inspirited from nature like Genetic Algorithm, Practical Swarm Optimization and Neural Network, these optimization methods allow us to improve the filter response to satisfy predetermined filter specifications.

In this work, we have followed a method that we have found the most appropriate and reliable for the synthesis of a waveguide band-pass filter. It consists of

Submitted On: June 28, 2016
Accepted On: December 24, 2016

generating the coupling matrix starting from the desired response, drawing the global form from the filter topology and calculates the initial dimensions of the filter by the equivalent impedance image method [3]. After segmentation of the structure into several basic elements (junctions, bends and T-junction), each element is separately analyzed using the mode-matching technique, then the structure is treated as a network of these basic elements. In the end, we used PSO as an optimization method [13].

II. THE COUPLING MATRIX

In the early 1970s, Atia and Williams introduced the concept of the coupling matrix as applied to dual-mode waveguide filters [2]. This matrix describes the coupling between adjacent cavities, but also the coupling of each cavity with all other cavities of the filter. It is synthesized from the filter transfer function, the latter is itself obtained from the specifications of the filter response.

If in a filter, each resonator is coupled to all the others, the coupling matrix will contain only non-zero values. It is practically difficult and even impossible to achieve with a waveguide filter of higher order. Therefore, the goal is to use mathematical techniques to reduce the number of non-zero elements, leading to M matrices, similar to the initial matrix and which are substantially converted into filter.

In its final form, the matrix M proposed by Attia and Williams had symmetrical and multidiagonal elements. This form is called the canonical form and it was the basic element of many researchers whose purpose was to propose other forms of coupling matrices. Several matrices have been obtained and successfully tested. They are called "topologies" [6].

Later, commercial software called CMS Filter & Coupling Matrix Synthesis Software is developed by Guided Wave Technology's. By simply introducing the characteristics of the filter and checking the box where we need to introduce a coupling, then the coupling matrix is calculated with high accuracy.

In this work, for the synthesis of a forth-order filter, having a symmetric frequency response of elliptical shape with four poles and two zeros of transmission located at (normalized frequency) -1.8 and 1.8 with 20 dB of return losses, a coupling matrix has been synthesized. It is presented as following:

$$M = \begin{bmatrix} 0 & 0.856 & 0 & -0.220 \\ 0.856 & 0 & 0.786 & 0 \\ 0 & 0.786 & 0 & 0.856 \\ -0.220 & 0 & 0.856 & 0 \end{bmatrix}, \quad (1)$$

with normalized input/output resistances R=1.021.

III. INITIAL DIMENSIONS

Once the coupling matrix obtained, the equivalent electric circuit may easily be inferred, as replacing simply the coupling coefficient K_n by frequency invariant reactance inverters and the resonators by a capacitors C.

Figure 1 shows the equivalent circuit of a 4th order prototype filter, under the canonical form.

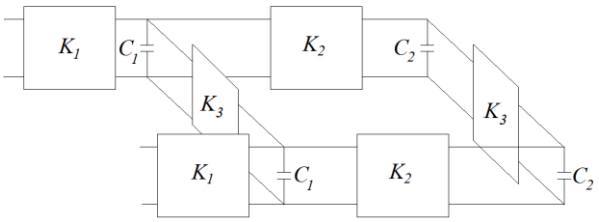

Fig. 1. Equivalent circuit of 4th order filter.

Since the final circuit consists of a quadripoles network connected in series and/or parallel, we can use ABCD to [Y] and [Y] to ABCD transformations to calculate the overall scattering parameters S_{11} and S_{21}; they will give us the ideal frequency response of the filter. This latter will be our reference for the synthesis of the waveguide filter.

Figure 2 shows the response of the equivalent circuit after transforming the low-pass prototype into a bandpass filter, with 10 GHz as central frequency, a bandwidth of 300 MHz and 20 dB of return loss level.

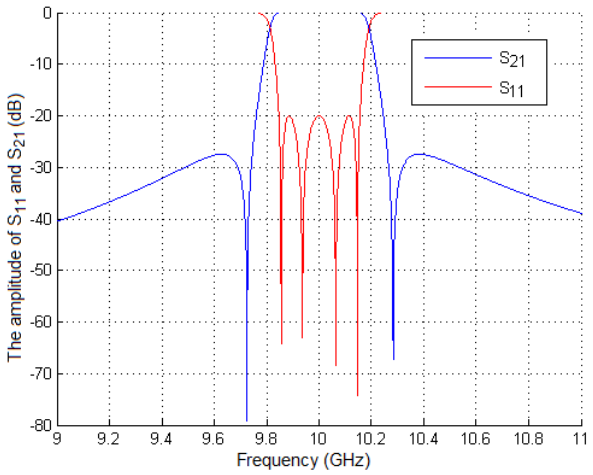

Fig. 2. *S*-parameters obtained from the coupling matrix.

The next step is to convert the equivalent circuit in a waveguide filter. To achieve this, we used the method of impedance images (impedance seen looking into a port of a network), which consists of inserting inside the waveguide geometric shapes or obstacles in order to obtain a structure having a similar impedance image than those quadripoles (inverter), these obstacles will separate a half-wave or quarter-wave cavities, which

will have the role of the resonators. To simplify the construction of the filter, in this work we have among our objectives to use as inverter only purely inductive or purely capacitive irises. The initial openings of these irises are deducted from curves drawn in [14] and the total electrical length θ of resonator cavity R is given by:

$$\theta_R = n\pi + \frac{1}{2}\left(\cot^{-1}\frac{B_1}{2} + \cot^{-1}\frac{B_2}{2}\right), \quad (2)$$

where B_1 and B_2 are the coupling susceptances of the two irises that define the cavity.

IV. MODE MATCHING METHOD

The mode-matching is a powerful method for analyzing waveguides with varying cross-section. It is based on the matching of the total mode fields at each junction between uniform sections (Fig. 3). The amplitudes of the modes at the output of a junction can be deduced in terms of the amplitudes of the mode spectrum at the input to the junction [12].

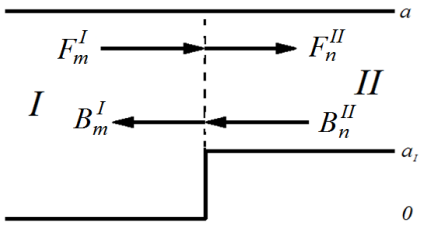

Fig. 3. Waveguide discontinuity.

Matching the transverse field components at the discontinuity we have:

$$\begin{cases} E_y^I = 0 & if: 0 \le x \le a_1 \\ E_y^I = E_y^{II} & if: a_1 \le x \le a \end{cases}, \quad H_x^I = H_x^{II} \quad if: a_1 < x \le a. \quad (3)$$

Then,

$$\sum_{m=1}^{M} T_m^I \sin\left(\frac{m\pi}{a}x\right)\left(F_m^I + B_m^I\right) = \sum_{m=1}^{N} T_n^{II} \sin\left(\frac{n\pi}{a-a_1}(x-a_1)\right)\left(F_n^{II} + B_n^{II}\right), \quad (4)$$

$$\sum_{m=1}^{M} T_m^I Y_m^I \sin\left(\frac{m\pi}{a}x\right)\left(F_m^I - B_m^I\right) = \sum_{m=1}^{N} T_n^{II} Y_n^{II} \sin\left(\frac{n\pi}{a-a_1}(x-a_1)\right)\left(F_n^{II} - B_n^{II}\right), \quad (5)$$

where F_m and B_m are the amplitudes of incident and reflected waves respectively. T_i are the power normalization terms. L_E and L_H (the report between input and output field component) can be calculated by power normalization and some algebraic calculation [15]:

$$F^I + B^I = L_E(F^{II} + B^{II}), \quad (6)$$

$$L_H(F^I - B^I) = F^{II} - B^{II}. \quad (7)$$

The S matrix expresses the scattered waves as a function of incident waves:

$$\begin{bmatrix} B^I \\ F^{II} \end{bmatrix} = [S]\begin{bmatrix} F^I \\ B^{II} \end{bmatrix}. \quad (8)$$

From Equations (4) and (5), and to simplify the S matrix calculation, we write it as a vectoiel product:

$$[S] = inv\begin{bmatrix} I & -L_E \\ -L_H & -I \end{bmatrix} * \begin{bmatrix} -I & L_E \\ -L_H & -I \end{bmatrix}. \quad (9)$$

To check the proper functioning of this analysis, we applied it on a filter already proposed in the literature, and then compare the results.

We chose the filter proposed by Chen in [16], because, as shown in Fig. 4, only resonants irises are used; and this kind of iris necessitates a TE-TM fullwave analysis. Figure 5 shows that the results were very satisfactory.

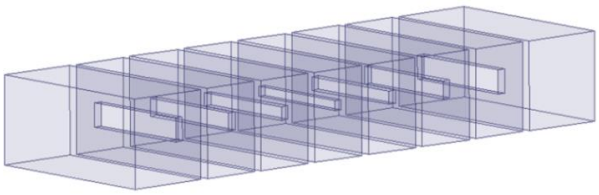

Fig. 4. Seven-iris bandpass filter proposed in [16].

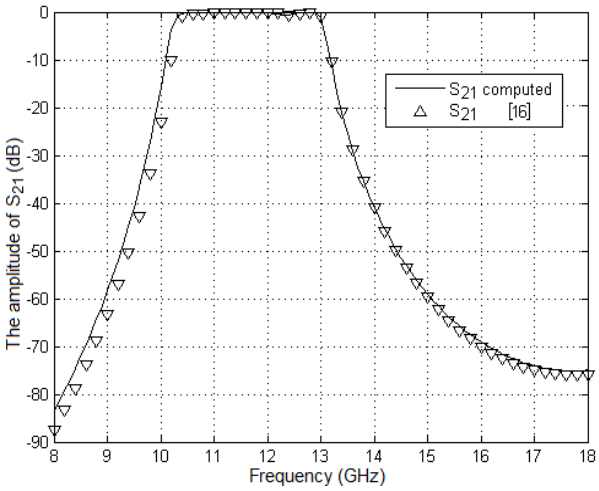

Fig. 5. Frequency response of the seven-iris bandpass filter.

A. Waveguide bend

Considering a waveguide bend in Fig. 6, we can

divide it into three regions, waveguide I, waveguide II, and resonator region III (the center square with the post bounded by the conducting wall, broken line in figure).

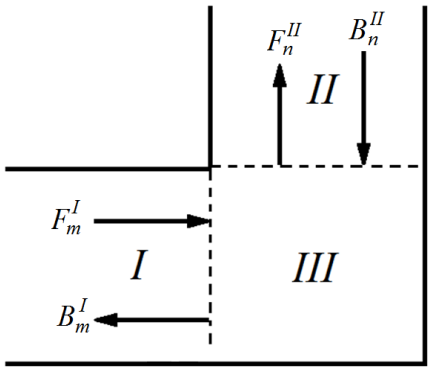

Fig. 6. Waveguide 90° bend.

By an application of a superposition principle, the total fields in the resonator region can be superposed by the field solutions satisfying boundary conditions. Then the fields in this resonator region are derived from the component of the electric and magnetic vector potentials A^i, where F and B, are the unknown eigenmode amplitude coefficients [17]:

$$A^I = \sum_{m=1}^{M} T_m^I \sin\left(\frac{m\pi}{a}x\right)\left(F_m^I e^{-jk_m^I z} - B_m^I e^{+jk_m^I z}\right), \quad (10)$$

$$A^{II} = \sum_{m=1}^{N} T_m^{II} \sin\left(\frac{n\pi}{a}z\right)\cdot \left(F_n^{II} e^{-jk_n^{II}(x-a)} - B_n^{II} e^{+jk_n^{II}(x-a)}\right), \quad (11)$$

$$A^{III} = \sum_{m=1}^{M} C_m^I \sin\left(\frac{m\pi}{a}x\right)\sin(k_m^I(z-a)) + \sum_{n=1}^{N} C_m^{II} \sin\left(\frac{n\pi}{a}z\right)\sin(k_n^{II}x). \quad (12)$$

Matching the transverse field components at the discontinuities:

$$F^I + B^I = D^I(F^I - B^I) + L^I(F^{II} - B^{II}), \quad (13)$$

$$F^{II} + B^{II} = L^{II}(F^I - B^I) + D^{II}(F^{II} - B^{II}). \quad (14)$$

And then,

$$[S] = inv\begin{bmatrix} I + D^I & -L^I \\ L^{II} & I - D^{II} \end{bmatrix} * \begin{bmatrix} D^I - I & -L^{II} \\ L^{II} & -D^{II} - I \end{bmatrix}. \quad (15)$$

Two distinct waveguide bends can be identified, left bend and right bend. Therefore, when the structure contains these two waveguide bends, the bend sense must be taken into consideration. The following examples illustrate the two possibilities; the first, shown in Fig. 7, is a succession of two bends from different kind, and the second, in Fig. 9, is a succession of two bends from the same kind. Each structure is followed by the comparison of the computed S-parameters and HFSS simulator results. They are shown in Fig. 8 and Fig. 10 respectively, and a good agreement is observed from the curves. In these examples, we used WR75 standard waveguide.

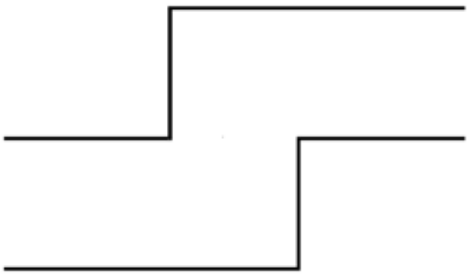

Fig. 7. Succession of two bends from different kind.

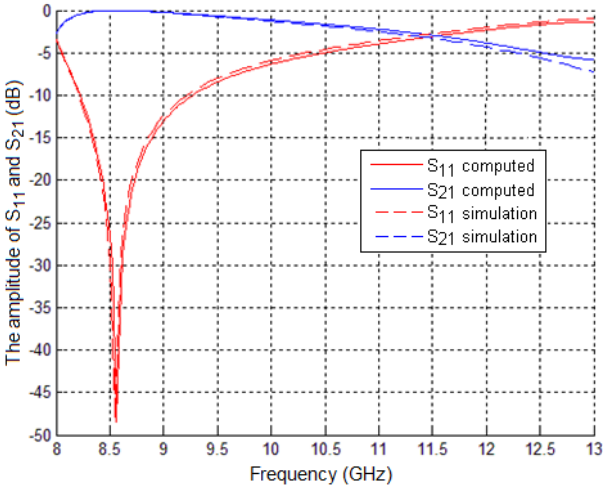

Fig. 8. Computed (——) and HFSS simulated (----) frequency responses of the two bends from different kind.

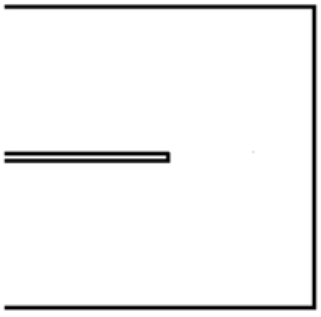

Fig. 9. Succession of two bends from the same kind.

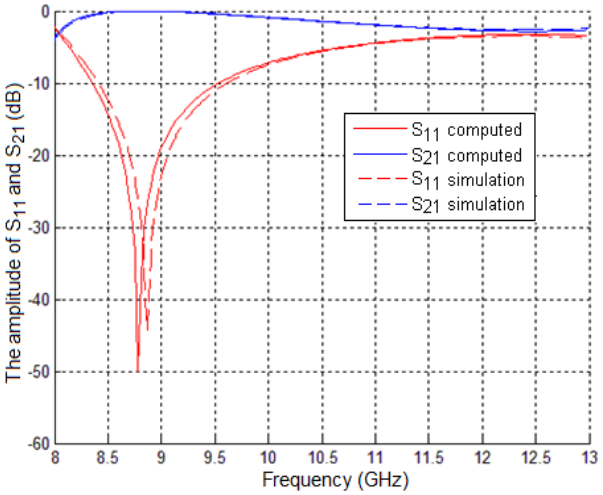

Fig. 10. Computed (——) and HFSS simulated (----) frequency responses of the two bends from same kind.

B. T-junction

To analyze the T-junction, we used the same technique as waveguide bend with adding a third port, then the resonator region becomes formed by three conducting walls (broken line in Fig. 11).

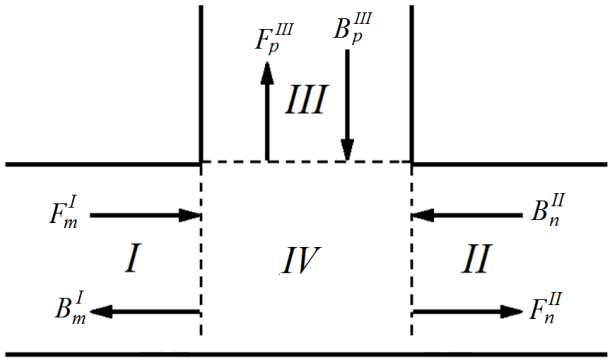

Fig. 11. T-junction.

Vector potentials at the four regions:

$$A^{I}=\sum_{m=1}^{M}T_m^{I}\sin\left(\frac{m\pi}{a}x\right)\left(F_m^{I}e^{-jk_m^{I}z}-B_m^{I}e^{+jk_m^{I}z}\right), \quad (16)$$

$$A^{II}=\sum_{n=1}^{N}T_n^{II}\sin\left(\frac{n\pi}{a}x\right)\cdot \left(F_n^{II}e^{-jk_n^{II}(z-a)}-B_n^{II}e^{+jk_n^{II}(z-a)}\right), \quad (17)$$

$$A^{III}=\sum_{p=1}^{P}T_p^{III}\sin\left(\frac{p\pi}{a}z\right)\cdot \left(F_p^{III}e^{-jk_p^{III}(x-a)}-B_p^{III}e^{+jk_p^{III}(x-a)}\right), \quad (18)$$

$$A^{IV}=\sum_{m=1}^{M}C_m^{I}\sin\left(\frac{m\pi}{a}x\right)\sin(k_m^{I}(z-a))+ \sum_{n=1}^{N}C_n^{II}\sin\left(\frac{n\pi}{a}x\right)\sin(k_n^{II}z)+ \sum_{p=1}^{P}C_p^{III}\sin\left(\frac{p\pi}{a}z\right)\sin(k_p^{III}x). \quad (19)$$

Matching the transverse field components at the discontinuities:

$$F^{I}+B^{I}=D^{I}(F^{I}-B^{I})+L^{I,II}(F^{II}-B^{II})+ L^{I,II}(F^{II}-B^{II})+L^{I,III}(F^{III}-B^{III}), \quad (20)$$

$$F^{II}+B^{II}=L^{II,I}(F^{I}-B^{I})+ D^{II}(F^{II}-B^{II})+L^{II,III}(F^{III}-B^{III}), \quad (21)$$

$$F^{III}+B^{III}=L^{III,I}(F^{I}-B^{I})+ L^{III,II}(F^{II}-B^{II})+D^{III}(F^{III}-B^{III}). \quad (22)$$

As for the junction and the bend, we could write the S matrix for the T-junction under the vector product to simplify calculations; the latter will be of great help for the simulation of a complex structure:

$$[S]=inv\begin{bmatrix} I+D^{I} & -L^{I,II} & -L^{I,III} \\ L^{II,I} & I-D^{II} & -L^{II,III} \\ -L^{III,I} & -L^{III,II} & I-D^{III} \end{bmatrix}*\begin{bmatrix} D^{I}-I & -L^{I,II} & -L^{I,III} \\ L^{II,I} & -D^{II}-I & -L^{II,III} \\ -L^{III,I} & -L^{III,II} & -I-D^{III} \end{bmatrix}. \quad (23)$$

For a WR75 waveguide T-junctions, we can note in Fig. 12 a perfect superposition between mode matching analysis and results in [18].

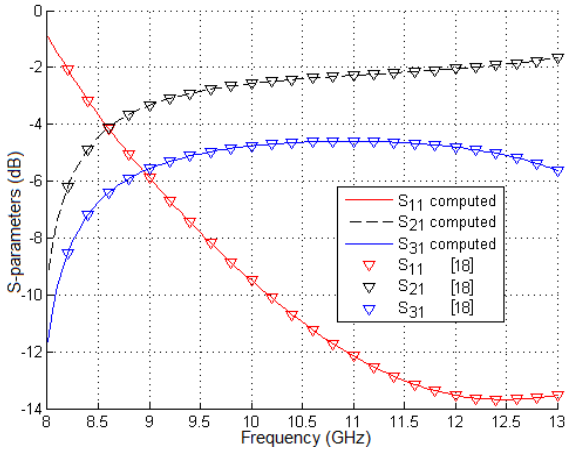

Fig. 12. Frequency response of a WR75 wiveguide T-junction.

V. PRACTICAL SWARM OPTIMIZATION PSO

Presented in 1995 by Kennedy, Particle Swarm Optimization (PSO) is a quite recent optimization technique [13]. Like genetic algorithms, it is inspirited from nature, so it consists of finding the optimal solution by simulating such social behavior of groups as a bird or bee flocking. It is a simple concept implemented in a few lines of computer code.

Compared to GA, the two methods are favorable to perform with high success rate the tasks of synthesizing microwave structures, with a slight advantage for the GA, but a big advantage for PSO in speed of executing time.

In what follows, we will give the notation and the algorithm of the method.

A. PSO notation

For each particle *i*:

- x_i is a vector denoting its position and y_i denotes its objective function value.
- y_i is the vector denoting its velocity.
- p_i is the best position that it has found so far and $Pbest_i$ denotes its objective function score.
- g_i is the best position that has been found so far in its neighborhood and $Gbest_i$ denotes the objective function value of g_i.

Velocity update:

- $\vec{U}(0,\varphi_i)$ is a random vector uniformly distributed in $[0,\varphi_i]$ generated at each generation for each particle.
- φ_1 and φ_2 are the acceleration coefficients determining the scale of the forces in the direction of p_i and g_i.
- $\otimes$ denotes the element-wise multiplication operator.

B. PSO algorithm

- Randomly initialize particle positions and velocities.
- While not terminate.
- For each particle i:
  1. Evaluate fitness y_i at current position x_i.
  2. If y_i is better than $Pbest_i$ then update $Pbest_i$ and p_i.
  3. If y_i is better than $Gbest_i$ then update $Gbest_i$ and g_i.
  4. Update velocity y_i and position x_i using:

$$\vec{v}_{i+1} \leftarrow \vec{v}_i + \vec{U}(0,\varphi_1) \otimes (\vec{p}_i - \vec{x}_i) + \vec{U}(0,\varphi_2) \otimes (\vec{g}_i - \vec{x}_i), \quad (24)$$

$$\vec{x}_{i+1} \leftarrow \vec{x}_i + \vec{v}_i, \quad (25)$$

C. Fitness function

The fitness function is an important part of any optimization method; it should evaluate how good the solution is, then the optimal solution is the one which minimizes the fitness function [19]. In this work, we used Discrete Target Approximation [20], which is a simple evaluation of the specifications fulfillment. It consists of assigning to each one of the N frequency points a value of 0 if the response function does not satisfy the corresponding specification, and on the contrary, a value of 1 if it satisfies the specification. The final fitness is the sum of the $\{0,1\}$ values for all the response points, divided by the number of points.

VI. EXAMPLE OF FILTER SYNTHESIS

We applied our combination for the synthesis of a fourth-order waveguide filter. Figure 13 shows the rectangular waveguide filter configuration used in order to implement the matrix (1) into waveguide filter. As mentioned before, the inverters are realized by inserting capacitive or inductive irises depending on the sign of the coupling coefficient in the coupling matrix (inductive iris for the positive coefficient and capacitive iris for negative coefficient) and the resonators are implemented by half-wave resonant cavities, chosen to make the fundamental mode resonate. We aimed to use a side by side waveguide configuration and purely inductive or capacitive irises to facilitate the further manufacturing of filter, using a CNC milling machine. The filter has a central frequency of 10 GHz, a bandwidth of 300 MHz and 20 dB of return loss level. The housing waveguide is a WR75.

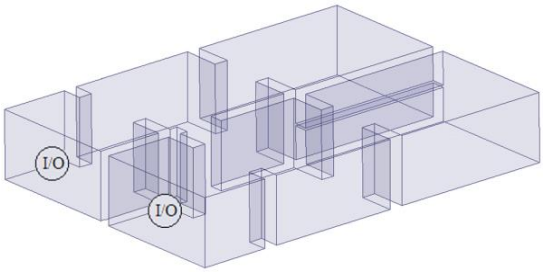

Fig. 13. Geometry of the proposed four-cavity filter.

To analyze the proposed structure, we used the segmentation method [21], which consists of fragmenting the structure into basic elements (seen in the first part of the paper), representing this same structure under network form and then using multi-port networks analysis [22], to analyze the obtained network (Fig. 14), where all the matrices of each segment are put together in a single matrix S_p in Equation (27) [23].

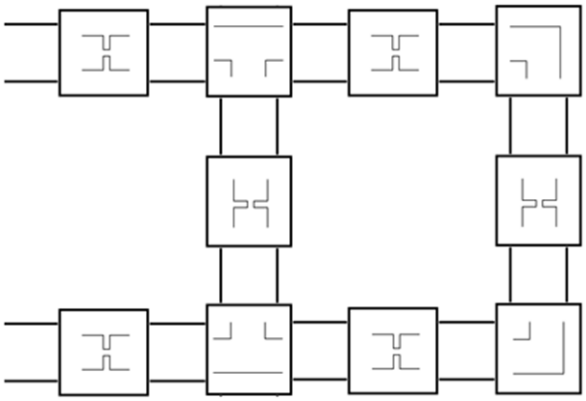

Fig. 14. Structure segmentation for network analysis.

If $\bar{a}_p$, $\bar{b}_p$ and $\bar{a}_c$, $\bar{b}_c$ are incident and reflected wave variables at the *p* external and *c* internal connected ports. The S_p matrix relating the external port is:

$$\begin{bmatrix} \bar{b}_p \\ \bar{b}_c \end{bmatrix} = \begin{bmatrix} S_{pp} & S_{pc} \\ S_{cp} & S_{cc} \end{bmatrix} \begin{bmatrix} \bar{a}_p \\ \bar{a}_c \end{bmatrix}, \tag{26}$$

$$S_p = S_{pp} + S_{pc}(\Gamma - S_{cc})^{-1} S_{cp}, \tag{27}$$

Γ is the connection matrix that relates adjacent internal ports.

As for the analysis of basic structures and to be assured of the analysis accuracy, we found it necessary to analyze a multi-cell structure treated before and having some similarities with that proposed in this work. We chose the proposed structure in [24] (Fig. 15) where, in both structures, rectangular waveguides are used and the both can be segmented into the same basic elements (junctions, bends and T-junction). The difference is that in the reference filter, the input and output waveguides are superposed, and resonant irises are used. A good agreement is observed in Fig. 16, by comparing the results of multi-port networks analysis and measurement from reference [24].

After the optimization, the finale filter dimensions are illustrated with dimensioning letters in Fig. 17, where the housing waveguide is a standard WR75 (19.0500 mm x 9.5250 mm). The first iris opening (between I/O and cavity ①) is (*a2*=11.5833 mm) with a shift to the left by (*x1*=3.2430 mm). The second iris opening (between cavity ① and cavity ②) is (*a3*=8.3379 mm). The capacitive iris opening (between cavity ② and cavity ③) is (b2=0.3000 mm). The forth iris opening (between cavity ① and cavity ④) is (a4=5.9782 mm) with a shift to the ports side by (x4=0.9809 mm). The length of the first cavity is (T=19.0990 mm) and the length of the second is (L=23.5963 mm). The thickness of all irises is 2 mm.

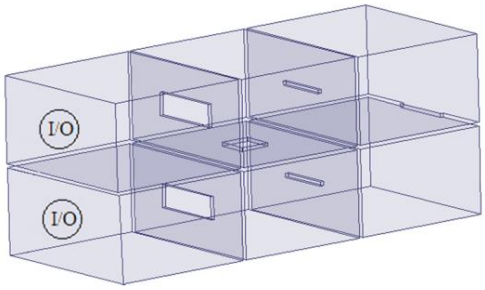

Fig. 15. Configuration of the reference filter [24].

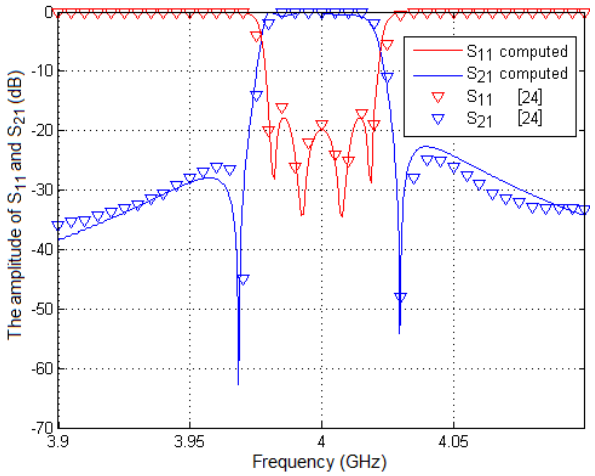

Fig. 16. S-parameters response of the reference filter shown in Fig. 15.

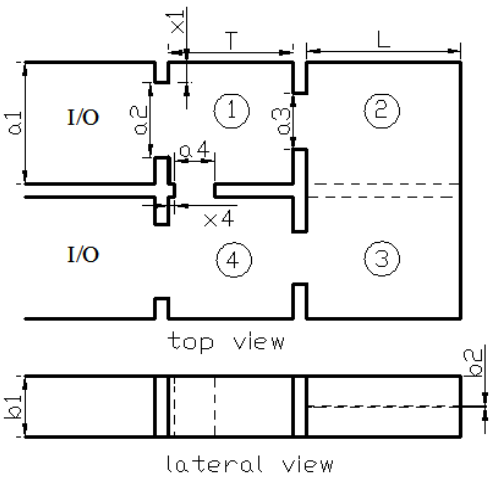

Fig. 17. Filter illustration with dimensioning letters.

Figure 18 shows the comparison between optimized waveguide filter response and equivalent circuit response. We can observe a good fulfillment of the filter specifications, aside from a slight shift of the

right transmission zero.

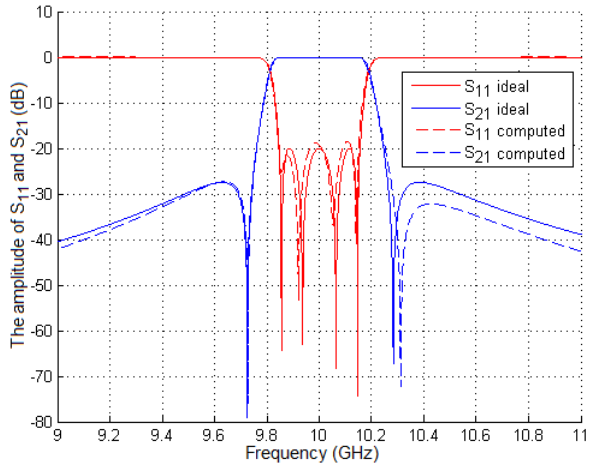

Fig. 18. Ideal circuit response of prototype filter and fullwave computed response.

VII. CONCLUSION

The hardest in the design of microwave filter is to convert a coupling matrix or an equivalent circuit into a microwave structure, this regardless of the manufacturing technique (waveguide, microstrip ... etc.).

This work presents a method for waveguide filter synthesis from predetermined specification. For this, we used a procedure that consists of a series of techniques and methods of calculation, simulation and optimization. All these steps are programmed under Matlab and successfully applied to synthesis waveguide filters.

The direct design by optimization of higher order waveguide filter, without calculating the initial dimensions often tends to fail. This is due to the high number of variables (dimensions of the microwave structure) and also to the high sensitivity of the filter response at very small variation in its dimensions. To alleviate this problem, it is necessary either to divide the structure into several sub-structures, and optimize each one separately, or by calculates the initial dimensions using appropriate approach methods.

REFERENCES

[1] R. Levy and S. B Cohn, "A history of microwave filter research, design, and development," *IEEE Transactions on Microwave Theory and Techniques*, MTT-32, no. 9, September 1984.

[2] A. E. Atia, A. E. Williams, and R. W. Newcomb, "Narrow-band multiple-coupled cavity synthesis," *IEEE Transaction on Circuit and Systems*, vol. CAS-21, no. 5, September 1974.

[3] G. L. Matthaei, L. Young, and E. M. T Jones, *Microwave Filters, Impedance-Matching Networks, and Coupling Structures*. Artech House 1980.

[4] J. D Rhodes, "The generalized direct-coupled cavity linear phase filter," *IEEE*, MTT-18, no. 6, June 1970.

[5] A. E Atia and Williams, "Narrow-bandpass waveguide filters," *IEEE Transactions on Microwave Theory and Techniques*, MTT-20, no. 4, pp. 258-265, 1972.

[6] R. J. Cameron, C. M. Kudsia, and R. R. Mansour, *Microwave Filters for Communication Systems*. John Wiley & Sons, Inc., 2007.

[7] M. Guglielmi, P. Jarry, E. Kerherve, O. Roquebrun, and D. Schmitt, "A new family of all-inductive dual-mode filters," *IEEE Transactions on Microwave Theory and Techniques*, MTT-49, no. 10, pp 1764-1769, 2001.

[8] M. Bekheit, S. Amari, and F. Seyfert, "A new approach to canonical dual-mode cavity filter design," *IEEE Transactions on Microwave Theory and Techniques*, vol. 57, no. 5, pp 1196-1206, May 2009.

[9] M. Guglielmi and C. Newport, "Multimode equivalent network representation of inductive discontinuities," *IEEE Transactions on Microwave Theory and Techniques*, MTT-38, no. 11, pp. 1651-1659, November 1990.

[10] R. F. Harrington, *Field Computation by Moment Methods*. Wiley-IEEE Press, April 1993.

[11] R. C Booton, Jr., *Computational Methods for Electromagnetics and Microwaves*. John Wiley & Sons, Inc., Publication 1992.

[12] H. Patzelt and F. Arndt, "Double-plane steps in rectangular waveguides and their application for transformers, irises, and filters," *IEEE Transactions on Microwave Theory and Techniques*, MTT-30, no. 5, pp. 771-776, May 1982.

[13] J. Kennedy and R. Eberhart, "Particle swarm optimization," *IEEE*, pp. 1942-1948, 1995.

[14] N. Marcuvitz, *Waveguide Handbook*. Polytechnic Institute of New Work, December 1986.

[15] J. Bornemann and R. Vahldieck, "Characterization of a class of waveguide discontinuities using a modified TE^{x}_{mn} mode approach," *IEEE Transactions on Microwave Theory and Techniques*, vol. 38, no. 12, pp. 1816-1822, December 1990.

[16] T. S. Chen, "Characteristics of waveguide resonant iris filters," *IEEE Transactions on Microwave Theory and Techniques*, vol. 15, no. 4, pp. 260-262, April 1967.

[17] T. Sieverding and F. Amdt, "Field theoretic CAD of open or aperture matched T-junction coupled rectangular waveguide structures," *IEEE Transactions on Microwave Theory and Techniques*, vol. 40, no. 2, pp. 353-362, February 1992.

[18] R. H. MacPhie and K.-L. Wu, "A full-wave

modal analysis of arbitrarily shaped waveguide discontinuities using the finite plane-wave series expansion," *IEEE Transactions on Microwave Theory and Techniques*, vol. 47, no. 2, pp. 232-237, February 1999.

[19] J. W. Bandler, "Optimization methods for computation-aided design," *IEEE Transactions on Microwave Theory and Techniques*, vol. 17, no. 8, pp. 533-552, August 1969.

[20] M. F. J. Nogales, J. P. Garcia, J. Hinojosa, and A. A. Melcon, "Genetic algorithms applied to microwave filters optimization and design," *Progress in Electromagnetics Research Symposium*, Cambridge, USA, pp. 99-103, July 2008.

[21] T. Okoshi, Y. Uehara, and T. Takeuchi, "The segmentation method—An approach to the analysis of microwave planar circuits," *IEEE Transactions on Microwave Theory and Techniques*, October 1976.

[22] V. A. Monaco and P. Tiberio, "Computer-aided analysis of microwave circuits," *IEEE Transactions on Microwave Theory and Techniques*, vol. 22, no. 3, pp. 249-263, March 1974.

[23] R. Chad, and K. C. Gupta, "Segmentation method using impedance matrices for analysis of planar microwave circuits," *IEEE Transactions on Microwave Theory and Techniques*, vol. 29, no. 1, pp. 71-74, January 1981.

[24] T. Shen, H. T Hsu, K. A. Zaki, A. E. Atia, and T. G. Dolan, "Full-wave design of canonical waveguide filters by optimization," *IEEE Transactions on Microwave Theory and Techniques*, vol. 51, no. 2, pp. 533-552, February 2003.